1-1-2014

Light-Enabled Identification of the Neuronal Substrates of Alkylphenol Anesthetics

Brian Weiser
University of Pennsylvania, weiser.brian@gmail.com

Light-Enabled Identification of the Neuronal Substrates of Alkylphenol Anesthetics

Abstract
General anesthetics are a critical class of drugs in modern medicine; however, the precise mechanisms by which they cause unconsciousness and unwanted side effects are largely undefined. In order to understand pharmacologic mechanisms of anesthetic action, drug interactions with macromolecular substrates and the subsequent functional consequences must be characterized. Analogs of general anesthetics that function as photolabels have been developed to assist in the identification of molecular targets. One such photolabel, meta-azi-propofol (AziPm), is an analog of the clinically used alkylphenol anesthetic propofol. In this work, AziPm is employed in a variety of experiments that aim to identify molecular substrates of propofol. Two proteins identified as propofol targets are more thoroughly examined: (1) the sirtuin deacetylase SIRT2 and (2) the mitochondrial voltage-dependent anion channel (VDAC). The binding sites of propofol on these proteins, and the in vitro functional consequences of propofol binding, are determined. Also described are the molecular interactions of VDAC with a separate ligand, cholesterol, which shares a binding site with propofol. In addition to molecular studies, a novel in vivo photolabeling technique, called optoanesthesia, that utilizes AziPm is introduced, and the behavioral phenotype induced by optoanesthesia in Xenopus laevis tadpoles is characterized. Finally, optoanesthesia is demonstrated with other ligands, including a photoactive analog of an anthracene anesthetic, and mechanistic insight into the pharmacology of this anthracene is revealed.

Degree Type
Dissertation

Degree Name
Doctor of Philosophy (PhD)

Graduate Group
Pharmacology

First Advisor
Roderic G. Eckenhoff

Subject Categories
Pharmacology

LIGHT-ENABLED IDENTIFICATION OF THE NEURONAL SUBSTRATES OF ALKYLPHENOL ANESTHETICS

Brian Patrick Weiser

A DISSERTATION

in

Pharmacology

Presented to the Faculties of the University of Pennsylvania

in

Partial Fulfillment of the Requirements for the

Degree of Doctor of Philosophy

2014

Supervisor of Dissertation:

_____

Roderic G. Eckenhoff, MD, Austin Lamont Professor of Anesthesiology & Critical Care

Graduate Group Chairperson:

_____

Julie A. Blendy, PhD, Professor of Pharmacology

Dissertation Committee:

(chair) Harry Ischiropoulos, PhD, Research Professor of Pediatrics

Max B. Kelz, MD PhD, Associate Professor of Anesthesiology & Critical Care

Ivan J. Dmochowski, PhD, Associate Professor of Chemistry

A. Joshua Wand, PhD, Benjamin Rush Professor of Biochemistry

LIGHT-ENABLED IDENTIFICATION OF THE NEURONAL SUBSTRATES OF ALKYLPHENOL ANESTHETICS

ACKNOWLEDGEMENTS

Throughout my graduate studies, I have been surrounded by excellent scientists who have been extremely supportive of my work. First and foremost, I will forever be grateful to Rod and Maryellen Eckenhoff for all of their support and guidance throughout the past 4.5 years; I am certain that I could not have chosen a better lab for my PhD work. Thank you to all of my collaborators at UPenn, including Max Kelz, Ivan Dmochowski, Weiming Bu, Bill Dailey, Nathan Weinbren, and Kellie Woll; I have had very positive and productive interactions with all of these people. I am extremely grateful to my collaborators at Rutgers University-Camden, Grace Brannigan and Reza Salari, and also to Tatiana Rostovtseva and members of her lab at the National Institute of Child Health and Human Development. Finally, I would like to thank Alan Cahill and Jay Mills, who introduced me to academic science at Thomas Jefferson University and were critical in my decision to go to graduate school.

This body of work could not have been accomplished without all of the above individuals. One final person who was instrumental in my graduate school career is my wife, Hilary McCarren. Thank you for endless scientific discussion, but more importantly, thank you for everything else you do that is unrelated to science.

ABSTRACT

LIGHT-ENABLED IDENTIFICATION OF THE NEURONAL SUBSTRATES OF ALKYLPHENOL ANESTHETICS

Brian P. Weiser

Roderic G. Eckenhoff

General anesthetics are a critical class of drugs in modern medicine; however, the precise mechanisms by which they cause unconsciousness and unwanted side effects are largely undefined. In order to understand pharmacologic mechanisms of anesthetic action, drug interactions with macromolecular substrates and the subsequent functional consequences must be characterized. Analogs of general anesthetics that function as photolabels have been developed to assist in the identification of molecular targets. One such photolabel, *meta*-azi-propofol (AziP*m*), is an analog of the clinically used alkylphenol anesthetic propofol. In this work, AziP*m* is employed in a variety of experiments that aim to identify molecular substrates of propofol. Two proteins identified as propofol targets are more thoroughly examined: (1) the sirtuin deacetylase SIRT2 and (2) the mitochondrial voltage-dependent anion channel (VDAC). The binding sites of propofol on these proteins, and the *in vitro* functional consequences of propofol binding, are determined. Also described are the molecular interactions of VDAC with a separate ligand, cholesterol, which shares a binding site with propofol. In addition to molecular studies, a novel *in vivo* photolabeling technique, called optoanesthesia, that utilizes AziP*m* is introduced, and the behavioral phenotype induced by optoanesthesia in *Xenopus laevis*

tadpoles is characterized. Finally, optoanesthesia is demonstrated with other ligands, including a photoactive analog of an anthracene anesthetic, and mechanistic insight into the pharmacology of this anthracene is revealed.

TABLE OF CONTENTS

ACKNOWLEDGEMENTS.....iii

ABSTRACT.....iv

LIST OF TABLES.....ix

LIST OF FIGURES.....x

ABBREVIATIONS AND ACRONYMS.....xii

CHAPTER 1: INTRODUCTION TO GENERAL ANESTHETICS AND ANESTHETIC PHOTOLABELING.....1

1.1 Relevance of General Anesthetic Pharmacology.....1

1.2 General Anesthetic Photolabeling.....3

1.3 Development and Detection of Anesthetic Photolabels.....3

1.4 Experimental Approach for the Discovery of Anesthetic Targets.....6

CHAPTER 2: PROPOFOL AND ALKYLPHENOL ANESTHETICS.....8

2.1 Alkylphenol Anesthetic Pharmacology.....8

2.2 *Meta*-Azi-Propofol (AziP*m*).....9

2.3 AziP*m* Binding to Whole Brain.....10

2.4 AziP*m* Binding to Synaptosomal Protein.....14

2.5 AziP*m* Binding to Neuronal Lipids.....17

CHAPTER 3: PROPOFOL INTERACTIONS WITH SIRT2 DEACETYLASE....19

3.1 Experimental Rationale and Introduction to SIRT2.....19

3.2 Identification of SIRT2 as a Propofol Target.....20

3.3 Conformation-Specific Propofol-SIRT2 Binding.....22

3.4 Inhibition of SIRT2 by Propofol.....25

3.5 A Unique Sirtuin Inhibitory Site....28

3.6 Relevance of SIRT2 Inhibition by Propofol....30

CHAPTER 4: ALKYLPHENOL ANESTHETIC BINDING AND MODULATION OF MITOCHONDRIAL VDAC....32

4.1 Introduction to the Tadpole as a Model Organism....32

4.2 AziP*m* Binding to Tadpole VDAC *In Vivo*....33

4.3 Introduction to VDAC....37

4.4 General Anesthetic-VDAC Binding....38

4.5 Sites and Functional Consequence of VDAC-Alkylphenol Anesthetic Interactions....39

CHAPTER 5: INVESTIGATION OF VDAC-CHOLESTEROL BINDING WITH MOLECULAR DYNAMICS SIMULATIONS....50

5.1 Experimental Rationale and Introduction to VDAC-Cholesterol Binding....50

5.2 Cholesterol-Bound VDAC Model....51

5.3 Effects of Cholesterol on VDAC Dynamics....57

5.4 Effects of Cholesterol on Open VDAC Ion Permeability....61

5.5 Conclusions, Cholesterol Binding to VDAC....64

CHAPTER 6: OPTOANESTHESIA....67

6.1 Optoanesthesia in *X. laevis* Tadpoles....67

6.2 *In Vivo* Covalent Attachment of [^{3}H]AziP*m* to Proteins Over Time....69

6.3 Expanding the Optoanesthesia Technique....73

CHAPTER 7: TUBULIN AS A TARGET OF ANTHRACENE GENERAL ANESTHETICS....76

7.1 1-Aminoanthracene (1-AMA) and 1-Azidoanthracene (1-AZA).....76

7.2 *In vivo* Tadpole Photolabeling with 1-AZA.....77

7.3 Tubulin as a Target of 1-AZA.....79

7.4 Shifting Sensitivity of Tadpoles to 1-AMA.....84

7.5 Implications of Tubulin as a Target of 1-AMA.....85

CHAPTER 8: CONCLUSIONS.....88

APPENDIX.....91

A1. Experimental Procedures.....91

A1.1 Materials and Instrumentation.....91

A1.2 Methods.....92

A1.3 Figures and Statistics.....120

A2. Mass Spectra.....121

A2.1 SIRT2 Peptides Photolabeled by AziP*m*.....121

A2.2 VDAC Peptides Photolabeled by AziP*m*.....127

A2.3 Tubulin Peptides Photolabeled by 1-AZA.....138

A3. Acknowledgement of Funding Sources.....141

BIBLIOGRAPHY.....142

LIST OF TABLES

Table 1. Physicochemical properties of propofol and AziP*m*.....10

Table 2. [^{3}H]AziP*m* binding to rat brain regions.....12

Table 3. [^{3}H]AziP*m* binding to rat brain by primary composition of regions.....13

Table 4. [^{3}H]AziP*m* binding to major rat brain lipids.....17

Table 5. SIRT2 peptides photolabeled by AziP*m*.....21

Table 6. Analysis of [^{3}H]AziP*m*-photolabed protein from tadpole brain.....36

Table 7. Relative protein abundance in rat VDAC spots from IEF/SDS-PAGE.....40

Table 8. Conductance (nS) per VDAC channel with propofol under low voltage.....45

Table 9. Calculated VDAC gating parameters at negative voltages with propofol.....47

Table 10. Residues that cholesterol contacts in VDAC sites.....56

Table 11. Percent of simulation frames in which VDAC residue pairs hydrogen bond.....61

Table 12. Analysis of 1-AZA-photolabeled protein from tadpole brain.....80

Table 13. Tubulin polymerization rates with and without anthracenes and colchicine....84

LIST OF FIGURES

Figure 1. Chemical structures of general anesthetics and their photoactive analogs.....5

Figure 2. Chemical structures of propofol and AziP*m*.....10

Figure 3. Autoradiographs of [^{3}H]AziP*m*-photolabeled brain sections.....11

Figure 4. Autoradiograph of [^{3}H]AziP*m*-photolabeled synaptosomal protein.....15

Figure 5. Autoradiograph of [^{3}H]AziP*m*-photolabeled protein from brain fractions.....16

Figure 6. Autoradiograph of [^{3}H]AziP*m*-photolabeled myelin protein.....21

Figure 7. Inhibition of [^{3}H]AziP*m* photolabeling of myelin SIRT2 by propofol.....22

Figure 8. Structural analysis of the propofol cavity on SIRT2.....24

Figure 9. Inhibition of [^{3}H]AziP*m* photolabeling of active SIRT2 by propofol.....25

Figure 10. SIRT2 deacetylase assays with inhibition by propofol.....26

Figure 11. SIRT2 deacetylase assays in the presence of epothilone D.....28

Figure 12. Structural comparison of inhibitor binding sites on SIRT2.....29

Figure 13. Radioactivity content in tadpole brain protein after *in vivo* photolabeling and SDS-PAGE.....33

Figure 14. Radioactivity content in tadpole brain protein after *in vivo* photolabeling and IEF/SDS-PAGE.....34

Figure 15. IEF/SDS-PAGE gel of rat brain mitochondria.....40

Figure 16. LC-MS/MS sequence coverage of rat VDAC protein.....42

Figure 17. Location of AziP*m*-photolabeled VDAC residues.....44

Figure 18. Propofol effects on open VDAC conductance.....45

Figure 19. Propofol effects on VDAC gating.....46

Figure 20. Propofol effects on gramicidin A.....49

Figure 21. Alkylphenol and cholesterol binding site on VDAC.....50

Figure 22. Location of cholesterol binding sites on VDAC.....52

Figure 23. Orientations of cholesterol molecules docked onto VDAC.....53

Figure 24. Cholesterol-bound VDAC model.....54

Figure 25. RMSD of VDAC backbones from simulations ± bound cholesterol.....58

Figure 26. VDAC residue α-carbon RMSF from simulations ± bound cholesterol.....59

Figure 27. Positive electrostatic potential maps from VDAC simulations ± bound cholesterol.....62

Figure 28. Ion density maps from VDAC simulations ± bound cholesterol.....63

Figure 29. VDAC potential of mean force from simulations ± bound cholesterol.....65

Figure 30. Tadpole optoanesthesia with AziP*m*.....68

Figure 31. Radioactivity content in tadpole brain protein over time.....70

Figure 32. Tadpole optoanesthesia with alkylphenol anesthetic photolabels.....73

Figure 33. Targeted photolabeling of [^{3}H]AziP*m* in mouse brain.....75

Figure 34. Synthesis of 1-AZA from 1-AMA.....77

Figure 35. Confocal microscopy of 1-AZA-photolabeled tadpoles.....78

Figure 36. Tadpole optoanesthesia with 1-AZA.....79

Figure 37. IEF/SDS-PAGE gel of 1-AZA photolabeled tadpole brain protein.....80

Figure 38. Tubulin peptides photolabeled by 1-AZA.....81

Figure 39. Structural visualization of the 1-AZA/colchicine tubulin site.....82

Figure 40. Anthracene and colchicine competition for tubulin binding.....83

Figure 41. Epo-D stabilization of microtubules *in vivo* in tadpoles.....84

Figure 42. Tadpole 1-AMA dose-response curves ± EpoD.....86

ABBREVIATIONS AND ACRONYMS

1-AMA – 1-aminoanthracene

1-AZA – 1-azidoanthracene

ADP – adenosine 5'-diphosphate

AziP*m* – *meta*-azi-propofol

CNS – central nervous system

DOPC – 1,2-dioleoyl-*sn*-glycero-3-phosphocholine

DOPE – 1,2-dioleoyl-*sn*-glycero-3-phosphoethanolamine

HDAC – histone deacetylase

IEF – isoelectric focusing

LC-MS/MS – liquid chromatography with online tandem mass spectrometry

NAD^+ – nicotinamide adenine dinucleotide

PC – phosphatidylcholine

PE – phosphatidylethanolamine

PI – phosphatidylinositol

PS – phosphatidylserine

RMSD – root mean square deviation

RMSF – root mean square fluctuation

SDS-PAGE – sodium dodecyl sulfate polyacrylamide gel electrophoresis

SNAP25 – synaptosomal-associated protein 25

SPH – sphingomyelin

UVA – long-wave ultraviolet light

VDAC – voltage-dependent anion channel

CHAPTER 1: INTRODUCTION TO GENERAL ANESTHETICS AND ANESTHETIC PHOTOLABELING

1.1 Relevance of General Anesthetic Pharmacology

General anesthetics are united by their ability to cause the clinically important endpoints of reversible unconsciousness and amnesia. These drugs enable over 230 million surgeries to be performed worldwide every year (Weiser *et al.*, 2008). Despite this widespread use in medicine, the mechanisms by which general anesthetics act remain undefined on both the molecular and systems neuroscience levels.

As a class of drugs, general anesthetics are chemically diverse and include both injectable and volatile compounds. Small organic molecules, halogenated alkanes and ethers, and even the gaseous element xenon can be efficacious anesthetics. The Meyer-Overton hypothesis (Meyer, 1901; Overton, 1901) that general anesthesia is caused by non-specific perturbation of cellular membranes has largely been supplanted by research focusing on interactions of anesthetics with proteins. Considerable attention has been devoted to hypotheses suggesting that different classes of anesthetics elicit their effects through proteins localized within distinct neuronal circuits; however, the efficacies of different anesthetic chemotypes likely arise from modulating different molecular and neuronal targets. Most current theories of anesthetic action emphasize additive or synergistic interactions with multiple targets, each contributing variably to a given anesthetic endpoint. Thus, bulk partitioning or strong binding to a target does not imply relevance, as a high concentration of ligand may be required for a small contribution to an endpoint and vice versa, on both the molecular and physiologic levels.

The potencies of general anesthetics vary over at least five orders of magnitude, yet the drugs exhibit similarly steep Hill slopes in population studies; for example, the dose response curves for human unconsciousness have Hill slopes of ~15 and ~6 for sevoflurane and propofol, respectively (Katoh and Ikeda, 1987; Smith *et al.*, 1994). Population Hill slopes statistically quantify pharmacodynamic variability. A plausible explanation for the homogeneity of general anesthetic response in populations is that the compounds act on a highly conserved target with a highly conserved function. In general, however, drugs that act on a single molecular target *in vivo* typically produce broader population dose response curves with a Hill slope of ~1 due to genetic or physiologic variability (Eckenhoff and Johansson, 1997). Coupled with the fact that complete resistance to any general anesthetic has not been imposed on an organism through genetic or pharmacologic manipulations, it seems likely that multiple molecular targets each contribute partially to the cellular and systematic pathways that regulate the state of consciousness and are disrupted by anesthetics.

In addition to causing unconsciousness with a change of concentration less than a factor of 1.6 (Franks, 2008), general anesthetics have narrow therapeutic indices (LD_{50}/ED_{50}) (for example, 6-12 for propofol and 2-4 for sevoflurane (James and Glen, 1980; Baxter International Inc., 2013). Thus, the medical specialty of anesthesiology is needed to ensure the safe administration of these drugs. Further, along with the intended "on-pathway" endpoint- that is, the state of general anesthesia- the promiscuous nature of these small compounds leads to a plethora of undesired "off-pathway" effects. These include both acute (Patel *et al.*, 2003; Wickley *et al.*, 2009; Whittington *et al.*, 2011) and

chronic effects, with the latter including neurodevelopmental and neurodegenerative risks (Zhang *et al.*, 2009; Papon *et al.*, 2011).

1.2 General Anesthetic Photolabeling

To ensure optimal administration of current anesthetics and to rationally develop new drugs for clinical use, a comprehensive understanding of their modes of action is required. At clinical concentrations, general anesthetics affect the function of certain proteins. Injectable general anesthetics are typically of higher potency than the volatile type, suggesting higher affinities for protein targets that influence consciousness; however, micromolar dissociation constants are common for all anesthetic-macromolecule interactions. Micromolar dissociation constants indicate rapid ligand unbinding, and one experimental approach that overcomes these dissociation kinetics is photolabeling.

Photolabeling specifies that a ligand undergoes photolysis upon light exposure, generating chemically unstable intermediates that covalently attach to macromolecules. This adduct provides a tag in a site that can be identified with mass spectrometry, or else traced if the ligand is radiolabeled. General anesthetic photolabeling experiments have previously been performed with purified proteins, enriched subcellular fractions, and tissue sections, with variations on each biological system, and anesthetic photolabeling has been used to identify protein binding sites, to study functional effects of ligand binding, and for discovery-based proteomic or distribution studies.

1.3 Development and Detection of Anesthetic Photolabels

With ~254 nm exposure, halothane undergoes photodecomposition, primarily to reactive chlorotrifluoroethyl and bromine radicals, which permits its use as a photolabel (Bösterling *et al.*, 1982; el-Maghrabi *et al.*, 1992). An advantage of halothane photolabeling is the use of an unmodified clinical compound; however, the high energy UV that induces photolysis can be destructive to biological macromolecules. The chlorotrifluoroethyl radical, the distinguishing label, also demonstrates reaction selectivity towards aromatic residues, and the released bromine atom can propagate further radical reactions (Eckenhoff, 1996a; b; Eckenhoff *et al.*, 2000; Tang *et al.*, 2000; Ishizawa *et al.*, 2002; Chiara *et al.*, 2003).

To overcome these problems, photoactive anesthetic analogs containing diazirine or aryl azide moieties have been synthesized for multiple anesthetics. The chemotypes represented by these photolabels include haloalkanes (RG Eckenhoff *et al.*, 2002), long chain alcohols (Husain *et al.*, 1999; Addona *et al.*, 2002), etomidate (Husain *et al.*, 2003, 2006, 2010; Bright *et al.*, 2007), neurosteroids (Darbandi-Tonkabon *et al.*, 2003), haloethers (Xi *et al.*, 2006; Eckenhoff *et al.*, 2010), anthracene (Emerson *et al.*, 2013), alkylphenols (Hall *et al.*, 2010; Stewart *et al.*, 2011; Yip *et al.*, 2013), and barbiturates (Savechenkov *et al.*, 2012) (Figure 1). Incorporated photoactive groups undergo photolysis at lower energy wavelengths than halothane (~300-375 nm), limiting damage to biological samples upon irradiation. The chemical and pharmacologic properties of these analogs, including general anesthetic efficacy, are initially characterized to ensure reasonable mimicry of the parent compounds. Photolabeling studies with analogs are strengthened by confirmation that pharmacologic activity is conserved with the parent compound through parallel functional assays or competition experiments. Photolabeling

competition experiments hint at specificity or saturability of target binding sites, easing subsequent experimental investigations, but not necessarily designating a relevant role for the functional effects of the compounds.

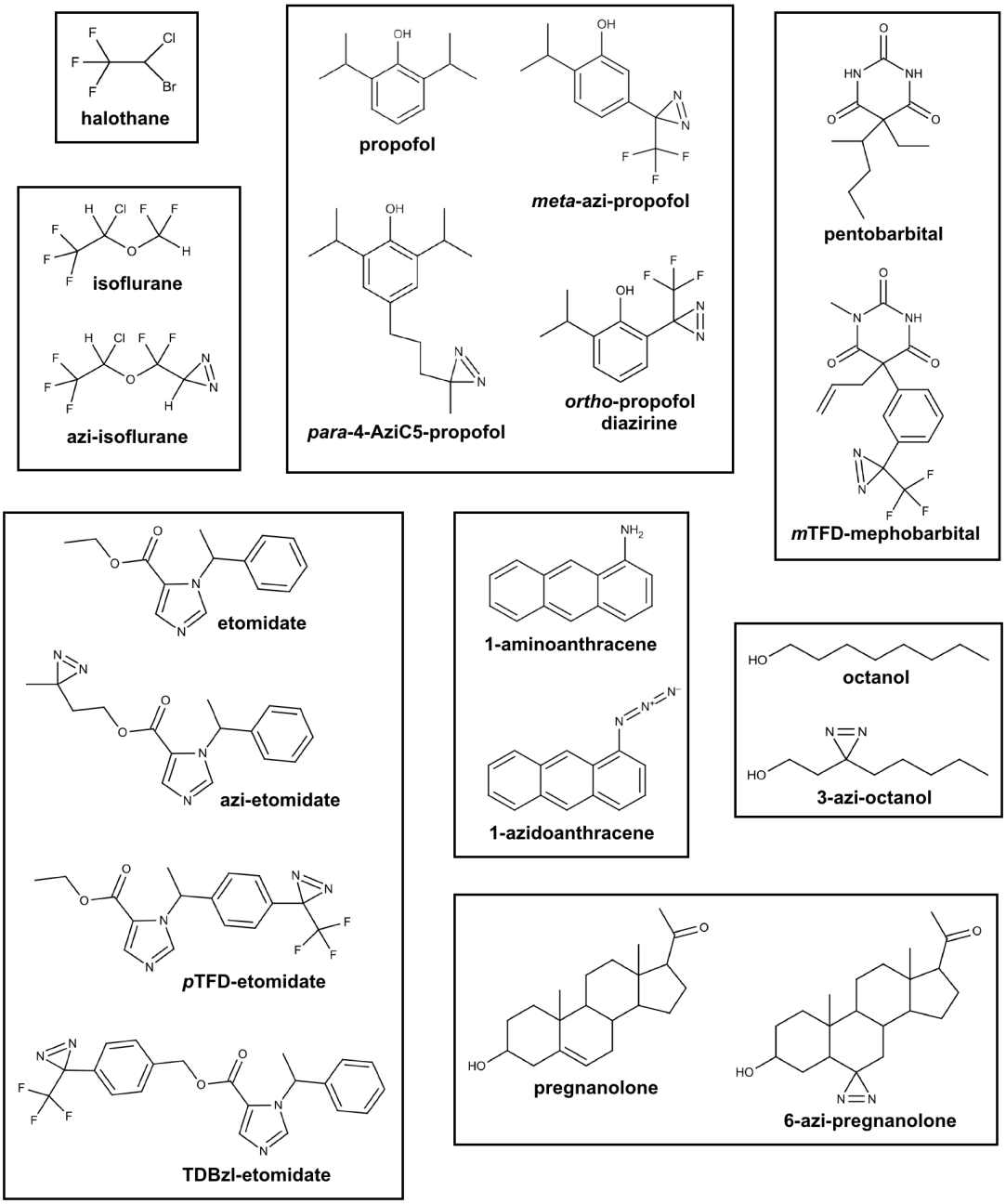

Figure 1. Chemical structures of general anesthetics and their photoactive analogs. With the exception of halothane, a diazirine or azido group serves as the photoactive moiety.

The diazirine moiety has generally been favored in anesthetic photolabel design. When placed adjacent to an electron-withdrawing group, especially a trifluoromethyl group, diazirine photolysis results in a single reactive intermediate, a singlet carbene, and an inert by-product, dinitrogen. This carbene intermediate simultaneously displays carbocation and carbanion characteristics, allowing both electrophilic and nucleophilic reactions, and enabling covalent attachment to proteins orders-of-magnitude faster than carbon-centered radicals (e.g., chlorotrifluoroethyl radical) (de Frémont *et al.*, 2009; Gerbig and Ley, 2013). The promiscuous reactivity of singlet carbenes is desired to reliably photolabel equilibrium binding sites, which can consist of chemically diverse side chain and backbone atoms, and photolabel promiscuity is suggested by adducting a broad range of residues, including aliphatic amino acids. Because general anesthetics can favorably assume multiple orientations in sites where interactions are mediated primarily by hydrophobic or van der Waals forces, photolabel attachment to multiple residues lining a pocket indicates a considerably dynamic ligand in the site.

1.4 Experimental Approach for the Discovery of Anesthetic Targets

An underlying theme throughout this thesis work is the experimental approach that utilizes general anesthetic photolabels. This approach proceeds with the following steps: (1) Photolabel development, which includes the design, synthesis, characterization, and pharmacologic validation of photoactive anesthetic analogs; (2) Use of photolabels to identify protein targets of anesthetics through unbiased proteomic approaches, followed by the identification of molecular binding sites; (3) Association of anesthetic binding with the alteration of a characteristic *in vitro* function of the identified protein; (4)

Demonstration of the relevance of altering protein function in organism physiology while an animal is anesthetized with a specific compound.

The primary aim of this work is to identify and implicate protein targets in anesthetic mechanisms, with primary focus on the anesthetic propofol and, to a lesser extent, 1-aminoanthracene. The unbiased proteomic approach in step (2) dictated that the proteins interrogated in step (3) and onwards were not defined at the start of this project. As target identification is dependent on ligand-protein binding, and is largely independent of protein function, the relevance of identified targets for on- or off-pathway pharmacologic mechanisms was also not predetermined. With this in mind, the initiation of the experimental approach and the pursuit of target relevance are described herein.

CHAPTER 2: PROPOFOL AND ALKYLPHENOL ANESTHETICS

2.1 Alkylphenol Anesthetic Pharmacology

Propofol (2,6-diisopropylphenol) is one of the most commonly used intravenous general anesthetics. In addition to propofol, other molecules of the same alkylphenol chemotype are also efficacious and potent general anesthetics (James and Glen, 1980; Krasowski *et al.*, 2001; Hall *et al.*, 2010; Stewart *et al.*, 2011). For example, 2-isopropopylphenol and the disubstituted compounds 3,5-dipropylphenol and 2,4-di-*sec*-butylphenol produce loss of righting reflex in tadpoles and/or mice within a 6-fold concentration range of propofol (James and Glen, 1980; Krasowski *et al.*, 2001). It is likely that the alkylphenol anesthetics share molecular binding partners and cause hypnosis through conserved mechanisms, and continuing to characterize the pharmacology of this chemotype should ultimately improve their use and development.

Central nervous system (CNS) depression by propofol is partially attributable to $GABA_A$ receptor potentiation (Jurd *et al.*, 2003); however, other ion channels that control neuronal excitability are modulated during alkylphenol anesthetic-induced hypnosis. Electrophysiological studies have demonstrated propofol inhibition of neuronal nicotinic acetylcholine receptors (Flood *et al.*, 1997; Violet *et al.*, 1997), suppression of sodium channel currents (Rehberg and Duch, 1999), and well-documented potentiation of glycine receptors, including evidence for their involvement in propofol hypnosis (Nguyen *et al.*, 2009). Additionally, propofol can alter G-protein coupled receptor signaling (Murasaki *et al.*, 2003), and propofol inhibits neurotransmitter release through SNARE-associated proteins (Herring *et al.*, 2011). With the exception of serum albumin and apoferritin

(Bhattacharya *et al.*, 2000; Vedula *et al.*, 2009), studies involving propofol binding to soluble proteins have thus far been limited.

2.2 *Meta*-Azi-Propofol (AziP*m*)

Similar to other general anesthetics, propofol has relatively low affinities for protein targets, with the reported highest affinity propofol-protein interactions having low micromolar dissociation constants (Vedula *et al.*, 2009). To aid the identification of propofol targets and binding sites, the Eckenhoff lab has developed a photoactive propofol analog called *meta*-azi-propofol (AziP*m*) (Figure 2) (Hall *et al.*, 2010). This compound contains a 2-isopropyl group and a trifluoromethyl-diazirine incorporated at the *meta* position of the phenol ring, and the peak absorbance of the diazirine, as measured with UV-Vis spectroscopy, is at ~370 nm. AziP*m* and propofol also have similar physicochemical properties (Table 1). As a validation that AziP*m* and propofol share conserved protein binding sites, the photolabel has been demonstrated to adduct residues within crystallographically-determined propofol sites on horse spleen apoferritin (Hall *et al.*, 2010), the *Gloeobacter* ligand-gated ion channel (GLIC) (Chiara *et al.*, 2014), and human serum albumin (unpublished data). Also, this ligand binds intersubunit transmembrane sites on $GABA_A$ receptors that are conserved with propofol and other anesthetics (Jayakar *et al.*, 2014), and AziP*m* potentiates $GABA_A$ receptor anionic current (Hall *et al.*, 2010). Importantly, similar to other alkylphenol analogs of propofol, AziP*m* is also a potent general anesthetic, producing anesthesia in tadpoles and mice within a two-fold concentration of propofol.

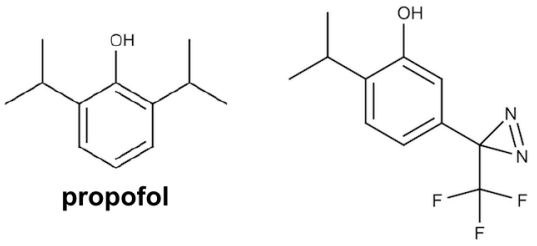

Figure 2. Chemical structures of propofol and AziP*m*.

Table 1. Physicochemical properties of propofol and AziP*m*

Compound	MW (Da)	Density (g/ml)[a]	LogP[a]	Dipole (D)[a]	Volume (Å^3)[b]
Propofol	178	0.96	3.79	1.70	192.5
AziP*m*	244	1.12	3.93	2.12	196.5

[a]Values derived from Hall *et al.*, 2010.
[b]Calculated with ChemAxon's MarvinSketch, v14.7.14.0.

2.3 AziP*m* Binding to Whole Brain

Alkylphenol general anesthetics are approximately two orders of magnitude more potent than volatile anesthetics. This could be due to higher affinities of the alkylphenols for drug targets and/or higher efficacies for modulating the function of critical substrates. One implication of higher affinity interactions is more selective binding to targets. To test the selectivity of binding, we characterized the macroscopic distribution of an alkylphenol anesthetic in its presumed target, the brain. Brain sections equilibrated and photolabeled with 0.1 μM [^{3}H]AziP*m* were exposed to x-ray film for autoradiography. We quantified binding to nine distinct brain regions (Figure 3A, Figure 3B, and Table 2). AziP*m* binding was widespread but heterogeneous, with the most heavily labeled regions approximately twice as intense as the least labeled. We compared the selectivity of

alkylphenol binding to that of the volatile anesthetic halothane (Table 2) (Eckenhoff and Eckenhoff, 1998). Overall, the relative selectivity of these chemically distinct anesthetics for each brain region was similar, and the largest differences were less than two-fold (Table 2).

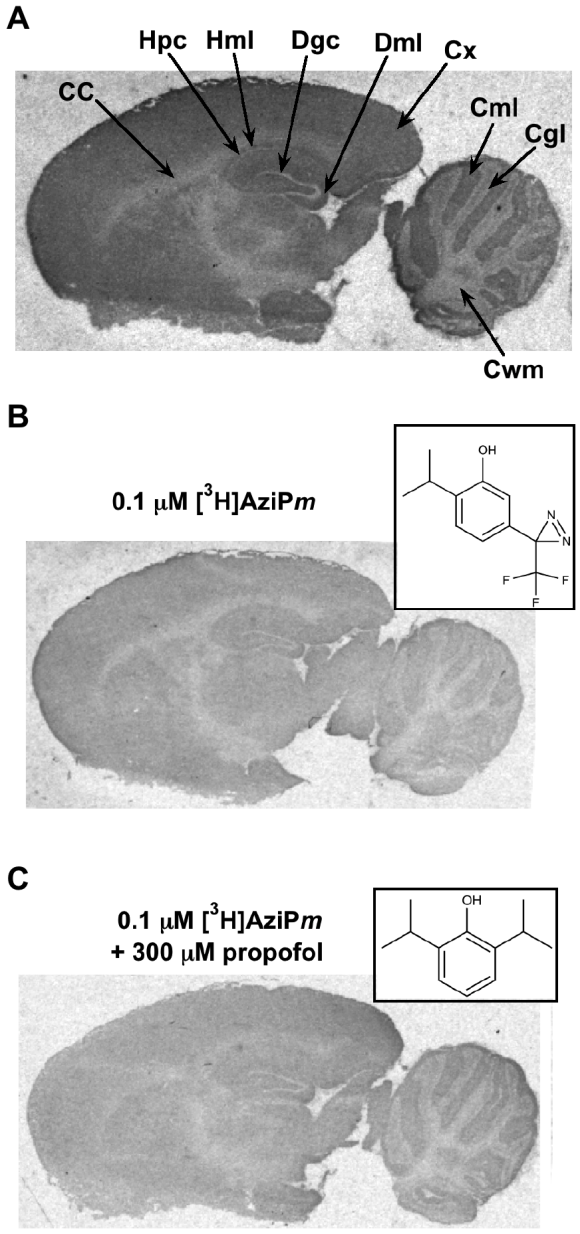

Figure 3. (A) Heavily contrasted autoradiograph of a sagittal brain section photolabeled with 0.1 μM [^{3}H]AziP*m*. Regions of interest are indicated: CC, corpus callosum; Hpc,

hippocampal pyramidal cell layer; Hml, hippocampal molecular layer; Dgc, dentate granule cell layer; Dml, dentate molecular layer; Cx, cortex; Cml, cerebellar molecular layer; Cgl, cerebellar granular cell layer; Cwm, cerebellar white matter. (B) Brain section photolabeled with 0.1 μM [^{3}H]AziP*m* or (C) [^{3}H]AziP*m* + 300 μM propofol. The insets depict (B) AziP*m* and (C) propofol. The sections in (B) and (C) were exposed to the same film and contrasted identically after development, and hence accurately portray relative levels of [^{3}H]AziP*m* binding.

Table 2. [^{3}H]AziP*m* binding to rat brain regions

Brain region	0.1 μM [^{3}H]AziP*m* (mO.D. ± SE)[a]	0.1 μM [^{3}H]AziP*m* + 300 μM propofol (mO.D. ± SE)	AziP*m* selectivity ratio[b]	Halothane selectivity ratio[c]
Cortex	215 ± 9	199 ± 11	0.14	0.13
Corpus callosum	147 ± 11	151 ± 7	0.10	0.12
Hippocampal molecular layer	199 ± 12	190 ± 11	0.13	0.13
Hippocampal pyramidal layer	168 ± 7	157 ± 7	0.11	0.10
Dentate molecular layer	212 ± 12	198 ± 7	0.14	0.12
Dentate granule cell layer	145 ± 7	141 ± 6	0.10	0.07
Cerebellar molecular layer	182 ± 6	178 ± 6	0.12	0.14
Cerebellar granular layer	118 ± 5	125 ± 2	0.08	0.07
Cerebellar white matter	100 ± 7	97 ± 5	0.07	0.12

[a]Milli-optical density (mO.D.) data is from (n = 4) brain sections for [^{3}H]AziP*m* and (n = 8) sections for [^{3}H]AziP*m* + propofol.
[b]Selectivity ratio calculated as region mO.D./sum of mO.D. from all the regions.
[c]Data for halothane derived from Eckenhoff and Eckenhoff, 1998.

The quantified brain regions can be combined into three compositions: (1) synapse-dense, (2) primarily cell bodies, and (3) primarily white matter (Table 3)

(Eckenhoff and Eckenhoff, 1998). Comparing combined data from each compositional class revealed that AziP*m* preferentially binds synapse-dense regions as compared to cell bodies or white matter (Table 3). Preferential binding suggests a general concentration of higher affinity substrates for alkylphenol anesthetics in these protein-rich areas. Maximal binding to synapse-dense regions was also seen for halothane, but halothane bound to white matter more strongly than did AziP*m* (Eckenhoff and Eckenhoff, 1998). Although binding does not necessarily imply functional association with the anesthetic endpoint, concentrated binding at synapses for both drugs is consistent with the consensus that the primary effect of general anesthetics is on transmission rather than conduction.

Table 3. [^{3}H]AziP*m* binding to rat brain by primary composition of regions

Brain region	0.1 μM [^{3}H]AziP*m* (mO.D. ± SE)
Molecular layers	202 ± 8[a]
Cortex	
Hippocampus	
Dentate gyrus	
Cerebellum	
Cell body layers	144 ± 15
Hippocampus pyramidal	
Dentate gyrus granule cell	
Cerebellar granular/Purkinje	
White matter	124 ± 24
Corpus callosum	
Cerebellum	

[a]Significantly greater binding in the molecular layers compared to cell body or white matter regions was determined with one-way ANOVA ($p = 0.01$) followed by Bonferroni post-hoc tests comparing all means and testing for significance with a family-wise error rate of 0.05. Values represent averages from 0.1 μM [^{3}H]AziP*m* binding in Table 2.

Pharmacologic specificity of alkylphenol sites on neuronal substrates can be indicated by inhibition of photolabeling by propofol. Therefore, we photolabeled brain

sections with 0.1 μM [^{3}H]AziP*m* while co-incubating with increasing concentrations of propofol (3-300 μM). We did not detect any significant change in total binding in any brain region, even with propofol concentrations 3000 fold higher than [^{3}H]AziP*m* (Table 2 and Figure 3C). We hypothesized that a high non-specific component of binding to lipid reduced the ability to detect saturable binding to protein in the whole brain section preparation, so we separately analyzed the specificity of alkylphenol anesthetic binding to both protein and lipid.

2.4 AziP*m* Binding to Synaptosomal Protein

Because [^{3}H]AziP*m* most selectively bound synapse-dense regions, we photolabeled rat synaptosomes *in vitro* with [^{3}H]AziP*m* ± propofol to test the specificity of binding to protein. SDS-PAGE and autoradiography revealed numerous targets, but selectivity was evident in that binding of [^{3}H]AziP*m* did not correlate with abundance as reflected by Coomassie intensity (Figure 4A). We also observed binding specificity, with inhibition of [^{3}H]AziP*m* protein photolabeling by only 100-fold higher concentrations of propofol (Figure 4A). Based on optical density measurements of the entire lanes, 400 μM propofol decreased 4 μM [^{3}H]AziP*m* binding to synaptosomal protein an average of 31%, with a maximum decrease of 57% in any individual band (Figure 4A). This suggested broad applicability for AziP*m* in examining propofol-protein interactions.

The autoradiograph signal normalized to the Coomassie intensity throughout the lanes revealed that, per amount of protein, higher molecular weight proteins were considerably more photolabeled than those of lower molecular weight (Figure 4B). Using

protein standards, molecular weight could reliably be estimated between 10-250 kDa. In the absence of competing propofol, [^{3}H]AziP*m* photolabeled 115-250 kDa protein proportionally with only a small dependence on protein molecular weight (Figure 4C). Less than 115 kDa, however, this trend was intermittently disrupted, presumably by abundant proteins without specific binding sites. Our interpretation is that larger polypeptides, because of larger surface area and folds (Liang *et al.*, 1998), are statistically more likely to contain the structural features that constitute a specific binding site for the small alkylphenol anesthetics, whereas these features become progressively less likely as the proteins become smaller. A similar dependence of chain length on the creation of specific halothane binding sites has previously been demonstrated with model polypeptides (Johansson and Eckenhoff, 1996).

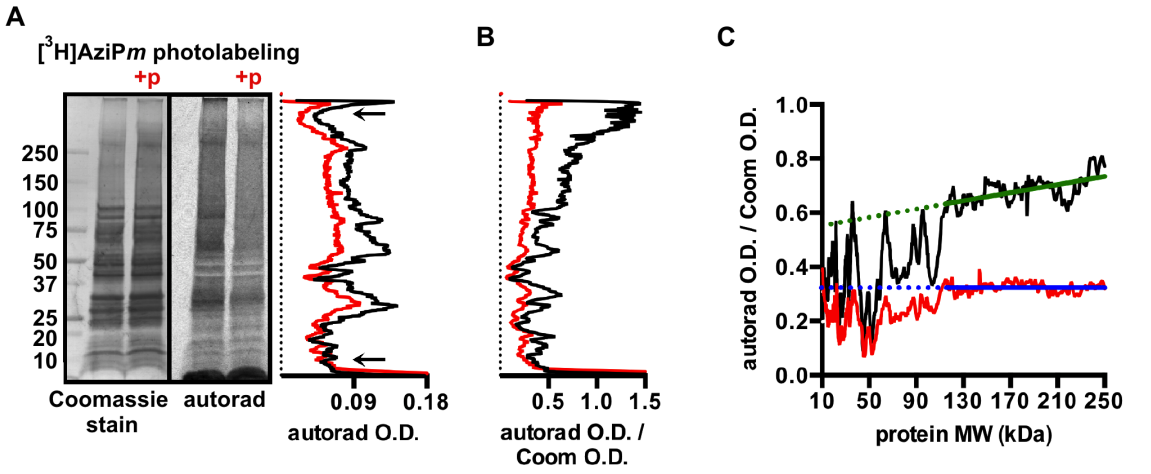

Figure 4. (A) Coomassie-stained PVDF membrane and corresponding autoradiograph of synaptosomal protein photolabeled with 4 μM [^{3}H]AziP*m* or 4 μM [^{3}H]AziP*m* + 400 μM propofol, with the latter indicated as +p. On the right, the optical density (O.D.) profiles of the lanes are shown, with [^{3}H]AziP*m* shown in black, and [^{3}H]AziP*m* + propofol shown in red. Between the arrows in the lanes, propofol inhibited [^{3}H]AziP*m* photolabeling by an average of 31%. (B) Autoradiograph O.D. normalized to Coomassie O.D. for the membrane and autoradiograph shown in (A). Data for [^{3}H]AziP*m* and [^{3}H]AziP*m* + propofol are again shown in black and red, respectively. (C) The 10-250

kDa portion of the [^{3}H]AziP*m* (black) and [^{3}H]AziP*m* + propofol (red) traces from (B) are shown. Linear regression was used to fit straight lines (shown in green and blue) through the data between 115-250 kDa, and the traces were extended with the dashed line to 10 kDa. R^2 was 0.38 and 0.00 for the green and blue fits, respectively.

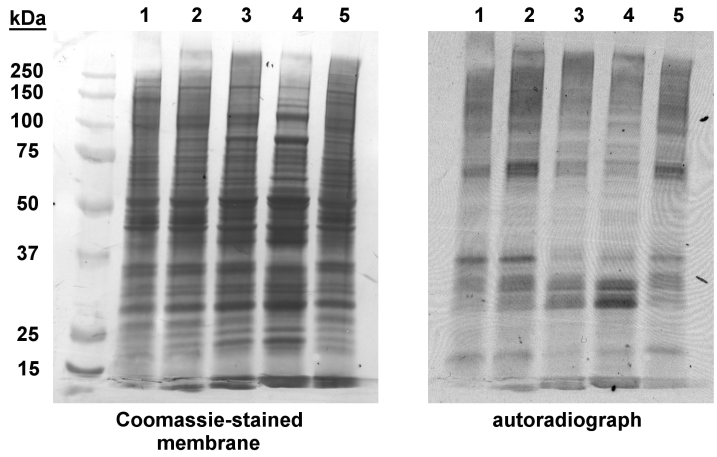

Figure 5. Coomassie-stained membrane and corresponding autoradiograph of mouse brain fractions (Dunkley *et al.*, 2008) photolabeled with [^{3}H]AziP*m*: 1, miscellaneous cellular membranes; 2, myelin; 3, synaptosomes; 4, mitochondria; 5, brain homogenate.

In brain sections, high affinity binding to few proteins could have manifested as a highly selective drug distribution that mimics the expression of those targets. For example, if alkylphenols uniquely bound $GABA_A$ receptors, a presumed functional target for these drugs, we would have expected greatest AziP*m* photolabeling in the cerebellar granule layer where functional $GABA_A$ receptors are most abundant (Palacios *et al.*, 1981; Bowery *et al.*, 1987). This would also have manifested as peak [^{3}H]AziP*m* intensity only at ~60 kDa on the SDS-PAGE autoradiograph. However, the brain sections and SDS-PAGE gel together demonstrate the presence of many proteins that selectively and specifically bind alkylphenol general anesthetics, and there are also numerous AziP*m* targets not present in synaptosomes (Figure 5). Identification of these many photolabeled

proteins will require purification of photolabeled protein or comprehensive protein sequencing to detect AziP*m* covalent adducts.

2.5 AziP*m* Binding to Neuronal Lipids

To characterize alkylphenol anesthetic binding to rat brain lipids, we isolated the major phospholipid species and cholesterol after photolabeling brain homogenate with 1 μM [^{3}H]AziP*m*. [^{3}H]AziP*m* exhibited statistically significant selectivity for photolabeling phosphatidylethanolamines (PE) as compared to the other lipids (Table 4). [^{3}H]AziP*m* binding to PE also increased in the presence of 400 μM propofol, in contrast to the other lipids, which showed no change in binding (phosphatidylcholines (PC) and cholesterol) or a 50% decrease (phosphatidylserines/phosphatidylinositol/sphingomyelin (PS/PI/SPH) combined). Because of the abundance of PE, it seems clear that the inability of propofol to displace [^{3}H]AziP*m* binding from brain slices was likely due to this over-abundance of non-specific sites, and that competition of labeling from proteins in brain sections is compensated for by this cooperative effect in the lipid fraction.

Table 4. [^{3}H]AziP*m* binding to major rat brain lipids

Lipids	Rf value	pmol [^{3}H]AziP*m* binding per μmol lipid	Fold change with 400 μM propofol co-incubation
PE	0.7 ± 0.1	102.1 ± 24.1[a]	1.7 ± 0.2
PC	0.4 ± 0.1	36.5 ± 10.6	0.9 ± 0.2
PS/SPH/PI	0.2 ± 0.1	27.0 ± 10.8	0.4 ± 0.1
Cholesterol	1	0.8 ± 0.1	1.2 ± 0.2

[a]Significantly greater [^{3}H]AziP*m* binding to PE compared to PC, PS/SPH/PI, and cholesterol was determined with one-way ANOVA ($p = 0.002$) followed by Bonferroni post-hoc tests comparing all means and testing for significance with a family-wise error rate of 0.05. Mean values are from ($n = 4$) experiments per lipid.

Of the dominant lipid fractions, PE is charged and polar and is thought to hydrogen bond to membrane proteins. Because the alkylphenols distribute in the headgroup region of lipid bilayers (Hansen *et al.*, 2013; Arcario *et al.*, 2014), the phenol hydroxyl may better hydrogen bond to PE, explaining the selectivity of binding. In separate experiments, we determined that 16 ± 3% of [^{3}H]AziP*m* that covalently bound to PE had incorporated into the polar headgroup, as compared to only 5 ± 1% for both PC and PS/PI/SPH. Thus, at least in the absence of propofol, alkylphenols partially distribute to different membrane depths that are dependent upon adjacent phospholipid species. The cooperativity of AziP*m* photolabeling of lipids in the presence of excess propofol might arise from displacement of [^{3}H]AziP*m* from adjacent protein sites, or through alterations in bilayer structure or dynamics that permit greater access of the photolabel to these headgroup regions (Tsuchiya, 2001; Bahri *et al.*, 2007; Hansen *et al.*, 2013). The implications of this complex shifting of ligands between macromolecular pools are not clear, but emphasize that ligand-ligand interactions and the concentration-dependence of ligand actions could be far more complex than conventionally modeled.

CHAPTER 3: PROPOFOL INTERACTIONS WITH SIRT2 DEACETYLASE

3.1 Rationale and Introduction to SIRT2

Proteins involved in neurotransmission are among the pharmacologic targets that are affected by propofol to cause hypnosis (Jurd *et al.*, 2003; Kretschmannova *et al.*, 2013), and characterizing the interactions between propofol and these proteins should allow the rational design of new hypnotics that specifically target relevant binding sites. Designing ligands with greater selectivity for specific sites should also alleviate side effects caused by propofol binding to off-pathway protein targets that do not contribute to hypnosis. As previously noted, propofol has been reported to cause multiple adverse neurological side effects in mammals (Patel *et al.*, 2003; Zhang *et al.*, 2009; Whittington *et al.*, 2011; Creeley *et al.*, 2013); however, the molecular targets underlying their causes are not clear. Therefore, comprehensive knowledge of propofol substrates in all CNS tissue types is necessary to improve drug action.

In this chapter, we used AziP*m* to investigate alkylphenol-anesthetic binding in a myelin-enriched fraction from rat brain. We identified the sirtuin protein SIRT2 as a specific target of propofol and AziP*m.* There are seven mammalian sirtuins (SIRT1-7) that are traditionally known as Class III histone deacetylases (HDACs), although this class of proteins is evolutionarily and structurally unrelated to the classical HDAC proteins (HDAC1-11). During enzymatic catalysis, SIRT2 couples deacetylation of acetyl-lysine with NAD^+ hydrolysis, which results in the formation of O-acetyl-ADP-ribose and nicotinamide; nicotinamide is also a feedback inhibitor of the enzyme. We found that clinical concentrations of propofol inhibit this enzymatic function of SIRT2,

and we characterized the allosteric protein site that propofol binds. Possible physiological implications for SIRT2 inhibition by propofol are also discussed.

3.2 Identification of SIRT2 as a Propofol Target

We isolated a myelin-enriched fraction from rat brain for photolabeling with 4 μM [^{3}H]AziP*m*, a concentration that approximates the EC_{99} dose for anesthetizing tadpoles. To measure the specificity of anesthetic binding, we also photolabeled with 4 μM [^{3}H]AziP*m* while co-equilibrating with 400 μM propofol or 180 μM (non-tritiated) AziP*m*, which are concentrations that approach their maximum aqueous solubility. The protein was separated by SDS-PAGE and transferred to a membrane for autoradiography. Based on optical density from the radioactivity (Figure 6B), propofol and AziP*m* inhibited [^{3}H]AziP*m* binding to myelin proteins an average of 41% and 53%, respectively, throughout the lanes. [^{3}H]AziP*m* incorporation was concentrated in four bands shown as peaks at (1) >250 kDa, (2) 80-95 kDa, (3) 55-70 kDa, and (4) 35-40 kDa, and propofol decreased [^{3}H]AziP*m* labeling of these peak regions by 50-69%.

The >250 kDa band did not enter the resolving gel and was likely aggregated protein; however, the high selectivity of photolabeling in the remaining bands suggested strong binding to few proteins. To identify these proteins, we photolabeled myelin with 4 μM AziP*m* and excised the bands from a separate SDS-PAGE gel (Figure 6C). We then employed a mass spectrometry-based approach whereby we first identified all the proteins in the bands, then searched for an AziP*m* mass adduct (~216 Da) on those proteins. Six unique peptides from trypsin- and chymotrypsin-digested samples of the 35-

40 kDa band were identified as photolabeled by AziP*m* (Table 5 and Appendix A2.1), and these peptides were all assigned to SIRT2. With this approach, we did not identify adducts on proteins from the other bands and therefore pursued the relevance of propofol binding to SIRT2.

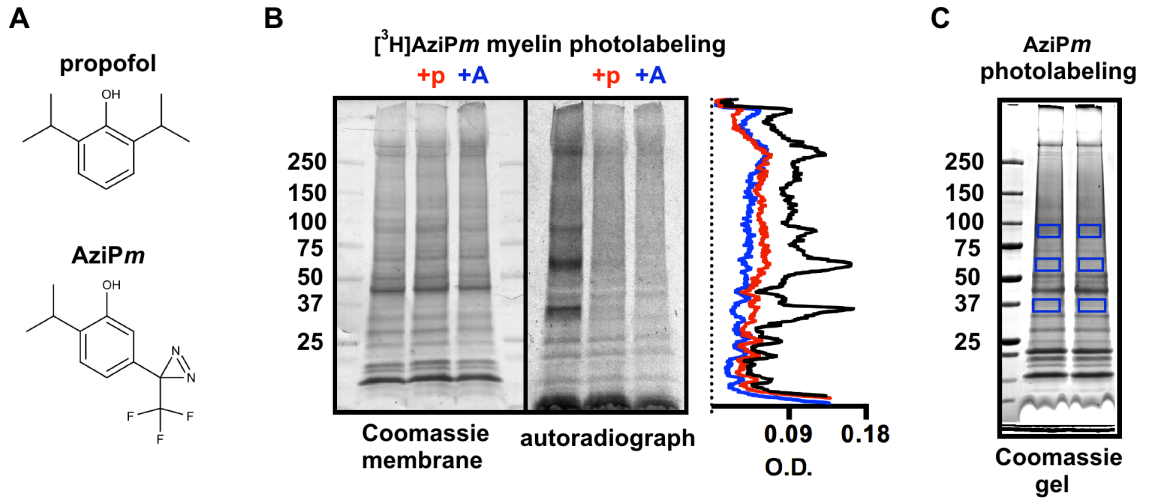

Figure 6. (A) Chemical structures of propofol and AziP*m*. (B) Coomassie-stained membrane and corresponding autoradiograph of 50 µg myelin protein separated with SDS-PAGE after photolabeling with 4 µM [^{3}H]AziP*m* ± 400 µM propofol (+p) or 180 µM AziP*m* (+A). Optical density (O.D.) quantification from the autoradiograph lanes is shown in the aligned traces. (C) Coomassie-stained gel of 50 µg myelin protein separated with SDS-PAGE after photolabeling with 4 µM (non-tritiated) AziP*m*. The boxed gel regions were excised for LC-MS/MS and processed with either trypsin or chymotrypsin digestion as described in the text.

Table 5. SIRT2 peptides photolabeled by AziP*m*

Photolabeled peptide	Peptide charge	Observed MH+	Calculated MH+	Enzyme used
^{131}F.FALAKELY$^{\#}$PGQF.K^{144}	+2	1599.8101	1599.8069	chymo
^{132}F.ALAKELY$^{\#}$PGQF.K^{144}	+2	1452.7406	1452.7385	chymo
^{134}L.AKELY$^{\#}$PGQF.K^{144}	+2	1268.6200	1268.6173	chymo
^{136}K.ELY$^{\#}$PGQFK.P^{145}	+1	1197.5819	1197.5802	trypsin
^{172}L.ERVAGLEPQDLVEAHGTF$^{\#}$Y.T^{192}	+3	2347.1260	2347.1216	chymo
^{202}K.EYTM$^{\#}$SWMK.E^{211}	+1	1291.5378	1291.5349	trypsin

$^{\#}$Indicates a 216.0762 Da modification was detected. Amino acid numbering is according to full-length rat SIRT2.

3.3 Conformation-Specific Propofol-SIRT2 Binding

After photolabeling separate myelin samples, we confirmed that propofol concentration-dependently inhibited 4 μM [^{3}H]AziP*m* photolabeling of the ~37 kDa SIRT2 band (Figure 7A). We then photolabeled purified recombinant human SIRT2 with 4 μM [^{3}H]AziP*m* ± propofol to test the specificity of binding in solution. Human and rat SIRT2 are highly conserved and share 88% sequence identity, and thus it was surprising when our initial attempts to inhibit [^{3}H]AziP*m* photolabeling of human SIRT2 with propofol were unsuccessful (Figure 7B).

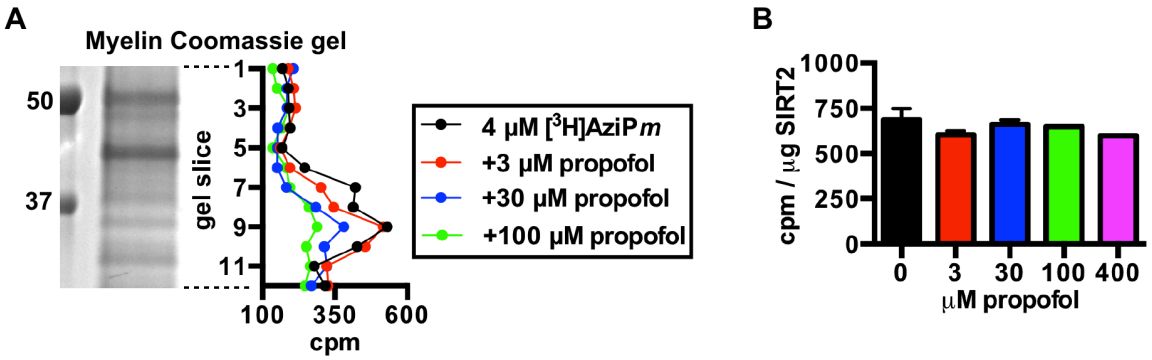

Figure 7. (A) Representative Coomassie-stained gel lane of myelin protein separated with SDS-PAGE after photolabeling with 4 μM [^{3}H]AziP*m* ± 3, 30, or 100 μM propofol. Each gel lane was cut horizontally into 1 mm pieces, and the radioactivity content in each slice is shown in the aligned graph. (B) Shown are the levels of covalent [^{3}H]AziP*m* binding to human SIRT2 in solution. In this experiment, SIRT2 was photolabeled with 4 μM [^{3}H]AziP*m* ± the indicated concentrations of propofol, and no additional substrates were added. Each mean was derived from 3-6 values from separate photolabeling experiments.

To investigate these contrasting results, we analyzed the AziP*m* binding site on high-resolution structures of SIRT2, which are also derived from recombinant human protein. The crystal structures of human SIRT2 represent two enzymatic conformations. The first is an inactive conformation, with SIRT2 bound only to its structural, non-

catalytic cofactor zinc (Finnin *et al.*, 2001; Moniot *et al.*, 2013). The second conformation represents an active enzyme bound to zinc, acetate, and ADP-ribose, with the latter in the cleft occupied by NAD^+ during enzymatic catalysis (Moniot *et al.*, 2013). When active, the helical domain containing the zinc subdomain is rotated over the NAD^+ cleft, hinging on loops that connect to the Rossmann-fold domain (Moniot *et al.*, 2013). AziP*m* photolabeled Tyr139, Phe190, and Met206 on the helical domain of rat SIRT2, and these residues converge in the folded protein at a single site (Figures 8A and 8B). AziP*m* photolabeling of multiple SIRT2 residues suggests that the ligand is somewhat mobile in the site. The portion of the cavity containing Tyr139 is also dynamic, being part of the flexible loop that connects the Rossmann-fold domain to the helical domain (Moniot *et al.*, 2013).

Although the photolabeled residues are similarly positioned in both SIRT2 conformations, the protein topology revealed that these amino acids surround a cavity that is present in the active conformation, but that is absent in the inactive conformation (Figures 8A, 8B, and 8C). The volume of this cavity is ~360 $Å^3$ and should therefore accommodate propofol and AziP*m*, which have van der Waals volumes of 192 $Å^3$ and 197 $Å^3$, respectively. Residues that line this cavity are identical in rat and human SIRT2, with the exception of rat Met206, which is a leucine in the human protein (Figure 8D).

This suggested that [^{3}H]AziP*m* and propofol might bind specifically only to the active conformation of SIRT2. To test this experimentally, we photolabeled recombinant human SIRT2 while co-incubating with >10 fold concentration (mol to mol) of acetylated human histones, which are protein substrates of SIRT2, and excess ADP-ribose and nicotinamide, which together mimic the co-substrate NAD^+ (Figure 9A). Simultaneous

binding of these substrates should increase the equilibrium fraction of SIRT2 that assumes the active conformation without allowing for enzymatic catalysis (Avalos *et al.*, 2004). As predicted with modeling, [^{3}H]AziP*m* photolabeling of SIRT2 significantly increased when the enzyme was co-equilibrated with these substrates, and propofol readily displaced [^{3}H]AziP*m* from active human SIRT2 (Figure 9B).

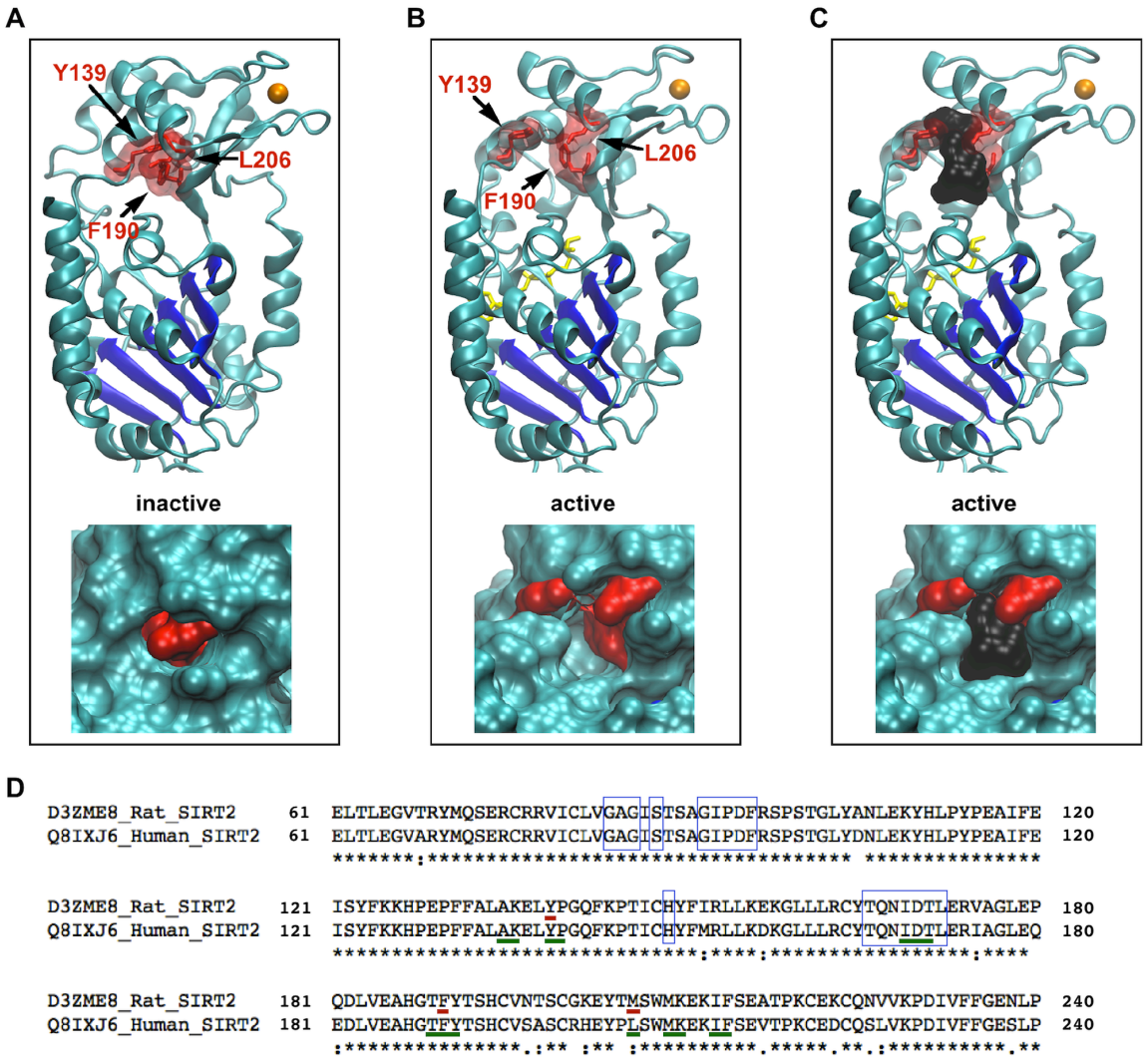

Figure 8. (A), (*top*) The positions of SIRT2 residues that are photolabeled by AziP*m* are shown in the structure of the inactive conformation. The Rossmann fold of SIRT2 is colored dark blue, zinc is colored orange, and the indicated photolabeled residues are shown as red sticks outlined by a transparent surface topology. (*bottom*) Enlarged view of

the photolabeled residues on the SIRT2 structure, but with the solid surface topology of the protein shown. (B) Identical views as in (A), but with the structure of the active SIRT2 conformation. ADP-ribose is colored yellow. (C) The cavity in the structure of the active conformation of SIRT2 is shown with a black surface representation, which has a volume of 364 $Å^3$. (D) Part of the human and rat SIRT2 sequences, which were derived from the indicated UniProt codes, are aligned. Identical residues are indicated by the asterisks, residues photolabeled by AziP*m* are underlined in red, residues lining the anesthetic cavity in active SIRT2 are underlined in green, and boxed residues form the protein C-pocket.

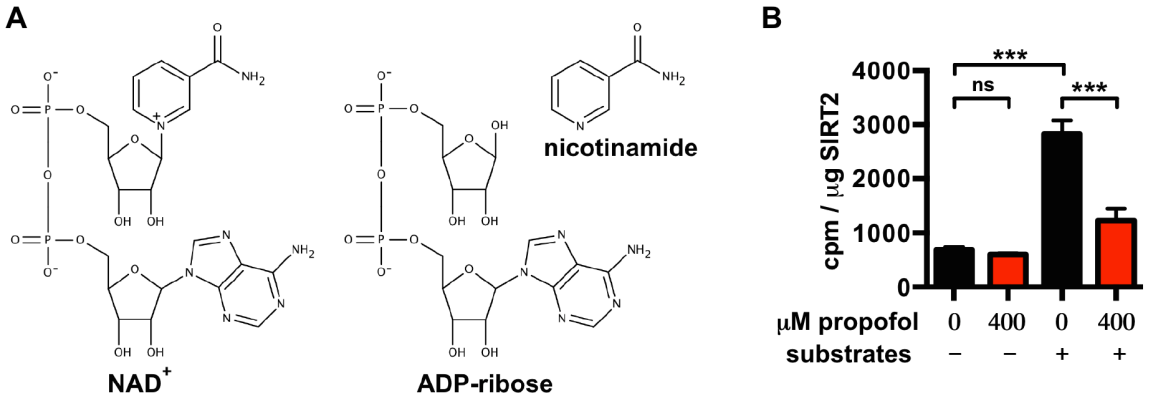

Figure 9. (A) Chemical structures of NAD^+, ADP-ribose, and nicotinamide. (B) The levels of covalent [^{3}H]AziP*m* binding to human SIRT2 in solution are shown, as in Figure 7B. However, in this experiment, SIRT2 was photolabeled with 4 µM [^{3}H]AziP*m* ± propofol and also ± substrates (acetylated histones, ADP-ribose, and nicotinamide). Each mean was derived from 3-6 values from separate experiments. 2-way ANOVA determined a significant effect of propofol and substrates on the means and their interaction ($p < 0.001$ for all comparisons). Bonferroni's post hoc tests comparing the indicated means determined that the substrates significantly increased [^{3}H]AziP*m* binding ($p < 0.001$), and that this binding was inhibited by propofol ($p < 0.001$).

3.4 Inhibition of SIRT2 by Propofol

To test whether propofol affects SIRT2 enzymatic activity, we measured SIRT2 deacetylation of acetylated α-tubulin that was derived from mammalian tissue (North *et al.*, 2003; Borra *et al.*, 2004). For this, we first prepared a soluble extract from rat brain that contained only a small amount of native SIRT2 (Figure 10A). Deacetylation of α-

tubulin in this soluble extract was accelerated by the addition of recombinant human SIRT2 and 1 mM NAD^+, and enzymatic activity was prevented by the sirtuin inhibitor nicotinamide (Figure 10B). The inability of other sirtuins to deacetylate α-tubulin (North *et al.*, 2003), and the addition of the histone deacetylase inhibitor trichostatin A to all reactions, ensured deacetylation was SIRT2-dependent.

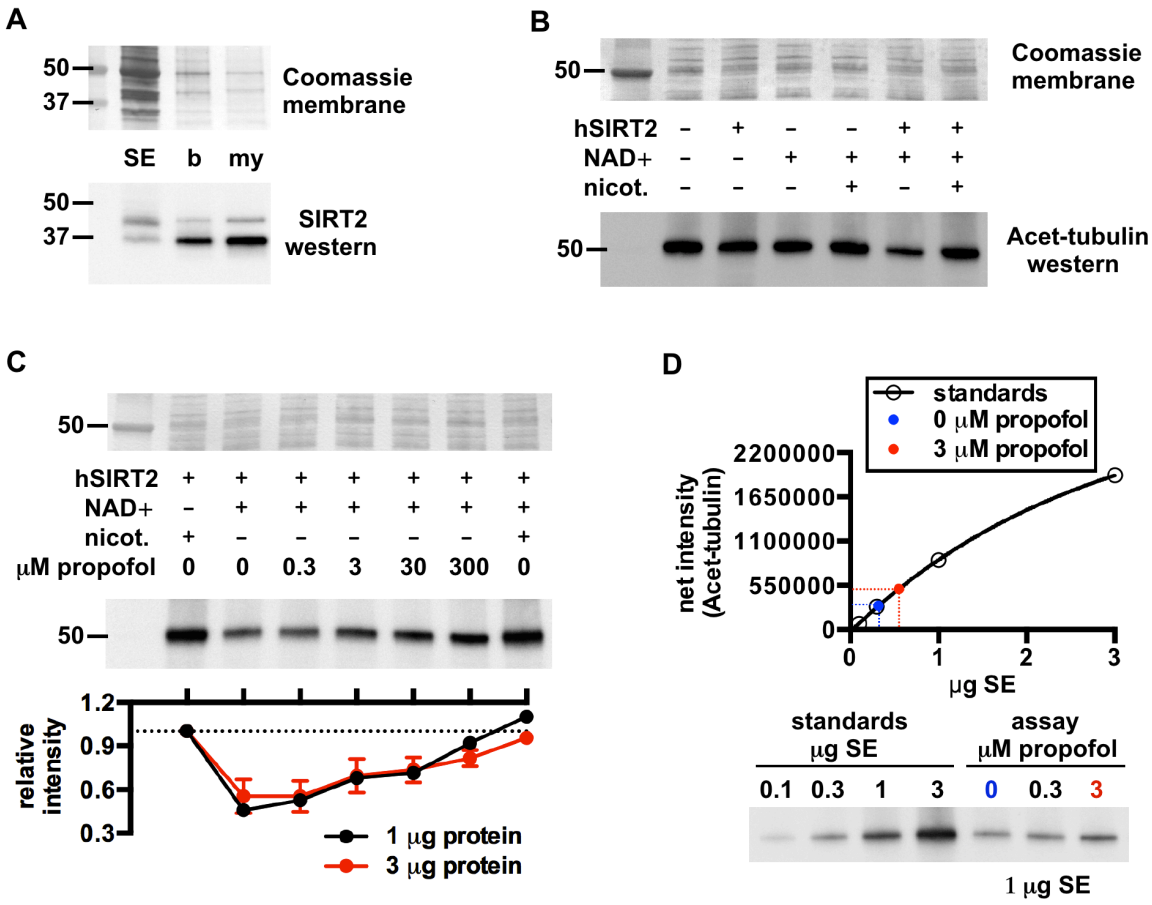

Figure 10. (A) Western blot showing relative amounts of SIRT2 in rat brain fractions: SE, soluble brain extract; b, brain homogenate; my, myelin. The Coomassie-stained membrane is shown for loading. (B) Western blot demonstrating deacetylation of acetylated α-tubulin from rat brain by recombinant human SIRT2 (hSIRT2). In this assay, SIRT2 activity was pronounced with the addition of 3 μg SIRT2 and 1 mM NAD^+, and deacetylase activity was inhibited by the SIRT2 inhibitor nicotinamide; the HDAC inhibitor trichostatin A was added to all reactions. 3 μg soluble extract protein from the assay was loaded in each lane for this blot. (C) Propofol concentration-dependently

inhibited SIRT2 deacetylation of acetylated α-tubulin. Assays were performed similar to (B) with the indicated substrates ± propofol. (D) Representative standard curve from a western blot used to determine absolute levels of acetylated α-tubulin deacetylation by SIRT2 in the absence and presence of propofol. For this, increasing amounts of soluble brain extract protein were separated via SDS-PAGE, and alongside this, 1 μg of protein from SIRT2 deacetylase assays that contained no inhibitor, 0.3 μM propofol, or 3 μM propofol. Densitometry from the standards allowed generation of the standard curve, from which absolute levels of deacetylase activity in the assay samples were determined.

With this assay, we observed concentration-dependent inhibition of SIRT2 activity by propofol (Figure 10C), including at the anesthetic concentration of 3 μM (Hall *et al.*, 2010). To quantify the absolute inhibition of SIRT2 activity by propofol, we accounted for the nonlinearity of the western blot chemiluminescent signal intensity. We generated internal standard curves by loading increasing amounts of soluble extract protein on a gel, and alongside this, we loaded the soluble extract from enzymatic assays (Figure 10D). In the absence of an inhibitor, 70 ± 2% of total acetylated α-tubulin was deacteylated in the assay, and 3 μM propofol inhibited SIRT2 deacetylase activity by 33 ± 4%.

Finally, because general anesthetics can affect tubulin polymerization (Emerson *et al.*, 2013), and because acetylation of α-tubulin is used as a surrogate for microtubule stability, we confirmed that propofol inhibition of SIRT2 was independent of tubulin polymerization state. The microtubule stabilizing agent epothilone D (Ballatore *et al.*, 2012) was added to separate assays at a concentration of 2 μM, which is sufficient to increase microtubule stability *in vivo* (Emerson *et al.*, 2013). Epothilone D did not affect SIRT2 deacetylation of α-tubulin, nor did it affect propofol inhibition of SIRT2 (Figure

11). This is consistent with observations that SIRT2 deacetylation of α-tubulin is not affected by co-incubation with taxol (North *et al.*, 2003).

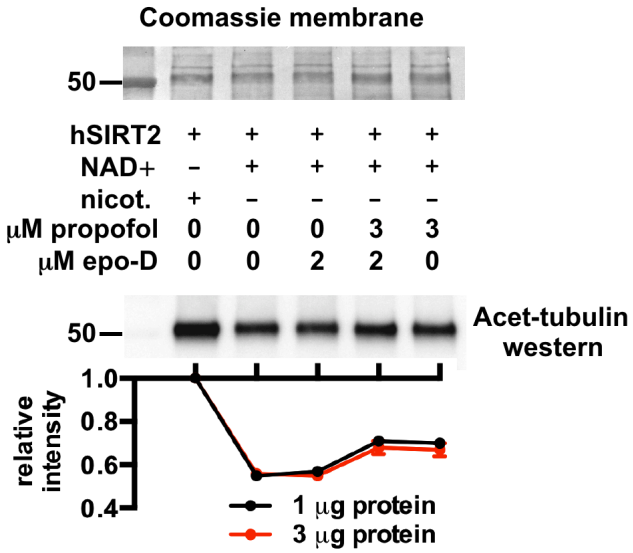

Figure 11. SIRT2 deacetylase assay western blot and quantification, as in Figure 10C, but with the microtubule stabilizing agent epothilone D added to some reactions. Epothilone D did not affect SIRT2 deacetylase activity or propofol inhibition of SIRT2.

3.5 A Unique Sirtuin Inhibitory Site

Despite the allosteric nature of this site, three residues that line the propofol site (Ile169, Asp170, and Thr171) also line the protein "C-pocket" that is highly conserved across sirtuins (Figure 8D) (Avalos *et al.*, 2004, 2005). Ile169 and Asp170 specifically contact the nicotinamide moiety of NAD^+ during enzymatic reactions (Avalos *et al.*, 2004, 2005), and mutagenesis of Asp170 reduces enzymatic activity (Finnin *et al.*, 2001). These residues are also adjacent to the acetyl-lysine substrate site (Avalos *et al.*, 2002; Moniot *et al.*, 2013). When bound, propofol is therefore suitably positioned to perturb the stability of the contacts that are critical for enzymatic catalysis. An alternative inhibitory mechanism is that propofol might inhibit enzyme cycling from the active conformation

back into the inactive conformation. Inhibition through binding to the active conformation is consistent with uncompetitive inhibition. Propofol does not bind within the C-pocket itself, in contrast to other sirtuin inhibitors such as nicotinamide (Avalos *et al.*, 2005) and Ex-527 (Napper *et al.*, 2005; Gertz *et al.*, 2013). The uniqueness of the propofol site was first demonstrated by the lack of competition between AziP*m* and nicotinamide for SIRT2 binding (Figure 9B). This can also be modeled by aligning the SIRT2 C-pocket to those of sirtuins co-crystallized with nicotinamide and Ex-527 (Figure 12). The residues photolabeled by AziP*m* are ~7-14 Å from nicotinamide and Ex-527, and the ligands are separated from these residues by a tunnel that constricts to ~4 Å in diameter in the SIRT2 protein.

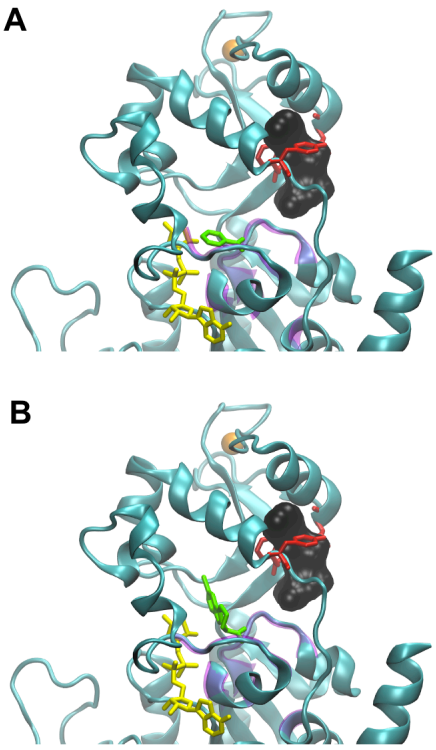

Figure 12. In (A) and (B), the active SIRT2 structure is shown in cyan, zinc is colored orange, ADP-ribose is colored yellow, and residues photolabeled by AziP*m* are shown as red sticks. The propofol binding cavity is filled with the black surface representation. For

(A), the C-pocket residues of SIRT2 were aligned to the C-pocket residues of Sir2Tm (PDB code 1YC5). The alignment root mean square was 0.75 Å, and the Sir2Tm C-pocket residues are traced in the transparent magenta cartoon. In 1YC5, Sir2Tm is bound to nicotinamide, and the position of this inhibitor, which binds to a separate site than propofol, is shown as green sticks. (B) The C-pocket residues of SIRT2 were aligned to those of SIRT3 (PDB code 4BV3). The alignment root mean square was 0.26 Å, and the SIRT3 C-pocket residues are traced in the transparent magenta cartoon. In 4BV3, SIRT3 is bound to the inhibitor Ex-527, which binds to the same site as nicotinamide, and is shown as green sticks.

3.6 Relevance of SIRT2 Inhibition by Propofol

As a soluble protein that is not known to directly affect neuronal excitability, it seems unlikely that propofol-SIRT2 interactions would contribute to hypnosis; therefore, the relevance of SIRT2 binding and enzymatic inhibition in myelin and elsewhere is likely as an off-pathway target of the drug. Although we used acetylated α-tubulin as a model substrate in our assays, there are numerous other proteins and cellular processes that are regulated by SIRT2, and essentially any cellular event regulated by acetylation state might therefore be influenced by propofol. For example, as a major deacetylase in oligodendrocytes (Li *et al.*, 2007; Southwood *et al.*, 2007; Werner *et al.*, 2007), SIRT2 activity regulates the development of myelin and also re-myelination of axons after crush injury (Beirowski *et al.*, 2011). In other cell types, SIRT2 deacetylates transcription factors (Liu *et al.*, 2012) and histones (Vaquero *et al.*, 2006, 2007; Vempati *et al.*, 2010) to regulate transcription and chromatin structure, and SIRT2 regulates metabolic enzyme function (Jiang *et al.*, 2011). Specific propofol binding only to active SIRT2 in solution also raises intriguing questions about the conformation of the enzyme in myelin. In order for [^{3}H]AziP*m* to bind strongly and specifically to myelin SIRT2 (Figure 6B), there must

be a significant fraction of SIRT2 in adult myelin that is complexed with substrates or is otherwise induced into a conformation more similar to the active form than the inactive.

In addition to SIRT2, there remain other proteins in myelin and other CNS tissue fractions that bind to propofol and have not yet been identified. In the approach taken in this chapter, identification of photolabeled protein was contingent on identifying AziP*m* mass adducts on peptides. The advantage of this strategy is that most proteins are retained in the SDS-PAGE gel and can potentially be identified, which is in contrast to other approaches such as IEF/SDS-PAGE that aim to purify photolabeled protein (see Chapter 4). However, adduct identification is also contingent on extensive sequencing of proteins. Soluble peptides are favored with LC-MS/MS sequencing, hindering detection of presumed hydrophobic propofol sites, and extensive sequencing becomes more challenging for larger proteins. Therefore, although our approach was successfully implemented for SIRT2 identification, this work also demonstrates the challenges associated with unbiased identification of unknown anesthetic protein targets.

CHAPTER 4: ALKYLPHENOL ANESTHETIC BINDING AND MODULATION OF MITOCHONDRIAL VDAC

4.1 The Tadpole as a Model Organism

The tadpole is typically used as a model for measuring general anesthetic potency. Anesthetics can be dissolved in the pond water, from which they are passively absorbed into the CNS, and passage across the gills and skin and the blood brain barrier are determined by the same physicochemical parameters (Downes and Courogen, 1996; Krasowski *et al.*, 2001). An equilibrium is achieved between the drug in the water and the drug in the plasma, and concentrations needed to anesthetize tadpoles are on the same order of magnitude as plasma concentrations needed to anesthetize humans (Downes and Courogen, 1996).

Several unambiguous phenotypic endpoints can be quantified when tadpoles are equilibrated with an anesthetic and become anesthetized. These endpoints include immobility (i.e., the tadpoles stop swimming) and loss of response to noxious stimuli. These endpoints can be measured during induction, when the anesthetic is administered to the tadpoles, and also emergence, when the tadpoles are placed into fresh water and the general anesthetic diffuses out from its body.

We performed experiments in which we photolabeled *Xenopus laevis* tadpoles *in vivo*. Photolabeling live, anesthetized organisms ensured that the proteins were in a functional state, and also that the ligand concentrations were aligned to the anesthetic endpoint. These experiments were performed for two purposes: (1) to investigate *in vivo* targets of alkylphenol anesthetics in the neuronal tissue of the tadpoles, and (2) to develop a technique called “optoanesthesia” that causes a light-dependent behavioral

phenotype. The results of optoanesthesia experiments are presented in Chapter 6, and in this chapter, I will present experiments on the identification of AziP*m* targets in the tadpole brain.

4.2 AziP*m* Binding to Tadpole VDAC *In Vivo*

In initial experiments, tadpoles were anesthetized with 4 μM [^{3}H]AziP*m*, which is a dose that approximates the EC_{99} for causing tadpole immobility. The tadpoles were then photolabeled *in vivo*, the brains and spinal cords dissected, neuronal membranes isolated, and the protein solubilized for SDS-PAGE. After staining the gel with Coomassie, the entire lane was cut horizontally into 1 mm slices, and then the slices were dissolved in H_2O_2 before scintillation counting (Figure 13). This experiment demonstrated that multiple neuronal protein targets were selectively photolabeled by [^{3}H]AziP*m* *in vivo*.

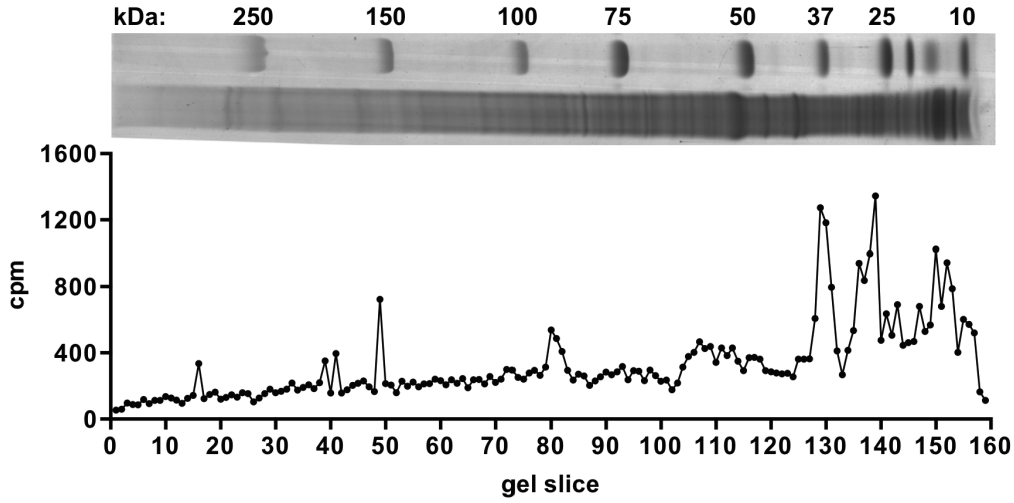

Figure 13. Coomassie-stained SDS-PAGE gel of tadpole neuronal tissue and radioactivity content in each 1 mm gel slice after *in vivo* photolabeling with 4 μM [^{3}H]AziP*m*. For this gel, 70 μg of protein was separated on a 16 cm 4-20% gel poured with a homemade exponential gradient maker (Domingo, 1990).

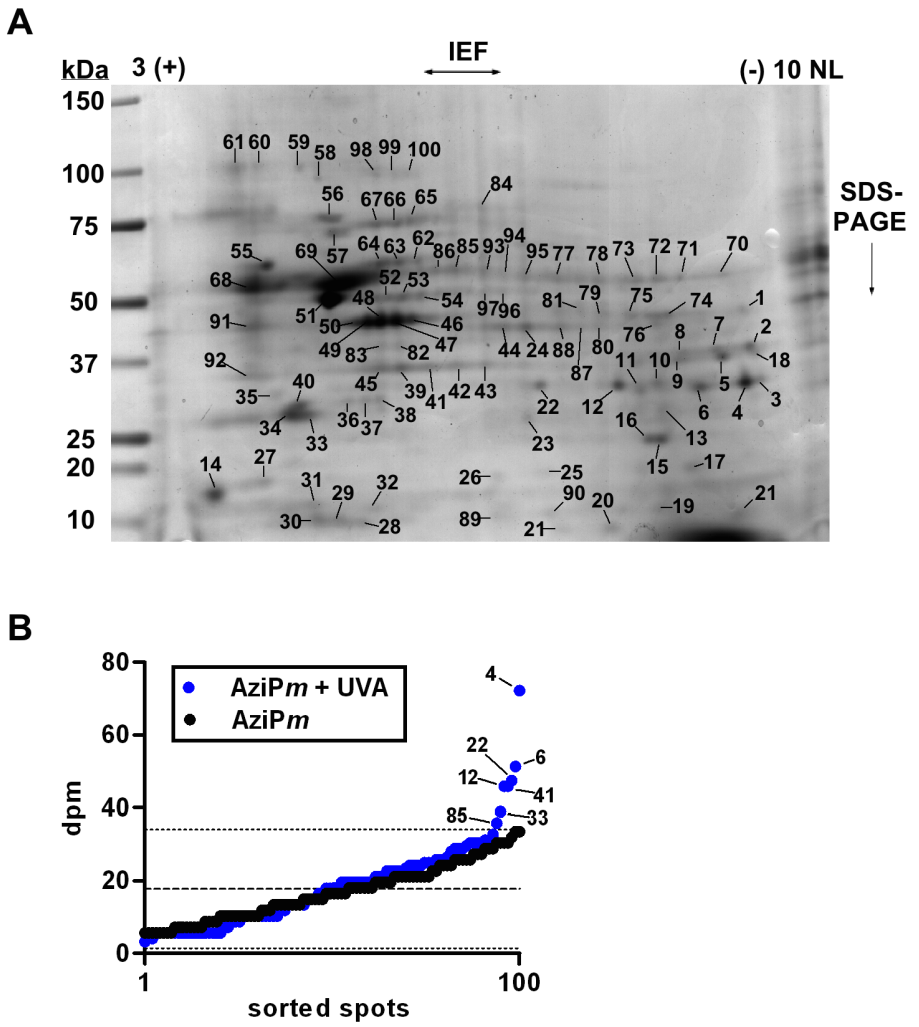

Figure 14. (A) Representative Coomassie stained gel of tadpole neuronal membrane protein. (B) Mean dpm of spots excised from gels of neuronal membrane protein isolated immediately after *in vivo* [^{3}H]AziP*m* ± long-wave ultraviolet light (UVA) treatment. Dpm values were arranged in ascending order, with measurements from select spots indicated. The dashed line indicates background mean from +UVA gels with the dotted line indicating two standard deviations.

To identify individual protein targets of [^{3}H]AziP*m*, protein must be further purified, as each SDS-PAGE band contains many proteins, thereby creating difficulties for the unambiguous identification of the photolabeled protein(s) in each band. Therefore, as an alternative approach, tadpoles were anesthetized and photolabeled *in vivo* as above

and after isolation of neuronal membranes, protein was solubilized for separation with isoelectric focusing (IEF) followed by SDS-PAGE (IEF/SDS-PAGE) (Figure 14A). This experiment was duplicated, and after staining the gels with Coomassie, 100 spots were excised from the gels, dissolved in H_2O_2, and scintillation counted. Mean background radiation in the gel was 18.0 dpm, and the mean radiation content for all 100 spots was 18.8 dpm. Seven spots contained dpm greater than two standard deviations from the background mean (Figure 14B). No protein spots from control tadpoles incubated with [^{3}H]AziP*m* but not exposed to the lamp contained counts that exceeded this background threshold.

In vitro photolabeling of neuronal homogenates with 4 μM [^{3}H]AziP*m* ± 400 μM propofol was performed to investigate the specificity of protein binding. Protein spots identified as photolabeled *in vivo* were analyzed, and all contained dpm above background. Propofol decreased [^{3}H]AziP*m* content in the each spot by 2-75% (n = 3 and n = 2 for each spot (-) and (+) propofol, respectively) (Table 6). Displacement of [^{3}H]AziP*m* binding by propofol suggests conserved binding of the alkylphenols to some saturable protein site(s). A separate gel was run for protein identification. Six spots were unambiguously identified as containing a single protein, while two high confidence identifications were possible in the seventh (Table 6).

Of the identified proteins, published evidence suggested that anesthetic interactions with synaptosomal-associated protein 25 (SNAP-25) might contribute to drug-induced hypnosis. SNAP-25 is a component of the ternary SNARE complex that is involved in vesicular neurotransmitter release, and that binds volatile anesthetics at

physiologically relevant concentrations (Nagele *et al.*, 2005). Isoflurane and propofol inhibit neurotransmitter release through interactions with SNARE complex proteins (Herring *et al.*, 2009, 2011), and mutagenesis in SNARE proteins (including SNAP-25) alters organism sensitivity to general anesthetics (Van Swinderen *et al.*, 1999). Mammalian studies suggest SNAP-25 may be predominantly expressed in excitatory neurons (Verderio *et al.*, 2004; Garbelli *et al.*, 2008), and this protein negatively regulates voltage-gated calcium channels independent of its role in exocytosis (Wiser *et al.*, 1999; Condliffe *et al.*, 2010). Gβ (as part of Gβγ) can also directly inhibit presynaptic voltage-gated calcium channels (Herlitze *et al.*, 1996; Ikeda, 1996) and binds to SNAP-25 and syntaxin to inhibit neuronal exocytosis (Blackmer *et al.*, 2005; Gerachshenko *et al.*, 2005).

Table 6. Analysis of [^{3}H]AziP*m*-photolabed protein from tadpole brain

Spot	% disp[a]	Protein ID	NCBI accession #	Theor[b] MW	Obs[c] MW	Theor[b] pI	Obs[c] pI	% seq coverage	Spectra count
4	40.1	VDAC2	gi|62826006	30183	27937	8.36	8.99	29	18
6	52.0	VDAC2	gi|62826006	30183	27448	8.36	8.27	23	14
12	46.5	VDAC1	gi|28302268	30627	28671	6.85	6.71	20	11
22	74.5	VDAC1	gi|28302268	30627	29160	6.85	6.21	26	16
33	3.4	SNAP25	gi|33416802	23172	26468	4.74	4.89	30	15
41	1.7	$G\beta_4$	gi|49257618	37504	33084	5.70	5.78	20	11
85	26.6	PDIA3	gi|28302197	56086	54992	5.72	5.91	30	25
	26.6	VHA-55	gi|28436920	56411	54992	5.56	5.91	20	21

[a] [^{3}H]AziP*m* displacement by propofol from *in vitro* photolabeling experiments.
[b]Theoretical values were computed with ExPASy Compute pI/Mw tool (http://web.expasy.org/compute_pi/). Monoisotopic molecular weights (Da) are shown.
[c]Observed values were estimated from molecular weight markers and IEF resolving estimations published by the manufacturer of the gels.

The lack of [^{3}H]AziP*m* displacement by propofol on SNAP-25 can be interpreted

in several ways. Although protein binding may be specific to AziP*m* but not propofol, it is more likely that binding sites are not saturable at propofol concentrations that can be achieved in solution. For example, it has been shown that isoflurane and halothane both bind to the SNARE complex in a non-competitive and non-saturable manner (Nagele *et al.*, 2005). This suggests the presence of multiple sites of varying affinities, each capable of binding ligands with low occupancy, in the hydrophobic interior of the SNARE complex.

Of the identified targets, [^{3}H]AziP*m* most selectively bound mitochondrial voltage-dependent anion channels (VDACs), and substantial displacement of photoactive ligand by the parent propofol was most evident with these proteins. VDACs can be post-translationally modified (Kerner *et al.*, 2012), which can alter protein migration during IEF, hence the presence of multiple spots for each isoform. Although VDAC has not been proposed to contribute to anesthetic hypnosis, VDAC isoforms critically regulate a variety of cellular processes related to energetics and apoptosis. Coupled with the fact that every general anesthetic appears to bind VDAC (evidence cited below), further investigation of alkylphenol-VDAC binding was warranted, specifically in the context of VDAC as an off-pathway target of general anesthetics.

4.3 Introduction to VDAC

VDACs are integral membrane proteins in the mitochondrial outer membrane. VDACs are related to ancient porin proteins commonly seen in bacteria, and the functional properties of VDAC proteins are remarkably conserved across eukaryotic species. These channels regulate ion and metabolite passage between the cytosol and the

mitochondrial intermembrane space (Colombini, 1980). Crystallographic and NMR structures of mammalian VDAC revealed a β-barrel with nineteen strands connected by loops, and an N-terminal helix inside the channel (Bayrhuber *et al.*, 2008; Hiller *et al.*, 2008, 2010; Ujwal *et al.*, 2008). The channel remains open under low voltage and has two-fold selectivity for anions relative to cations; however, applied voltages greater than 30-40 mV cause VDAC to change conformations to various "closed" states. VDAC closure (also referred to as "gating") is characterized by a decrease in channel conductance and a reversal in ion selectivity (Colombini *et al.*, 1996).

In addition to voltage, VDAC function is modulated by proteins that include Bcl-xL (Vander Heiden *et al.*, 2001), tBid (Rostovtseva *et al.*, 2004), hexokinase (Azoulay-Zohar *et al.*, 2004), and tubulin (Rostovtseva *et al.*, 2008; Gurnev *et al.*, 2011), and the interactions of these proteins with VDAC critically regulate apoptosis and cellular respiration (Rostovtseva *et al.*, 2005; Rostovtseva and Bezrukov, 2008; Maldonado *et al.*, 2013). Lipids can also affect channel activity by altering the properties of the surrounding membrane (e.g., lipid packing stress), or through direct interactions with the protein (Rostovtseva *et al.*, 2006; Mlayeh *et al.*, 2010). In addition to endogenous regulators, VDAC binds drugs that include erastin (Yagoda *et al.*, 2007) and general anesthetics, although modulators for specific isoforms and/or specific VDAC properties are not available.

4.4 General Anesthetic-VDAC Binding

VDACs are ubiquitous targets of general anesthetics. VDAC isoforms bind halothane (Xi *et al.*, 2004; Pan *et al.*, 2007), neurosteroids (Darbandi-Tonkabon *et al.*,

2003, 2004; Chen, Manion, *et al.*, 2012), long-chain alcohols (Husain *et al.*, 1999; Pratt *et al.*, 2000), alkylphenols (Stewart *et al.*, 2011), and etomidate (Husain *et al.*, 2003, 2006, 2010; Ziebell *et al.*, 2004; Hamouda *et al.*, 2011). Saturable, competitive binding has been demonstrated for all chemotypes, and VDAC has been photolabeled in tissue originating from mammals (including humans), amphibians, insects, and fish. Anesthetic effects on VDAC function had not previously been reported. VDAC and Cys-loop receptors associate *in vitro* (Bureau *et al.*, 1992; Darbandi-Tonkabon *et al.*, 2003, 2004; Gergalova *et al.*, 2012), although the *in vivo* relevance of this is unclear, and knockout of VDAC isoforms 1 and 3 does not affect rodent sensitivity to neurosteroids (Darbandi-Tonkabon *et al.*, 2004). The necessity of VDAC2 for cellular viability has thus far rendered *in vivo* knockout studies of these channels difficult to interpret, as the isoforms compensate for the loss of each other.

4.5 Sites and Functional Consequence of VDAC-Alkylphenol Anesthetic Interactions

To further investigate alkylphenol-VDAC interactions, specifically the binding sites and functional consequences, we transitioned our experiments to mammalian systems. We confirmed alkylphenol anesthetic binding to mammalian VDAC by first enriching and identifying VDAC protein. We purified rat brain mitochondria then separated the protein with IEF/SDS-PAGE. Initially guided by protein molecular weight and isoelectric point, and subsequently confirmed with LC-MS/MS, we identified five spots that contained VDAC as the major component (Figure 15). 64-91% of total spectra per spot were assigned to VDAC (Table 7), and each spot contained multiple isoforms.

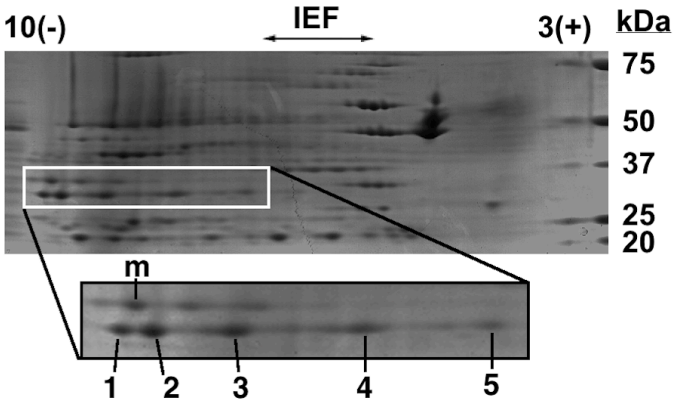

Figure 15. IEF/SDS-PAGE gel of rat brain mitochondria. Spots 1-5 primarily contain VDAC isoforms, and spot "m" contains malate dehydrogenase 2 (MDH-2).

Table 7. Relative protein abundance in rat VDAC spots from IEF/SDS-PAGE

Spot	Isoelectric point[a]	Protein	% of total spectra
1	9.5	VDAC1	48
		VDAC2	10
		VDAC3	6
		MDH-2	36
2	9.3	VDAC1	61
		VDAC2	10
		VDAC3	12
		MDH-2	16
3	8.5	VDAC1	44
		VDAC2	13
		VDAC3	5
		MDH-2	38
4	6.9	VDAC1	54
		VDAC2	27
		VDAC3	5
		MDH-2	13
5	5.9	VDAC1	37
		VDAC2	29
		VDAC3	25
		MDH-2	9
m	9.4	VDAC1	10
		VDAC2	2
		VDAC3	N/A
		MDH-2	88

[a]These experimental values were calculated based on the migration distance of each spot between the two electrodes during IEF, and are based on published recommendations by

the gel manufacturer. We also calculated the theoretical isoelectric points for each protein: 8.63 (VDAC1), 7.44 (VDAC2), 8.91 (VDAC3), and 8.55 (MDH-2). These theoretical values are based on sequence only and exclude post-translational modifications, and these were calculated with the ExPASy Compute pI/Mw tool.

With VDAC identified, we then photolabeled mitochondria with 10 μM [^{3}H]AziP*m* ± 100 μM propofol, again separated the protein with IEF/SDS-PAGE, and dissolved the VDAC gel spots in H_2O_2. Scintillation counting of the VDAC spots after [^{3}H]AziP*m* photolabeling revealed cpm significantly above background (>4 fold each spot), with no selectivity for any spot after normalizing for protein amount. After confirming that [^{3}H]AziP*m* did not bind to the major contaminant in the spots (malate dehydrogenase 2), we determined that 100 μM propofol decreased 10 μM [^{3}H]AziP*m* binding to VDAC by approximately 30%. This is in reasonable agreement with the ~50% displacement of 4 μM [^{3}H]AziP*m* from *X. laevis* VDAC by 400 μM propofol (Table 6).

To identify alkylphenol site(s) on mammalian VDAC, we photolabeled mitochondria with 10 μM (non-radioactive) AziP*m* and sequenced VDAC with LC-MS/MS. Residues photolabeled by AziP*m* were identified by searching VDAC peptides for a 216 Da modification, which corresponds to the mass adduct of photo-reacted AziP*m*. With trypsin digest, we identified Gly56 on VDAC1 as photolabeled in all five spots (Appendix A2.2). To increase sequence coverage, we also digested the most intense spot (spot 2) with chymotrypsin; Val184 on VDAC1 and the homologous residue on VDAC2 (Val196) were identified as photolabeled (Appendix A2.2). Combining trypsin and chymotrypsin digestions, and combining the five spots, we sequenced 95.7% of VDAC1, 51.9% of VDAC2, and 41.3% of VDAC3 (Figure 16). Detection with LC-

MS/MS is dependent on protein abundance in the samples, which contributed to the variability in sequence coverage, as relative spectra counts for VDAC1:VDAC2:VDAC3 were approximately 10:3:1. Relative abundance may have also contributed to the lack of identified adducts on VDAC3 and a site on VDAC2. The photolabeled glycine and valine of VDAC1 are conserved in all three isoforms, which each share ~70% sequence identity, and are believed to adopt identical folds (Komarov *et al.*, 2005; Amodeo *et al.*, 2014; Schredelseker *et al.*, 2014); therefore, alkylphenol binding to these residues on all isoforms remains possible and perhaps likely.

```
rVDAC-1    ---------------------------------MAVPPTYADLGKSARDVFTKGYGFGLIK 28
rVDAC-2    ------------------MAECCVP--VCQRPICIPPPYADLGKAARDIFNKGFGFGLVK 40
rVDAC-3    ---------------------------------MCSTPTYCDLGKAAKDVFNKGYGFGMVK 28
                                             . .*.*.****:*:*:*.**:***::*

rVDAC-1    LDLKTKSENGLEFTSSGSANTETTKVNGSLETKYRWTEYGLTFTEKWNTDNTLGTEITVE 88
rVDAC-2    LDVKTKSCSGVEFSTSGSSNTDTGKVSGTLETKYKWCEYGLTFTEKWNTDNTLGTEIAIE 100
rVDAC-3    IDLKTKSCSGVEFSTSGHAYTDTGKASGNLETKYKVCNYGLIFTQKWNTDNTLGTEISWE 88
           :*:**** .*:**::** : *:* *:.*.*****:  :*** **:************: *

rVDAC-1    DQLARGLKLTFDSSFSPNTGKKNAKIKTGYKREHINLGCDVDFDIAGPSIRGALVLGYEG 148
rVDAC-2    DQICQGLKLTFDTTFSPNTGKKSGKIKSAYKRECINLGCDVDFDFAGPAIHGSAVFGYEG 160
rVDAC-3    NKLAEGLKLTVDTIFVPNTGKKSGKLKASYRRDCFSVGSKVDIDFSGPTIYGWAVLAFEG 148
           :::..*****.*: * ******..*:*:.*:*: :.:*..**:*::**:* *  *:.:**

rVDAC-1    WLAGYQMNFETSKSRVTQSNFAVGYKTDEFQLHTNVNDGTEFGGSIYQKVNKKLETAVNL 208
rVDAC-2    WLAGYQMTFDSAKSKLTRSNFAVGYRTGDFQLHTNVNNGTEFGGSIYQKVCEDFDTSVNL 220
rVDAC-3    WLAGYQMSFDTAKSKLCQNNFALGYKAEDFQLHTHVNDGTEFGGSIYQRVNEKIETSINL 208
           *******.*:::**:: :.***:**:: :*****:**:**********:* :.::*::**

rVDAC-1    AWTAGNSNTRFGIAAKYQVDPDACFSAKVNNSSLIGLGYTQTLKPGIKLTLSALLDGKNV 268
rVDAC-2    AWTSGTNCTRFGIAAKYQLDPTASISAKVNNSSLIGVGYTQTLRPGVKLTLSALVDGKSF 280
rVDAC-3    AWTAGSNNTRFGIAAKYRLDCRTSLSAKVNNASLIGLGYTQSLRPGVKLTLSALVDGKNF 268
           ***:*.. **********::*  :.:******:****:****:*:**:*******:***..

rVDAC-1    NAGGHKLGLGLEFQA-------- 283
rVDAC-2    NAGGHKLGLALELEA-------- 295
rVDAC-3    NAGGHKVGLGFELEA-------- 283
           ******:**.:*:::*


rMDH-2     MLSALARPVGAALRRSFSTSAQNNAKVAVLGASGGIGQPLSLLLKNSPLVSRLTLYDIAH 60
           TPGVAADLSHIETRANVKGYLGPEQLPDCLKGCDVVVIPAGVPRKPGMTRDDLFNTNATI 120
           VATLTAACAQHCPEAMICIISNPVNSTIPITAEVFKKHGVYNPNKIFGVTTLDIVRANTF 180
           VAELKGLDPARVNVPVIGGHAGKTIIPLISQCTPKVDFPQDQLATLTGRIQEAGTEVVKA 240
           KAGAGSATLSMAYAGARFVFSLVDAMNGKEGVIECSFVQSKETECTYFSTPLLLGKKGLE 300
           KNLGIGKITPFEEKMIAEAIPELKASIKKGEDFVKNMK                        338
```

Figure 16. Residues that were sequenced with mass spectrometry are highlighted yellow, and residues that were photolabeled by AziP*m* are bolded in red. Residues highlighted

gray are removed during protein maturation and were not included in sequence coverage calculations. Total protein sequence coverage for each protein is: 95.7% (VDAC1), 51.9% (VDAC2), 41.3% (VDAC3), and 87.6% (MDH-2).

To investigate the locations of the residues that alkylphenols bind, we first used the crystal structure of recombinant rat VDAC1 (PDB code 3EMN) (Ujwal *et al.*, 2008). We oriented this VDAC structure in a hypothetical membrane to calculate the hydrophobic boundaries of the protein (Lomize *et al.*, 2012). Both residues were on the cytosolic half of the protein within the predicted bilayer (Tomasello *et al.*, 2013), with Gly56 and Val184 at the periphery of β-strands 3 and 12, respectively. The backbone α carbons of Gly56 and Val184 were 3.2 Å and 2.3 Å, respectively, from the predicted hydrophobic-hydrophilic interface of the protein (Figure 17). The membrane depths of these residues are consistent with the predicted distribution of propofol in a bilayer, i.e. at the interface of lipid phospho-headgroups and acyl chains (Hansen *et al.*, 2013; Arcario *et al.*, 2014). The topology of an alternatively-folded VDAC1 has also been proposed (Song *et al.*, 1998; Colombini, 2004, 2009), and interestingly, this model also places Gly56 and Val184 at the hydrophobic-hydrophilic interface. However, in contrast to the crystal structure, the residues in this model are placed near the membrane surfaces of opposite leaflets. Regardless, these binding sites should be readily accessible to free ligand dissolved in lipid, assuming that propofol binds the VDAC residues at the lipid-facing channel surface and not inside the pore.

After demonstrating conserved binding of the alkylphenol anesthetics to rat VDAC, we tested whether the clinical compound propofol affects its basic electrophysiological properties. For these experiments, we used native VDAC isolated

from rat liver mitochondria, which also contains a mixture of the three VDAC isoforms. We first measured the conductance of open VDAC reconstituted in a planar bilayer of 1:1 DOPC:DOPE (Figure 18A). The measured single channel conductance of ~4 nS in a bath of 1 M KCl, pH 7.4, is in agreement with previously published values (Colombini *et al.*, 1996). Addition of propofol (1-18 μM) to the bath did not affect open channel conductance, further suggesting that it is unlikely propofol binds inside the open channel lumen (Figures 18A and 18B) (Table 8).

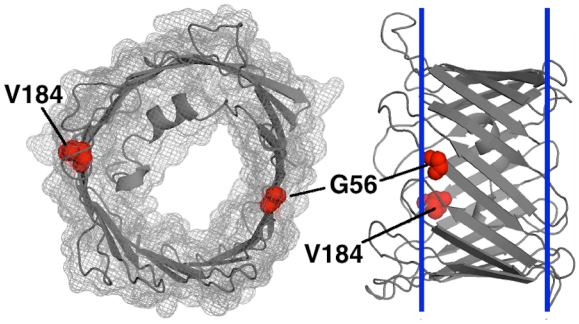

Figure 17. The location of VDAC1 residues Gly56 and Val184, which are photolabeled by AziP*m*, are indicated in red spheres on the crystal structure of recombinant rat VDAC. (*Left*), the protein surface is shown in mesh, and the view through the barrel is from the cytosolic side. (*Right*), the blue lines indicate the predicted hydrophobic-hydrophilic interface of membrane lipids. Here, the cytosolic side is on the left.

We therefore tested whether propofol affects the most characteristic VDAC property, its voltage gating. For these experiments, we used identical lipid and bath conditions as before, but reconstituted multiple channels into the planar membrane and applied a slow symmetrical triangular voltage wave with amplitude ±60 mV (Thomas *et al.*, 1993; Vander Heiden *et al.*, 2000; Rostovtseva *et al.*, 2006; Teijido *et al.*, 2014). At clinically relevant concentrations (1-10 μM), propofol concentration-dependently decreased VDAC conductance at high negative voltages (Figure 19). Because VDAC

inserts unidirectionally into these membranes (Rostovtseva *et al.*, 2006), channel gating at positive and negative voltages can be dissociated.

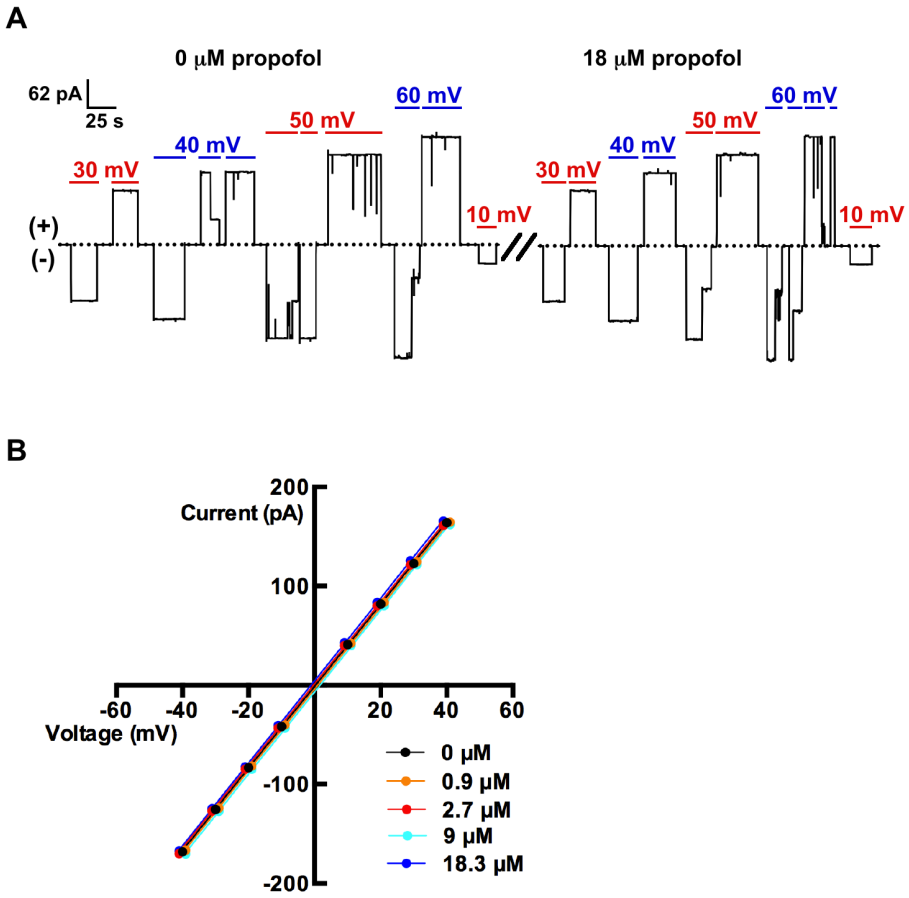

Figure 18. (A) Current trace from a single VDAC channel reconstituted in a planar bilayer. Negative and positive voltages were alternately applied as indicated. Typical VDAC gating was seen, and the open channel conductance in this experiment was 4.1 nS at each voltage ± propofol. (B) Current-voltage relationship for a single VDAC channel in the open state. The same channel was used for the entire experiment, with consecutive additions of propofol.

Table 8. Conductance (nS) per VDAC channel with propofol under low voltage[a]

	Propofol concentration (μM)				
Applied voltage	0	0.9	2.7 ± 0.1	9.0 ± 0.1	18.8 ± 0.5
(-)10 mV	3.8 ± 0.2	3.9 ± 0.3	4.0 ± 0.2	4.0 ± 0.2	3.9 ± 0.3
(+)10 mV	3.8 ± 0.2	3.9 ± 0.3	3.9 ± 0.2	4.0 ± 0.2	3.9 ± 0.2

[a]Mean conductance values from 2-3 experiments are shown with SD.

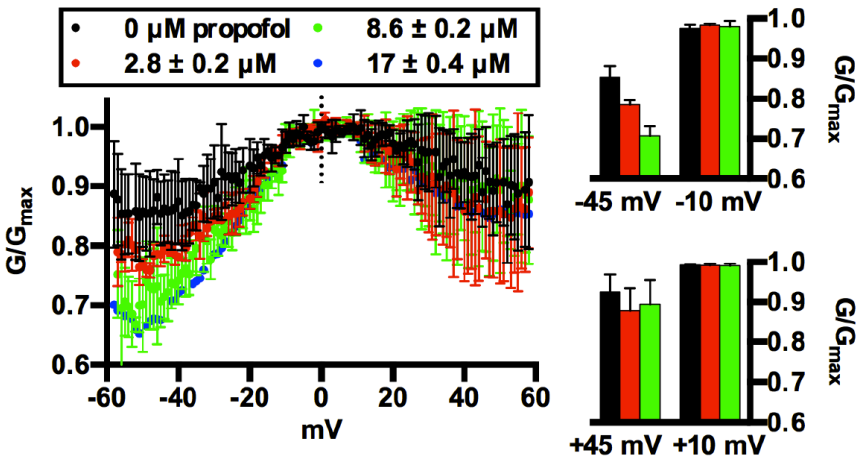

Figure 19. (*Left*), VDAC conductance (G) at each voltage normalized to the maximum conductance for each experiment (G_{max}), which occurs when all channels are open at low voltage. Normalizing by G_{max} accounts for the variable number of channels in the membrane, which ranged between 8 and 22 per experiment. The means ± SD from four (control, 0 µM propofol), three (2.8 µM and 8.6 µM propofol), or two (17 µM propofol) experiments are shown (SD not shown for 17 µM). (*Right*), the mean G/G_{max} ± SE is shown for select voltages. At -45 mV, G/G_{max} decreased by 8% and 17% with 2.8 µM and 8.6 µM propofol, respectively, compared to the control.

After VDAC closure, and in response to decreasing transmembrane voltage, re-opening of channels is fast (sub-milliseconds) (Colombini, 1979), and can be measured as an increase in channel conductance. With a two-state model of VDAC gating, where the channel is either open or closed, the conformational equilibrium of channel re-opening can be quantitatively described by the gating parameters V_0, which is the voltage at which half the channels are open, and *n*, which is the effective gating charge and describes the steepness of the voltage dependence (Thomas *et al.*, 1993; Rostovtseva *et al.*, 2006). At negative voltage, propofol did not significantly affect either gating parameters V_0 or *n* relative to control experiments (Table 9), suggesting that propofol might specifically influence initiation of VDAC gating as opposed to the dynamics associated with channel re-opening.

Table 9. Calculated VDAC gating parameters at negative voltages with propofol[a]

	Propofol concentration		
Gating parameter	0 μM	2.8 ± 0.2 μM	8.6 ± 0.2 μM
V_0	-20.7 ± 1.5 mV	-23.1 ± 2.3 mV	-24.1 ± 3.2 mV
n	2.6 ± 0.4	2.9 ± 0.2	2.9 ± 0.5

[a]Mean values from 3-4 experiments are shown with SD.

As an alternative to enhancing closure rate of VDAC, it is possible that propofol binds within the pore of the channel only when it is closed at negative voltages. VDAC still conducts ions when gated, and therefore channel blockage would further decrease the conductance of these channels. The specificity for voltage polarity could arise considering that the structures of closed VDAC at positive and negative voltages are believed to be different (Rostovtseva *et al.*, 2006). Hence, decreased conductance at high negative voltages could occur through a conformation specific binding site in the lumen that is only present at that polarity.

Interestingly, a similar decrease in VDAC conductance under high voltage of the same (negative) polarity has been previously observed by increasing the mole fraction of non-lamellar lipids in the membrane (Rostovtseva *et al.*, 2006). This initially suggested that propofol might be affecting VDAC by changing the properties of the surrounding membrane. However, in contrast to propofol, membranes of non-lamellar lipids clearly affect channel re-opening, as the voltage at which half the channels open, V_0, decreases while *n* remains constant (Rostovtseva *et al.*, 2006). Non-lamellar lipids likely affect VDAC through increased lipid packing stress on the membrane-embedded channel at the depth of lipid acyl chains. In the proposed model (Rostovtseva *et al.*, 2006), VDAC conformational transitions are sensitive to the pressure in the hydrophobic core of the

lipid bilayer, and upon gating at negative voltages, the external shape of the channel can relieve elevated pressures that derive from that depth in the membrane (Rostovtseva *et al.*, 2006; Rostovtseva and Bezrukov, 2008).

Therefore, to further differentiate the effects of propofol from those of non-lamellar lipids, we performed experiments with gramicidin A, an ion channel with properties known to be modulated by lipid bilayer mechanics. This channel is a sensitive molecular probe of, e.g., lipid packing stress (Lundbaek and Andersen, 1999; Suchyna *et al.*, 2004; Rostovtseva *et al.*, 2006; Weinrich *et al.*, 2009). Gramicidin A forms shorter-lived channels as the fraction of non-lamellar lipid in the membrane increases (Rostovtseva *et al.*, 2006; Weinrich *et al.*, 2009); however, propofol (1-40 μM) did not affect gramicidin A channel lifetime or conductance in DOPC/DOPE membranes (Figure 20).

The absence of a propofol effect on gramicidin A strongly suggests that the general anesthetic acts directly on VDAC through protein binding. The measured effect of propofol is enhanced VDAC closure at negative potentials. The physiological role of VDAC gating itself is a matter of conjecture (Lemasters and Holmuhamedov, 2006), and future work will aim to determine the relevance of enhanced closure. While it is unlikely that VDAC modulation contributes to anesthetic hypnosis (Darbandi-Tonkabon *et al.*, 2004), potentiation of gating could potentially modulate neuronal apoptosis or metabolism (Lemasters and Holmuhamedov, 2006).

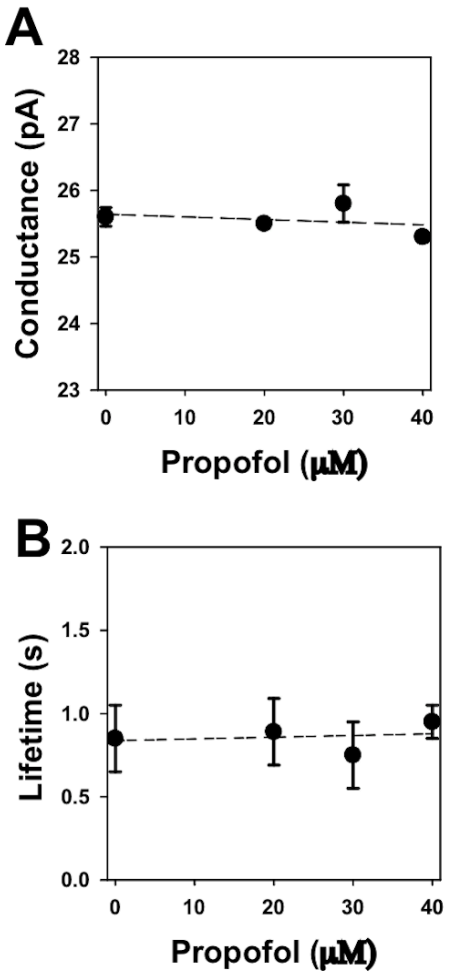

Figure 20. Propofol does not affect the conductance (A) or lifetime (B) of gramicidin A channels. The applied voltage was +100 mV. R^2 for conductance is 0.11, and R^2 for lifetime is 0.04. Data from two separate experiments are combined, and error bars represent standard deviation.

CHAPTER 5: INVESTIGATION OF VDAC-CHOLESTEROL BINDING WITH MOLECULAR DYNAMICS SIMULATIONS

5.1 Experimental Rationale and Introduction to VDAC-Cholesterol Binding

After identifying VDAC residues that were photolabeled by AziP*m*, an extensive literature search was performed to identify whether other ligands, substrates, or metabolites bind to the same sites as the anesthetic. We recognized that, as determined with NMR chemical shift mapping (Hiller *et al.*, 2008), cholesterol binds residues adjacent to the propofol site containing Val184 (Figure 21). We therefore decided to study how the larger, endogenous ligand cholesterol affects the structural dynamics of VDAC before potentially investigating how propofol affects VDAC dynamics through occupancy of the same site.

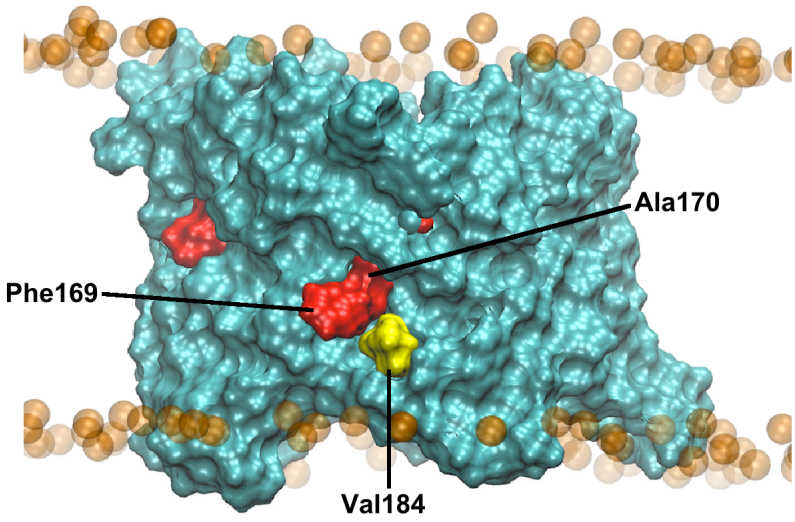

Figure 21. VDAC is shown as the cyan surface topology, and the calculated membrane boundaries (specifically, the phosphorous atoms of membrane lipids) are shown as the transparent orange spheres. The red residues were published to bind cholesterol, and the yellow residue (Val184) binds AziP*m*.

Cholesterol is known to bind mammalian VDAC *in vivo* (de Pinto *et al.*, 1989; Hulce *et al.*, 2013). *In vitro*, cholesterol functions to enhance the structural integrity of isolated VDAC (Pfaller *et al.*, 1985; de Pinto *et al.*, 1989; Popp *et al.*, 1995), and cholesterol promotes uniformity of open channel conductance (de Pinto *et al.*, 1989; Popp *et al.*, 1995). Cholesterol has also been suggested to affect VDAC interactions with other proteins (Pastorino and Hoek, 2008). Together, these effects suggest VDAC function might be modulated when mitochondrial outer membrane cholesterol content increases such as in certain disease states (Rouslin *et al.*, 1982; Baggetto *et al.*, 1992; Montero *et al.*, 2008; Pastorino and Hoek, 2008).

5.2 Cholesterol-Bound VDAC Model

Published NMR chemical shift mapping experiments revealed resonances of nine VDAC backbone amides that had a significant chemical shift induced by the presence of cholesterol, with the structure of the protein essentially unchanged (Figure 22) (Hiller *et al.*, 2008). This indicated a change in the chemical environment surrounding the backbone amides and suggested specific binding by cholesterol. In that experiment, cholesterol was dissolved in a hydrophobic micellar phase and interacted with VDAC from the channel exterior, analogous to membrane cholesterol approaching the protein.

With binding demonstrated experimentally, we aimed to identify the effects of cholesterol site occupancy on VDAC. To initiate this, we began a combined docking and molecular dynamics approach targeting cholesterol to the specific VDAC backbone atoms implicated in binding. The topology of the protein and initial docking calculations suggested a model in which five cholesterol molecules with unique orientations were

required to simultaneously occupy all residues that bind cholesterol. A 5 to 1 mole ratio of cholesterol to protein also reflected conditions under which the chemical shift mapping experiments were performed, and is consistent with the number of cholesterols that bind VDAC in detergent (de Pinto *et al.*, 1989; Hiller *et al.*, 2008). For simplicity, the targeted cholesterol sites are referred to numerically with ascending residue composition (site 1: Lys96, Thr116, Gly117, Asp128; site 2: Phe169, Ala170; site 3: Gly172; site 4: Lys236; site 5: Ser260) (Figure 22).

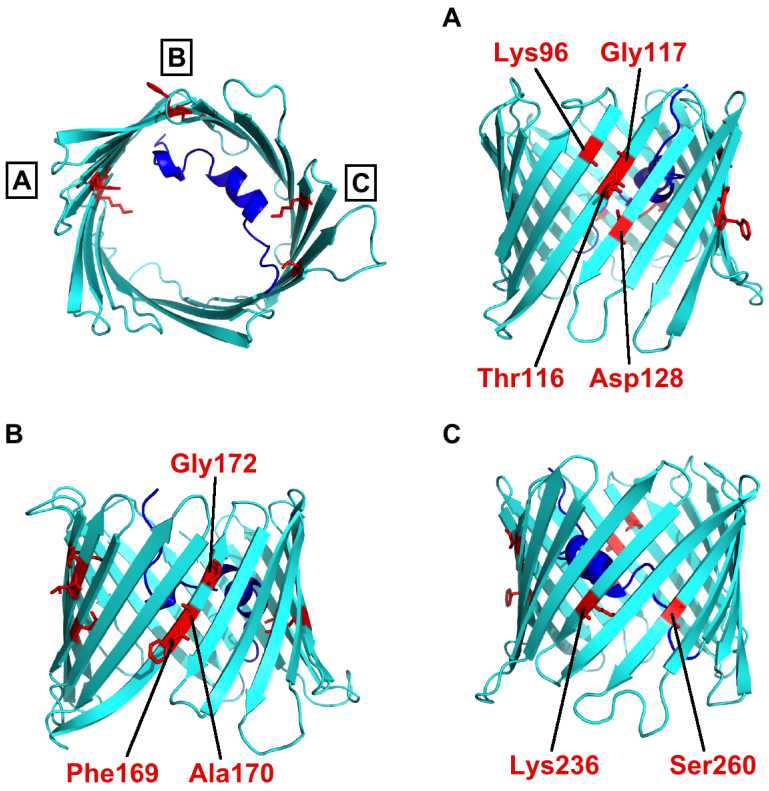

Figure 22. The location and identity of residues experimentally determined to bind cholesterol are shown as red sticks. N-terminal helix residues 2-25 are colored dark blue, and residues 26-283 are colored cyan.

We docked cholesterol to each site using AutoDock, which gave multiple poses and reasonable docking scores for each site ($\Delta G \approx$ -6.0 to -8.3 kcal/mol). With cholesterol

docked, we inserted VDAC into DOPC membranes. Fifteen atomistic molecular dynamics simulations, averaging 37.3 ns each, were computed in an iterative approach. We sampled multiple starting poses in each site with the goal of optimizing a cholesterol-bound VDAC model (Figure 23). The primary criterion for selecting favorable poses was sustained residency of cholesterol in the sites. Unbinding of cholesterol oriented unfavorably, and subsequent diffusion into the membrane, was observable on these timescales.

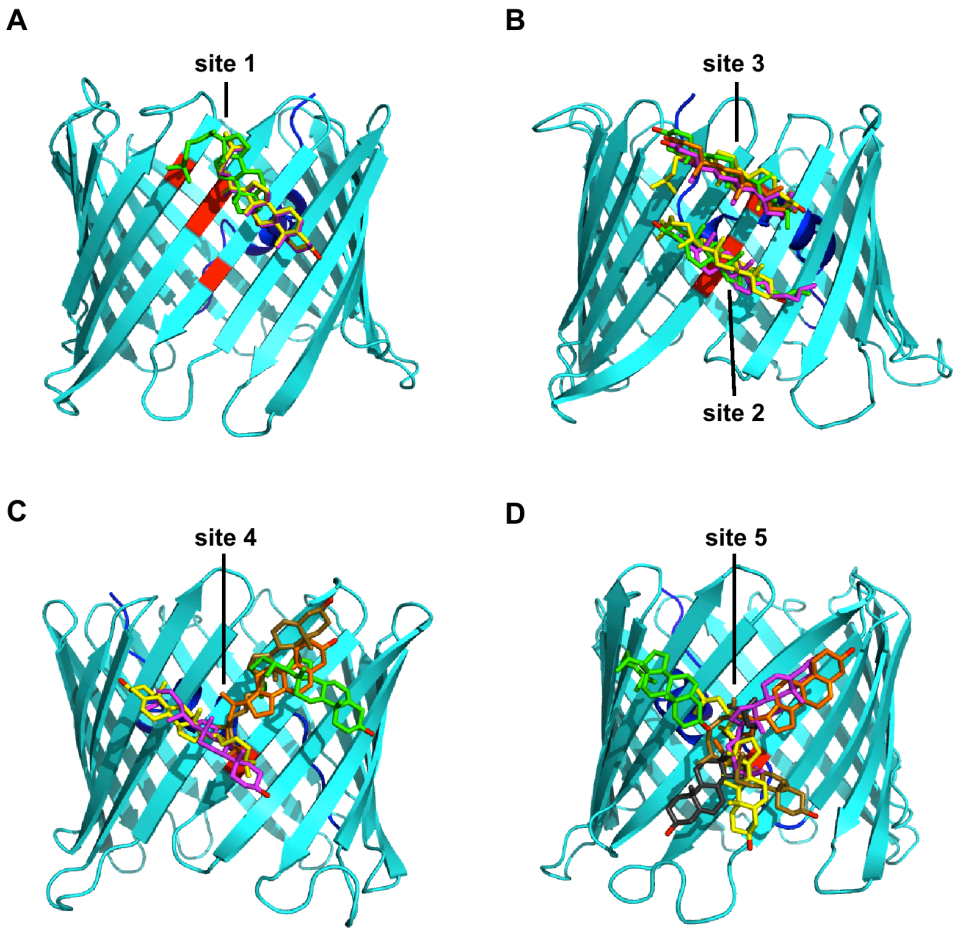

Figure 23. Shown in different colored sticks are the starting orientations for cholesterol during preliminary simulations that were used to build the final cholesterol-bound VDAC model shown in Figure 24. Each starting pose was a docking result that was returned from AutoDock. Residues that comprise each site are colored red.

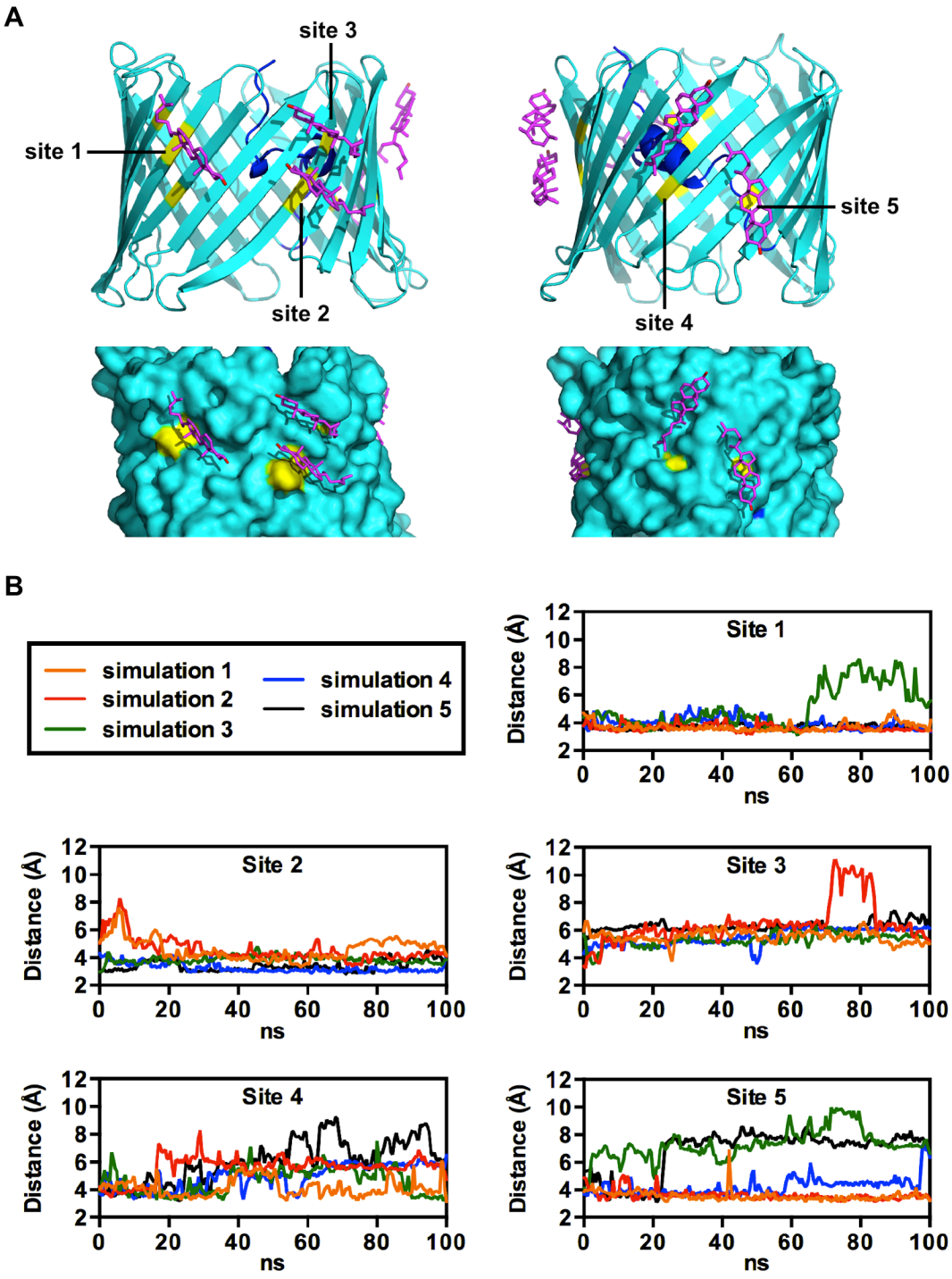

Figure 24. (A) Optimized cholesterol-bound VDAC model, with cholesterol colored magenta. The N-terminal helix is colored dark blue, and the residues within each site are colored yellow. (B) Minimum distance between cholesterol and an amide atom (N or H) of a residue within that site throughout five 100 ns simulations. A running average of 25 data points was used to reduce noise.

The final cholesterol-bound VDAC model used for subsequent production simulations is shown in Figure 24A. The consistency and fidelity of the model were measured in five 100 ns simulations. As a correlate to chemical shift mapping, we measured the distance between cholesterol and the backbone amide atoms in the sites throughout the trajectories (Figure 24B). In each 100 ns simulation, cholesterol maintained a ~3-6 Å intermolecular distance to an amide atom from at least three sites. Additionally, each site was essentially occupied for the full 100 ns in at least three simulations (Figure 24B). The unsustained binding we observed in some simulations, however, suggested low affinity interactions, and simultaneous occupation of these five sites cannot be determined at the NMR timescale at which the sites were initially identified (Hiller *et al.*, 2008).

Multiple intermolecular contacts contributed to stable binding in each site (Table 10). The cholesterol molecules primarily oriented in grooves defined by ridges of hydrophobic and sometimes aromatic side chains that alternately project into the membrane from adjacent β-strands; sites 2 and 3 are defined by a common ridge, as are sites 4 and 5. While we docked cholesterol to the protein *in vacuo*, we anticipated favorable binding in simulations would be enhanced by the sterol hydroxyl forming hydrogen bonds. The hydroxyls of sites 4 and 5 cholesterols extended into the membrane, contacting water and lipid headgroups, and the cholesterol in site 1 formed significant hydrogen bonds with Tyr153. Cholesterol in sites 1 and 3 were also accessible to water funneling from the edge of the protein.

Table 10. Residues that cholesterol contacts in VDAC sites

Site	Side chain contacts	Backbone contacts	H-bond partner(s)[a]
1	Leu95, Leu97, Thr116, Tyr118, Leu125, Cys127, Leu142, Met155	Gly117, Gly126, Gly140, Ala141	Tyr153, H_2O
2	Ile123, Leu142, Leu144, Ala151, Tyr153, Phe169, Val171, Thr182, Val184, Phe190, Trp210	Gly152, Ala170, Asn183, Gly191	N/A
3	Ile123, Leu144, Tyr146, Trp149, Ala151, Val171	Gly145, Leu150, Gly172	H_2O
4	Leu202, Ile221, Ala223, Tyr225, Phe233, Ala235, Val237, Ile243, Leu245	Lys236, Ser234	H_2O, DOPC
5	Phe233, Leu245, Tyr247, Leu259, Ala261, Leu263, Leu275	Gly246, Ser260	Asn269, H_2O, DOPC

[a]Site 1 cholesterol hydrogen bonded with Tyr153 for 40-50 ns in separate simulations, while site 5 cholesterol hydrogen bonded with Asn269 for 12 ns in one simulation.

In contrast to the above, cholesterol bound the protein parallel to the membrane with the hydroxyl among lipid tails in site 2, stably wedged between side chains, and inaccessible to bulk water and lipid headgroups. The initial coordinate of this cholesterol hydroxyl was 1.3 Å from the bilayer midplane. Membrane cholesterol commonly assumes an upright orientation in membranes of saturated phospholipids, with the hydroxyl at the hydrophilic interface ~16 Å from the bilayer midplane (Harroun *et al.*, 2006). However, in the presence of polyunsaturated fatty acids, membrane cholesterol can assume a flat orientation in the middle of the bilayer (Harroun *et al.*, 2006, 2008; Kucerka *et al.*, 2010), not unlike cholesterol in site 2; therefore, cholesterol could assume this orientation and bind protein without initial placement, especially in more complex membranes.

Our initial simulations were designed to identify favorable orientations of cholesterol in the experimentally identified sites. Validating our approach, we observed replacement of a docked cholesterol by a randomly placed membrane cholesterol, which

assumed an identical orientation in site 4. This should theoretically be observed at all sites; however, measuring multiple unbinding and re-binding events at each site is beyond these experimental timescales and comes at an uncertain computational cost. While cholesterol potentially binds in other orientations or sites with physiologically relevant affinities, the present model identifies several binding modes that reasonably and reproducibly satisfy experimental binding data.

5.3 Effects of Cholesterol on VDAC Dynamics

We used the cholesterol-bound VDAC model to investigate the effects of the sterol on the protein. Five 100 ns simulations with an identical mole fraction of cholesterol in the system, but not docked to the protein, were computed (the protein in these simulations is referred to as "apo-VDAC" as opposed to "cholesterol-bound VDAC" using our model). As a reference, the lipid composition of all systems included 9 mole percent cholesterol, comparable to the 8-11 mole percent measured in the mitochondrial outer membrane (Colbeau *et al.*, 1971; Cheng and Kimura, 1983). Cholesterol did not achieve binding poses in apo-VDAC simulations that were equivalent to cholesterol-bound VDAC. Our experimental approach therefore provided comparable systems that dissociated the effects of cholesterol as a ligand, which was investigated here, from its influence on the membrane. Five 100 ns replicates of VDAC with and without bound cholesterol allowed for a measure of reproducibility and biased our sampling towards the intended apo- or cholesterol-bound states.

The protein backbone equilibrated rapidly and remained stable in the presence or absence of bound cholesterol (Figure 25), and the RMSD of backbone α carbons from

averaged structures of apo- or cholesterol-bound VDAC was 0.6 Å. We calculated the average RMSF of the residue α carbons throughout the trajectories (Figure 26A and Figure 26B). With cholesterol-bound, 64 ± 7% of residues per simulation had decreased RMSF compared to the average from apo-VDAC simulations. Residue stabilization by cholesterol was generally global but not absolute, e.g. residues 130-138 (between β-strands 8 and 9) were consistently more dynamic (Figure 26C). For any individual residue, however, the absolute difference in averaged RMSF (i.e., the average RMSF from cholesterol-bound simulations minus that from apo-VDAC simulations) was quantitatively small and between -0.63 Å and +0.55 Å.

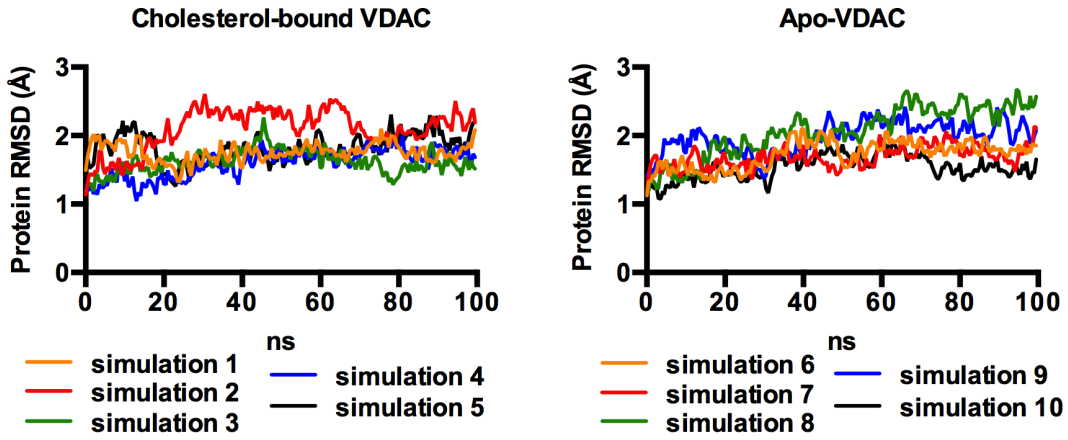

Figure 25. RMSD of cholesterol-bound and apo-VDAC backbone atoms for each of ten simulations, showing the protein is both equilibrated and stable throughout the simulations. The trajectories were aligned to the backbone of the first frames (essentially, the humanized structure of PDB code 3EMN). These traces represent production runs following a short (0.725 ns) equilibration.

Generally, the loops that connect β-strands were most dynamic (Figure 26A and Figure 26B), as previously observed (Villinger *et al.*, 2010; Krammer *et al.*, 2011). In an aqueous environment, these loops lack the structural support provided by the membrane

and inter-residue electrostatic interactions. Even without direct cholesterol binding, the dynamics of the loops were most susceptible to change. The ability of distant loops to be affected by changes in global protein dynamics has been well characterized in soluble proteins (Kurkcuoglu *et al.*, 2012; Zimmermann and Jernigan, 2012; Wood *et al.*, 2013). Here, VDAC residues that bind cholesterol might form networks with adjacent amino acids that relay the presence of cholesterol to the loops. Across these loops, the largest percent increases in averaged RMSF were seen in residues Ala134 and Lys274, and the largest percent decreases were seen in residues Pro105, Gly187, and Asn269 (Figure 26D).

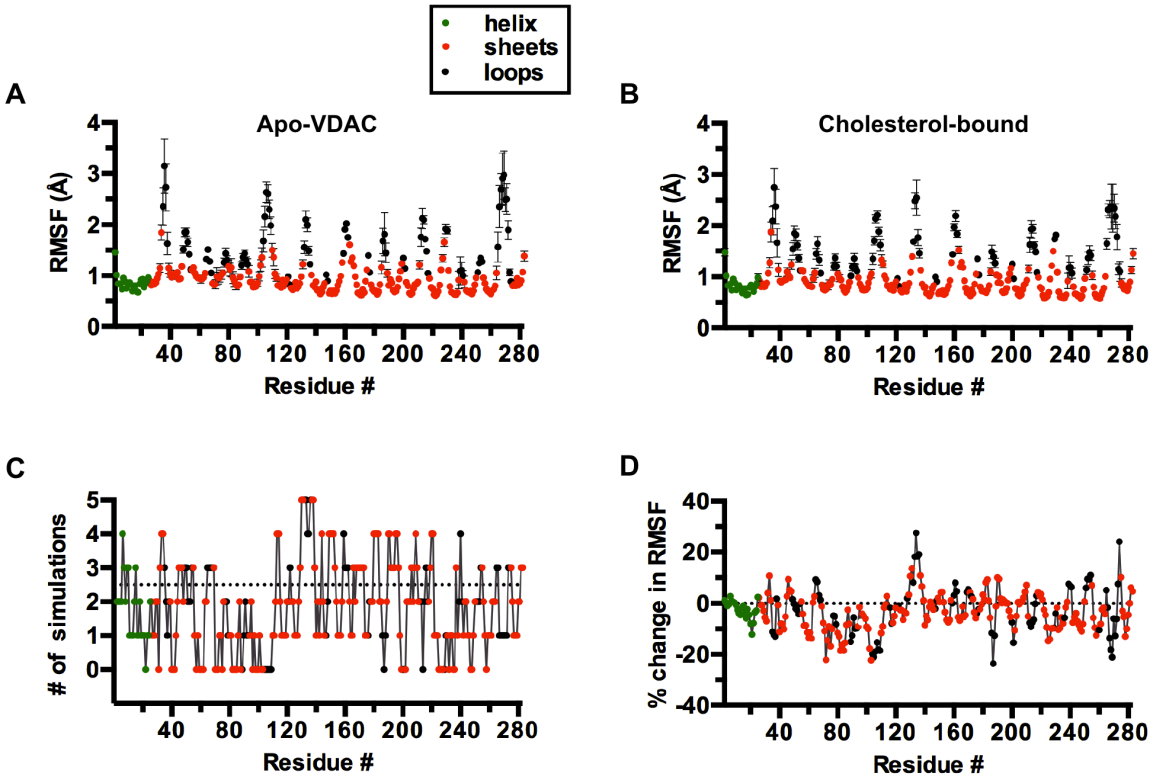

Figure 26. (A) The average RMSF value for each residue from five simulations of apo-VDAC and (B) cholesterol-bound VDAC systems. When not visible, the error was smaller than the size of the point. (C) The number of simulations (out of 5) that each residue from cholesterol-bound VDAC simulations had increased α carbon RMSF

relative to the average from apo-VDAC simulations. (D) Percent change in RMSF averaged across five cholesterol-bound and five apo-VDAC simulations. Points below the dotted lines indicate that the residue was less dynamic in cholesterol-bound VDAC simulations relative to apo-VDAC simulations.

We investigated further the effects of cholesterol on the N-terminus, as the helix and cholesterol bind the same wall of the β-barrel, but inside and outside of the pore, respectively (Figure 22). Bonding pairs between helix residues 2-25 and the barrel wall were variable both within and between the two groups (with or without bound cholesterol) (Table 11), and this variability extended to residues that hydrogen bond in the crystal structure (Ujwal *et al.*, 2008). However, the helix maintained 3.1 ± 0.1 and 2.9 ± 0.1 hydrogen bonds per frame with the barrel wall throughout apo-VDAC and cholesterol-bound VDAC simulations, suggesting a dynamic network maintained helical stability. Separate from hydrogen bonding, channel stability is also both dependent on and indicated by a hydrophobic contact between helix residue Leu10 and barrel residue Val143 (Schneider *et al.*, 2010; Zachariae *et al.*, 2012). The average distance (~3 Å) and maximum distance (~5 Å) between these residues throughout simulations were further consistent with a constitutively open channel for both apo- and cholesterol-bound VDAC. Interestingly, we detected a cholesterol-induced increase in the average minimum channel radius from 5.5 ± 0.1 Å (apo-VDAC) to 5.8 ± 0.1 Å (cholesterol-bound VDAC) using an algorithm that fits spheres inside the channel along the z axis (comparison of minimum channel radii: $p < 0.05$, two-tailed t-test, $n = 5$ simulations each group) (Smart *et al.*, 1993). The increased channel radius with cholesterol bound does not necessarily

imply greater area for water and ion accessibility; however, it does suggest larger circular or less elliptical constriction sites.

Table 11. Percent of simulation frames in which VDAC residue pairs hydrogen bond[a]

Simulation	A2-H122	P4-N124	F18-K236	G25-T49	G25-L275	G23-S260	K20-K224	G23-L26	Y7-N168	V3-K119
1	56.3	49.8	44.8	52.5	7.1	30.4	0.0	9.1	0.0	0.0
2	53.1	43.6	43.4	7.5	29.4	27.2	51.5	5.8	0.0	0.0
3	52.9	50.3	38.8	15.9	3.8	20.4	59.9	11.2	0.0	0.0
4	43.6	50.7	44.9	44.2	42.6	29.9	3.3	9.5	0.0	0.0
5	57.5	46.8	46.8	42.5	37.8	29.2	3.0	7.3	0.0	0.0
6	52.1	50.3	43.4	41.1	37.7	23.7	47.9	8.9	0.1	0.0
7	50.1	46.8	50.2	20.6	46.8	34.7	0.4	7.0	0.0	0.0
8	37.1	52.1	34.9	67.8	19.2	23.5	30.9	9.0	0.1	0.0
9	54.7	50.5	46.2	40.3	40.4	32.5	2.3	6.1	11.8	0.0
10	52.9	41.1	48.9	33.0	35.2	35.7	34.7	8.7	0.6	0.0
Median	52.9	50.0	44.8	40.7	36.4	29.5	17.1	8.8	0.0	0.0

[a]These pairs are specific to the N-terminal helix (residues 2-25) hydrogen bonding with the remainder of the protein (residues 26-283), and include polar atoms from side chains and the protein backbone. These have >10% occupancy in at least one simulation. Red indicates >10% difference from the median for that specific pair, and blue indicates >25% difference. The crystal structure from PDB code 3EMN contains hydrogen bonds between P4-N124, G25-T49, G25-L275, G23-S260, and V3-K119.

5.4 Effects of Cholesterol on Open VDAC Ion Permeability

We generated averaged electrostatic potential maps from the simulations, which revealed entirely positive net potentials inside the anion channel. Cholesterol-induced protein rigidity resulted in larger regions of strong positive potential, with the strongest potentials in the channel arising from residues with decreased positional fluctuation in cholesterol-bound VDAC (Figure 27). Mutagenesis of multiple residues in these positions modulates ion permeability under low voltage *in silico* (Lee *et al.*, 2011; Krammer *et al.*, 2013) and *in vitro* (Blachly-Dyson *et al.*, 1990). Similarly, negatively

charged residues that were also stabilized by cholesterol are located along the barrel wall opposite the N-terminal helix, providing a path for K^+ ions through cholesterol-bound VDAC. This was seen adjacent to Glu84 (Figure 28), previously shown to influence K^+ permeability through VDAC *in silico* (Krammer *et al.*, 2011; Rui *et al.*, 2011).

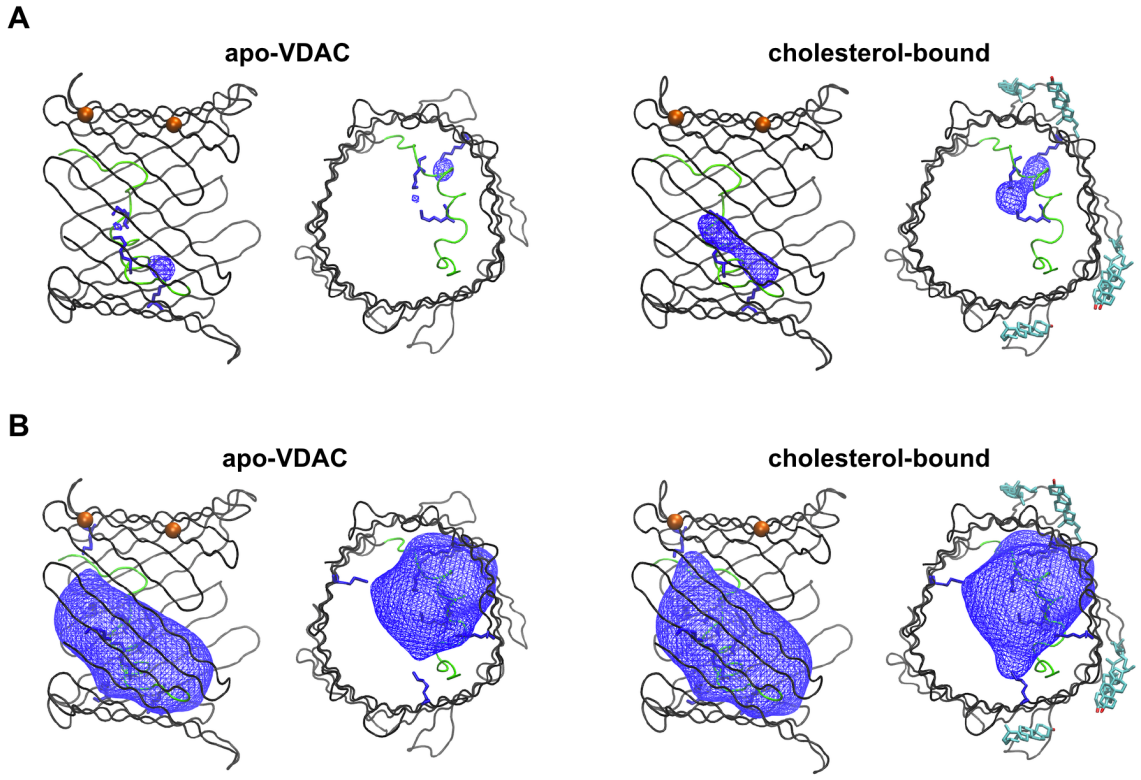

Figure 27. Electrostatic potential maps showing positive potential inside apo-VDAC and cholesterol-bound VDAC. Blue electrostatic potential maps correspond to (A) +64 kT/e and (B) +38 kT/e. The N-terminal helix is colored green, and the protein backbones correspond to the averaged α carbon structures from the simulations with or without bound cholesterol. The N- and C-termini are at the left entrance (in lateral structures) or on the near side of the channel (when looking into the barrel). In lateral structures, the orange spheres correspond to the α carbons of Leu69 and Ser101 which, for reference, are located at approximately $z \approx -8$ and $z \approx 8$, respectively. In (A), Lys12, Lys20, and Lys236 are shown in blue sticks, and are the charged residues that predominantly contribute to the electrostatic field. Arg15, Lys32, Lys119, Lys174, and Lys224 are also shown in (B). All of the mentioned residues are stabilized by cholesterol (i.e., have a decreased average RMSF).

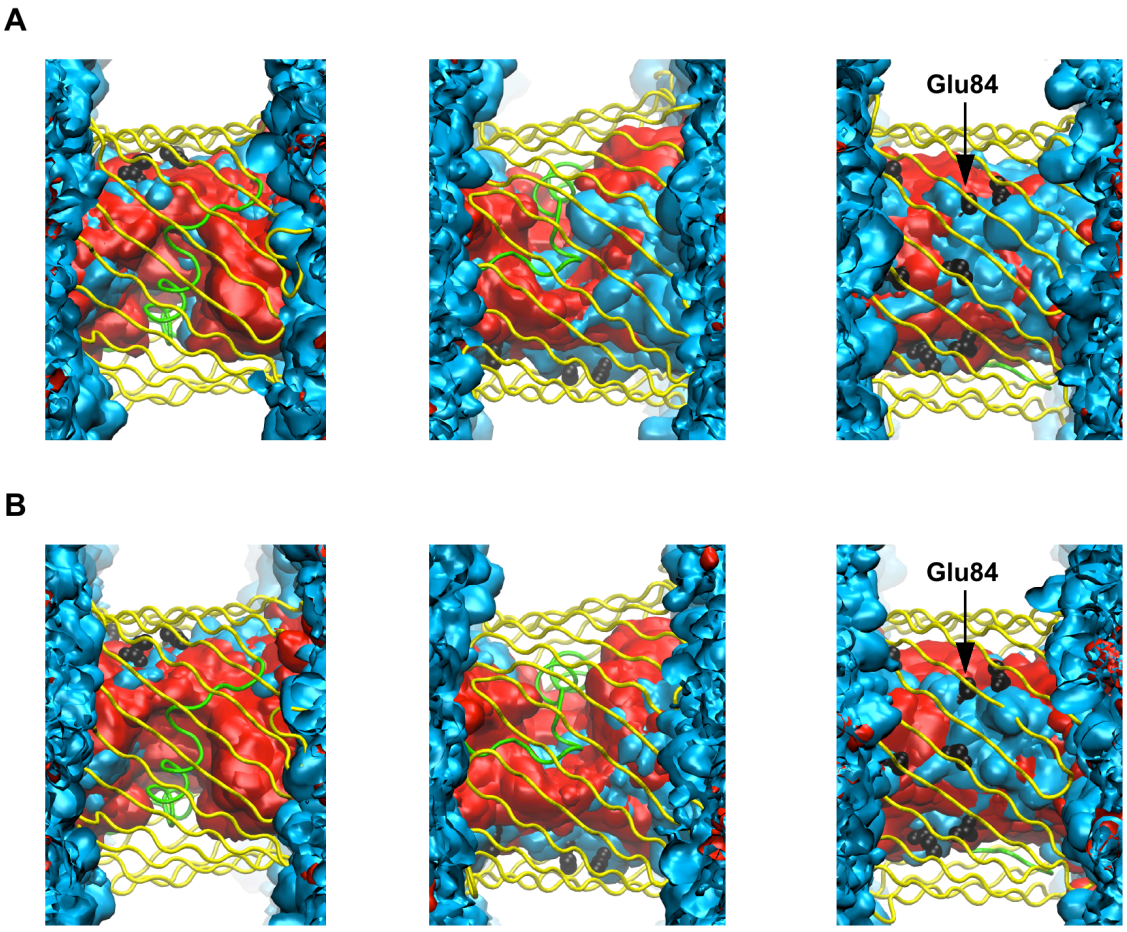

Figure 28. K^+ ions concentrate around negatively charged residues inside the channel on the opposite side of the barrel from the N-terminal helix. The cyan and red correspond to the aggregate volumetric densities of K^+ and Cl^- ions, respectively, at $3*10^{-5}$ amu/Å^3. (A) Apo-VDAC and (B) cholesterol-bound VDAC are shown, with the *trans* pore entrance to the left, and the panels representing a 360˚ rotation around the channel viewed from the within the membrane. Shown in black spheres are the sidechain atoms of Asp30, Glu40, Glu59, Glu84, Glu88, Asp100, and Glu280, all of which have decreased average RMSF in cholesterol-bound VDAC. Note the confluence of K^+ density across the entire channel (from left to right) and surrounding the negatively charged residues, particularly adjacent Glu84, in cholesterol-bound VDAC. In contrast, Cl^- density is concentrated around the N-terminal helix (colored green); this is increasingly evident in cholesterol-bound VDAC compared to apo-VDAC.

Despite changes in charge distribution, there was no significant change in the average number of Cl^- or K^+ ions that diffused through the channel in each simulation

(number of ions that translocate per simulation: Cl^-: 26 ± 3 (cholesterol-bound) and 23 ± 1 (apo-VDAC); K^+: 10 ± 2 (cholesterol-bound) and 7 ± 1 (apo-VDAC)). The Cl^-/K^+ permeability ratios from apo- and cholesterol-bound VDAC were 3.3 ± 0.4 and 2.8 ± 0.7, in reasonable agreement with the experimental value of ~2 for the open channel (Colombini *et al.*, 1996). We estimated the potential of mean force for Cl^- and K^+ as a function of the ion height z in the channel (Figure 29). Free energy wells for Cl^- were observed inside the channel on either side of the N-terminal helix, which is the source of the strongest positive potentials (Figure 27). The free energy well at -10 Å < z < -2.5 Å coincided with the location of the minimum pore radius, which was also the location of the free energy maxima for K^+. The averaged magnitude and shape of the K^+ profiles are similar to previous computational work despite variability between simulations at 0 Å < z < 10 Å, possibly due to under-sampling of K^+ inside the anion channel (Krammer *et al.*, 2011, 2013).

5.5 Conclusions, Cholesterol Binding to VDAC

Cholesterol can stably bind and modestly alter the dynamics of open mitochondrial VDAC; however, ion diffusion through the channel was unaffected by cholesterol. This is not surprising because, similar to propofol, cholesterol binds open VDAC from the lipid-exposed channel surface and does not interact with the channel lumen. Only a conformational change that modifies the structure of the channel lumen should be sufficient to modulate ion permeability; however, this would then correspond to a closed channel.

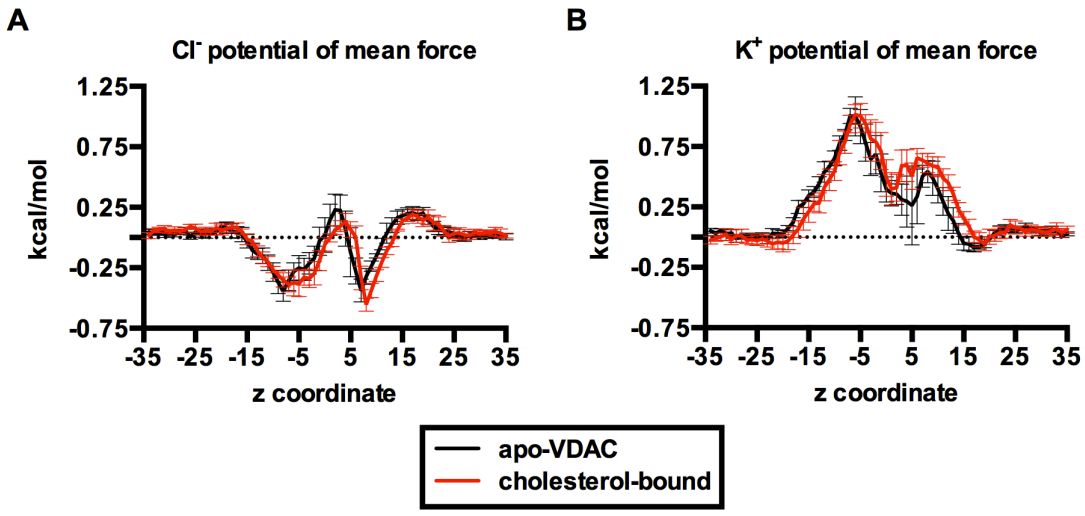

Figure 29. Potential of mean force for (A) Cl^- ions and (B) K^+ ions along the z axis, with and without bound cholesterol.

Although we observed replicable cholesterol binding, it is unclear from our simulations whether the five investigated sites would be simultaneously occupied *in vivo*. Computationally, in addition to modifying the starting positions of molecules, the stoichiometry of site occupancy can be modulated by the replacement rate of vacated sites by cholesterol from the membrane, which in turn is affected by membrane content. Mitochondrial outer membrane cholesterol content varies in disease states to potentially modulate VDAC function, with 2-10 fold increases in cholesterol per mg of protein observed (Rouslin *et al.*, 1982; Baggetto *et al.*, 1992; Montero *et al.*, 2008), suggesting higher site occupancy under these conditions. However, varying membrane cholesterol content might also affect VDAC through membrane-mediated mechanisms in addition to direct effects of specific protein binding, which was investigated here. Regulation of membrane protein function by lipid composition can likely occur by exerting the physical properties of the membrane and its components through specific protein sites.

Although we observed modest effects of cholesterol on the open channel, our model will be particularly useful in experiments that investigate how cholesterol affects VDAC function under applied electrochemical forces. We did not investigate the effects of cholesterol on closed VDAC either computationally or electrophysiologically. Because cholesterol and propofol bind to at least one conserved site, and because cholesterol affects gramicidin A properties similar to lipids that enhance VDAC closure (Weinrich *et al.*, 2009), it is reasonable to hypothesize that cholesterol would also promote VDAC closure at high voltages. It is therefore possible that cholesterol and propofol would additively affect VDAC gating, or alternatively, cholesterol could mitigate the effects of propofol by displacing the ligand from critical sites or through currently undefined membrane-mediated mechanisms.

CHAPTER 6: OPTOANESTHESIA

6.1 Optoanesthesia in *X. laevis* Tadpoles

With the exception of demonstrating anesthetic efficacy in tadpoles and rodents, general anesthetic photolabels have not been utilized in *in vivo* studies. *Ex vivo* photolabeling of $GABA_A$ receptors with azi-etomidate demonstrated that covalent attachment of ligand to binding sites can irreversibly modulate the ion channel (Zhong *et al.*, 2008). This included potentiation of GABA currents after washout of unattached compound, as well as increased receptor sensitivity to direct activation by etomidate and propofol (Zhong *et al.*, 2008). We therefore hypothesized that *in vivo* photolabeling of tadpoles equilibrated with AziP*m* would prolong the immobility endpoint of anesthesia, as anesthetic sites on relevant targets, likely including the $GABA_A$ receptor, become irreversibly occupied.

Albino tadpoles anesthetized with 3 μM propofol or 4 μM AziP*m* (approximate EC_{99} doses) recovered on similar time scales following transfer to fresh pond water (Figure 30A, *left*); recovery under these conditions is largely a function of drug diffusion back into the water. In contrast, albino tadpoles immobilized with AziP*m* and exposed to long-wave ultraviolet light (UVA) before transfer to fresh water exhibited prolonged immobility that was not observed when tadpoles were treated with UVA after being anesthetized with propofol, which lacks a photoactive moiety (Figure 30A, *right*). A relationship between lamp exposure time and recovery time was also evident, suggesting progressive covalent occupancy of AziP*m* in functionally relevant sites. Premature death or differences in body mass were not observed between tadpoles treated with either

alkylphenol anesthetic ± UVA following emergence (measured up to ten days).

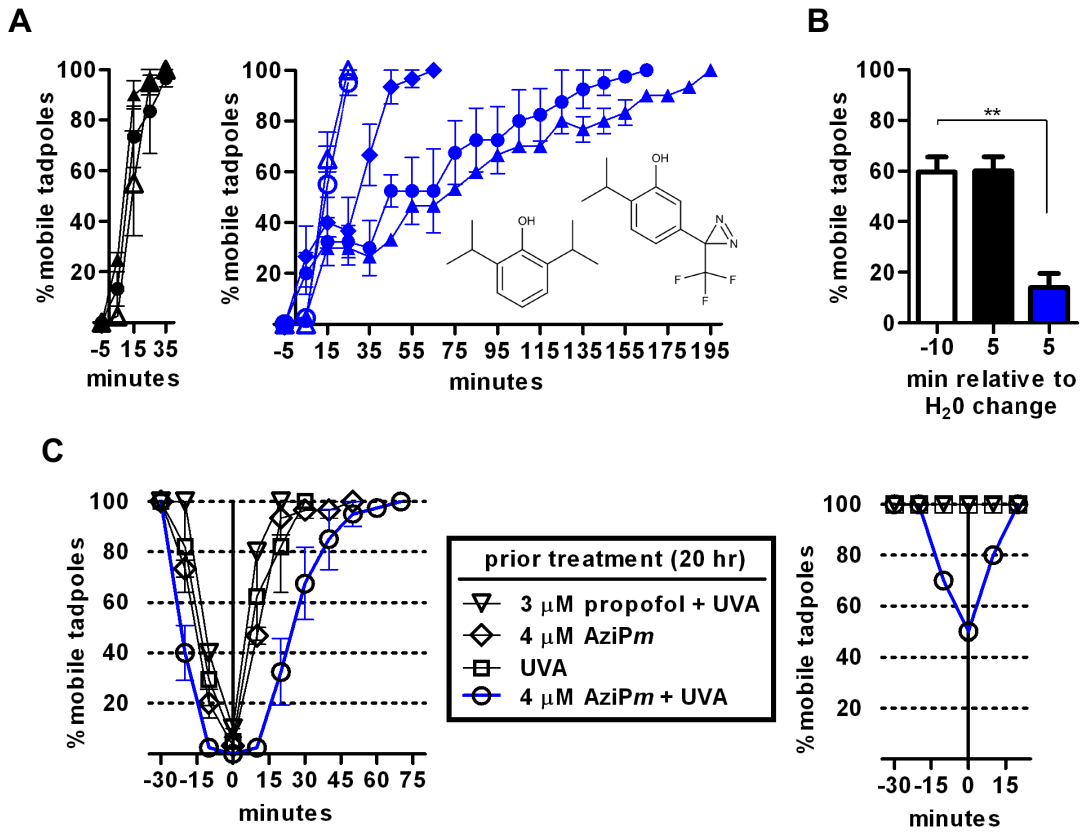

Figure 30. (A) Time course of recovery for tadpoles following anesthetic equilibration and (*left, black*) sham treatment or (*right, blue*) UVA exposure. 3 μM propofol (open symbols) or 4 μM AziP*m* (closed symbols) was used. Treatment times were 3 minutes (diamonds), 10 minutes (circles), or 20 minutes (triangles), and the water was changed at time 0. Data shown is from 3-4 experiments per group. (B) *In vivo* photolabeling for 10 minutes after equilibration with a sub-EC_{99} dose of 3 μM AziP*m* increased the immobile fraction of tadpoles. The water was changed at time 0, with photolabeling from -10 to 0 minutes. A one-way ANOVA found a significant difference between the three means ($p < 0.01$), and Bonferroni's post-hoc found a significant decrease in the percent of mobile tadpoles after lamp exposure and water change (blue bar, $p < 0.01$). Data is from three experiments per treatment (± UVA). After equilibration, the tadpoles were randomly assigned to sham or UVA treatment, with the data at -10 minutes representing both groups, and sham-treated animals represented by the black bar. (C) Induction and recovery of tadpoles treated with (*left*) 2 μM propofol or (*right*) 0.8 μM propofol 20 hours after the indicated treatments.

Covalent adduction should concentrate ligand into protein sites by decreasing off-rates, thereby increasing the apparent potency of the molecule. *In vivo* photolabeling for ten minutes after equilibration with a sub-EC_{99} AziP*m* dose markedly increased the population of immobilized tadpoles (Figure 30B). Further, we hypothesized that retained attachment of AziP*m* in functionally relevant targets after washout and emergence would manifest as a decrease in the effective concentration of propofol for immobility. Thus, 20 hours after emergence, tadpoles treated as above were exposed to 2 μM or 0.8 μM propofol. Animals photolabeled *in vivo* displayed increased sensitivity (more rapid induction, slower emergence, and induction with a lower dose) relative to controls (Figure 30C).

Lastly, 4 μM AziP*m* in pond water was photolysed for a period corresponding to twice the diazirine half-life (i.e., to a final concentration of ~1 μM plus whatever the product(s) of photolysis are). Tadpoles were then placed in this solution, and after 30 minutes, immobility was not observed, ruling out the possibility that a caged anesthetic that is more potent than AziP*m* and/or has slower washout kinetics was created with UVA. Together, these data suggest prolonged anesthetic influence due to photoadduction of ligand *in vivo*, and interestingly, *in vivo* mechanisms for terminating covalent drug action exist.

6.2 *In Vivo* Covalent Attachment of [^{3}H]AziP*m* to Proteins Over Time

The *in vivo* photolabeling technique that prolonged the behavioral phenotype caused by the anesthetic is called “optoanesthesia”. Because general anesthetics are

assumed to exert their effects through CNS targets, we measured retention of photoactivated AziP*m* in neural tissue following optoanesthesia. Brains and spinal cords from control tadpoles and those photolabeled *in vivo* with [^{3}H]AziP*m* were isolated to

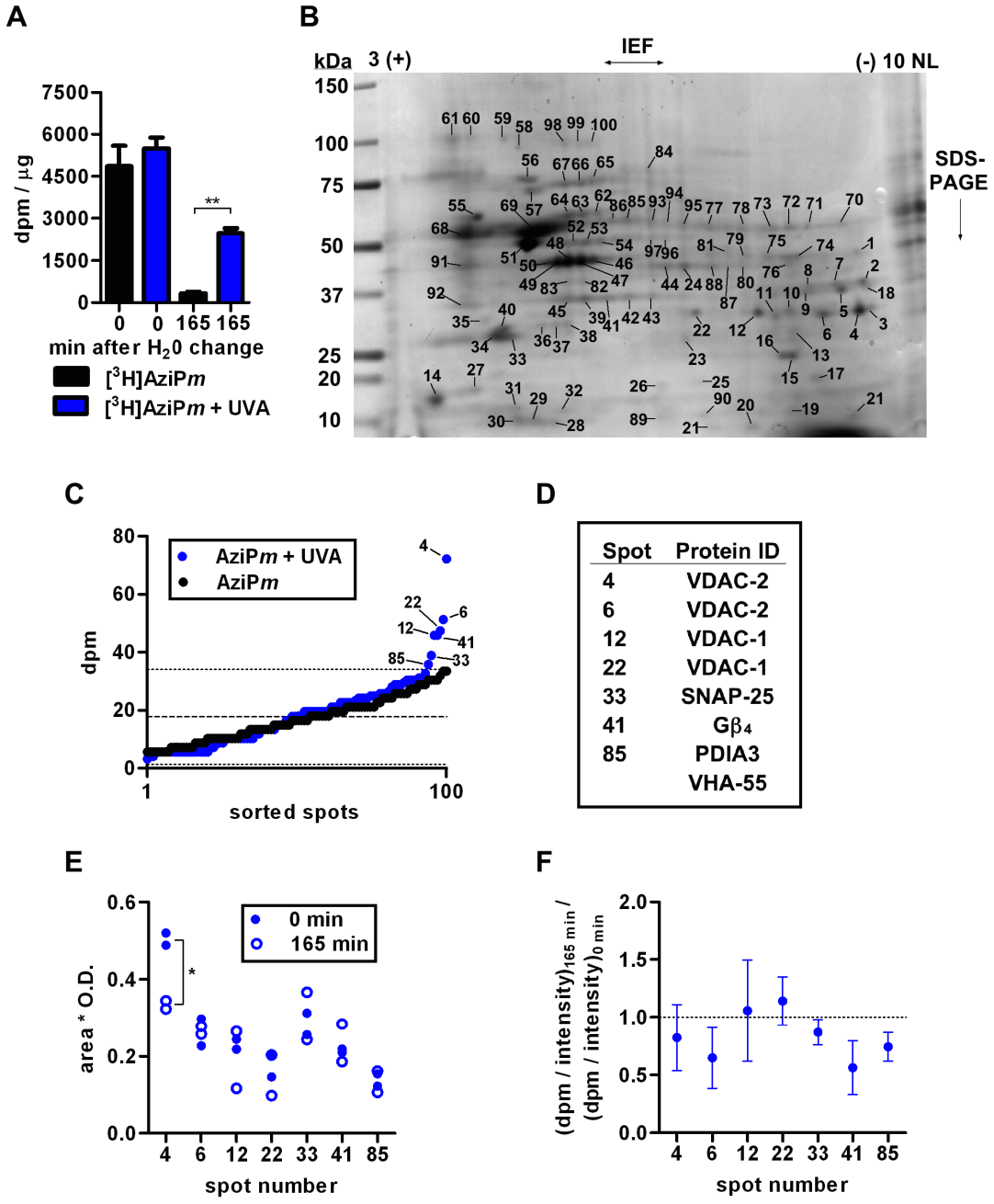

Figure 31. (A) Quantification of dpm normalized to protein amount in CNS tissue of tadpoles treated with AziP*m* ± UVA for ten minutes. Data is from 3 experiments per

treatment (10 tadpoles per experiment). Data was analyzed by one-way ANOVA with Bonferroni's post-hoc comparing dpm within each time point ($p < 0.01$). (B) Representative Coomassie-stained gel of tadpole neuronal membrane protein. (C) Mean dpm of spots excised from gels of tissue isolated immediately after *in vivo* [^{3}H]AziP*m* ± UVA treatment. Dpm values were arranged in ascending order, with measurements from select spots indicated. The dashed line indicates background mean from + UVA gels with the dotted line indicating two standard deviations. (D) Identities of proteins in the indicated spots. A detailed analysis can be found in Table 6. (E) Coomassie stain intensity quantified from *in vivo* gel spots. Spot 4 was found to decrease with a two-tailed student t-test ($p < 0.05$). (F) The ratio $(\text{dpm/intensity})_{165\ \text{min}}$ divided by $(\text{dpm/intensity})_{0\ \text{min}}$ shows the change in the fraction of photolabeled protein over the emergence period. Standard deviation is shown, and a ratio of 1 would indicate no change.

quantify radioactivity after recovery in fresh water (Figure 31A). Following [^{3}H]AziP*m* induction, without washout, no difference was seen between groups treated ± UVA. However, approximately eight-fold more radioactivity was measured in the neuronal tissue of photolabeled animals at 165 minutes, the point of emergence for all tadpoles exposed to 4 μM AziP*m* and 10 minutes of UVA.

The optoanesthesia-induced prolongation of tadpole immobility indicated that neuronal substrates photolabeled *in vivo* were relevant targets of AziP*m* and possibly propofol. To identify specific proteins photolabeled *in vivo*, neuronal membrane protein from tadpoles equilibrated with [^{3}H]AziP*m* and photolabeled for 10 minutes was subjected to IEF/SDS-PAGE. Duplicate gels were stained, and one hundred random spots were excised for scintillation counting (Figure 31B). (Note that this experiment was first described in Chapter 4, and Figures 31B and 31C are also shown in Figure 14.) Seven spots contained dpm greater than background, and covalent attachment of [^{3}H]AziP*m* was dependent on lamp exposure. The analysis of protein in the spots can be found in Table 6, and the identities of the spots are repeated in Figure 31D.

We coupled this behavioral phenotype with time-resolved gel proteomics. The temporal aspects were designed to specifically identify critical facilitators of the general anesthetic state. We hypothesized that for tadpoles to emerge, the cellular components contributing to mobility must adapt by degrading photolabeled proteins whose activity is altered, and/or by replacing these photolabeled macromolecules with newly synthesized proteins. An alternative hypothesis, not tested here, is that the activities of proteins that are not targets of AziP*m* are altered to compensate for the covalent modification of the alkylphenol binding partners. To test the former hypothesis, neuronal membranes were isolated 165 minutes after tadpoles were photolabeled (when all had emerged) as above for IEF/SDS-PAGE, and the previously identified spots from duplicate gels were assayed for dpm. The mean from three spots contained dpm within 10% of the initial value, while decreases of 46%, 35%, 42%, and 28% were noted in spots 4, 6, 41, and 85 respectively. Coomassie intensity was quantified to assess changes in protein expression, and with the exception of spot 4, little variation was observed (Figure 31E).

Spot dpm was normalized to corresponding Coomassie intensities for these *in vivo* experiments. We proposed that proteins with decreased radioactivity content coincident with emergence gained additional credibility as functionally important. Thus, we calculated the ratio of normalized photolabel incorporation at 165 minutes to that at the 0 time point for each spot (Figure 31F). A ratio of 1 would indicate that the fraction of adducted protein did not change over the 165 minutes. We found that the ratio from spots 6, 33, 41, and 85 were less than 1, suggesting potential relevance in emergence from optoanesthesia-induced immobility.

6.3 Expanding the Optoanesthesia Technique

In addition to AziP*m*, it has been confirmed by K. A. Woll (University of Pennsylvania) that other alkylphenol anesthetic photolabels can be used for tadpole optoanesthesia experiments (Figure 32). Included in these is a photoactive ligand that contains a terminal alkyne functional group (Figure 32, *right*). After *in vivo* or *in vitro* photo-attachment of the ligand to protein substrates, this alkyne group can be used for conventional click-chemistry reactions whereby, e.g., an azide-linked conjugate such as biotin can be covalently attached to the photolabel-protein complex for purification with column chromatography. This specific enrichment of photolabeled protein should allow for photolabeled target identification beyond the depths achievable with IEF/SDS-PAGE or shotgun mass spectrometry methods (the latter, for example, used in Chapter 3).

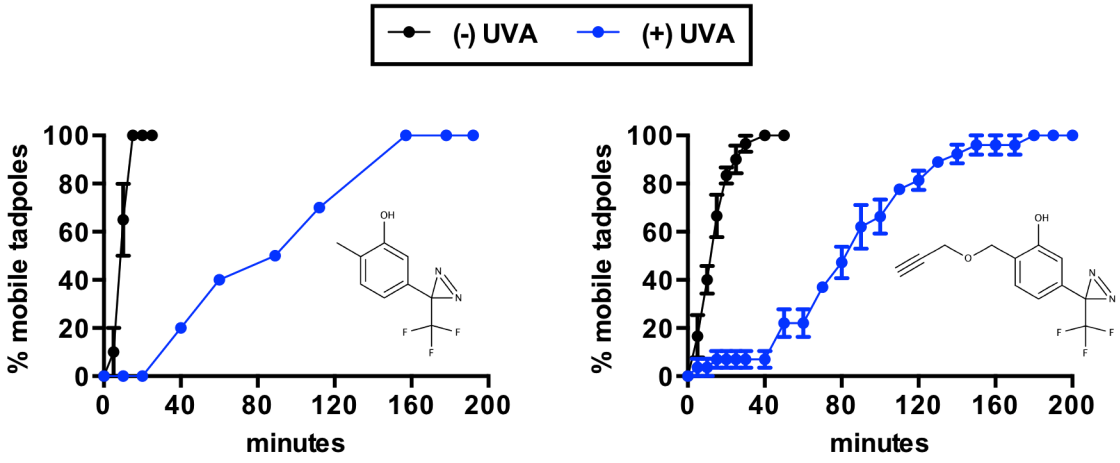

Figure 32. Tadpole optoanesthesia experiments with photoactive alkylphenol anesthetics other than AziP*m*. *(Left)* methyl-AziP*m*, (*right*) a terminal alkyne-containing AziP*m* analog. Experiments were performed essentially as in Figure 30A.

Other technical challenges should be considered when exploring mechanisms that underlie the behavioral phenotypes induced by optoanesthesia in tadpoles. For example,

each stage 45-47 *X. laevis* tadpole has a mass of 19.8 ± 3.6 mg (mean ± SD, n = 66), and the presumed target of general anesthetics, the brain, constitutes only 1.2% of this body mass. Assuming covalent binding of ligand to protein underlies the optoanesthesia-induced state, large-scale tissue harvesting for proteomic experiments is challenging albeit possible, although mass spectrometry experiments are hindered by an incompletely sequenced genome. To emphasize this issue, the sequences of *X. laevis* $GABA_A$ receptor β subunits are currently unavailable; β subunits are photolabeled by AziP*m* in mammalian receptors (Jayakar *et al.*, 2014) and presumably contribute to immobility (Jurd *et al.*, 2003). In contrast to *X. laevis*, the genome of the related *Xenopus tropicalis* is fully sequenced and annotated (Hellsten *et al.*, 2010). *X. tropicalis* is generally favored by geneticists because its cells are diploid, which simplifies mutagenesis approaches, as compared to the tetraploid cells of *X. laevis*. Use of *X. tropicalis* as a model organism could therefore ease any investigation that relies on genetic alteration of general anesthetic targets; however, this organism has yet to be established as a model to study general anesthesia.

Translating optoanesthesia to mammals is also of interest, and in addition to AziP*m*, azi-etomidate (Liao *et al.*, 2005) and other anesthetic photolabels (Yip *et al.*, 2013) have been demonstrated to be efficacious in rodents, suggesting the applicability of this technique to other anesthetic chemotypes. We have successfully photolabeled defined anatomic coordinates with [^{3}H]AziP*m* *in vivo* in a live mouse (Figure 33). This was achieved by threading a fiber optic cable, connected to a 375 nm laser, through cannulas implanted in the brain, and illuminating the laser after an IV bolus of [^{3}H]AziP*m*. This spatial control allows for photolabeling of precise brain structures in

order to test their functional relevance to specific anesthetic endpoints, and dissection of brain tissue surrounding cannula termini can theoretically be used for identification of photolabeled targets. Similar to this approach is the localized photolabeling of *X. laevis* tadpole brain regions using confocal microscopy lasers, which was performed in experiments that are further described in Chapter 7.

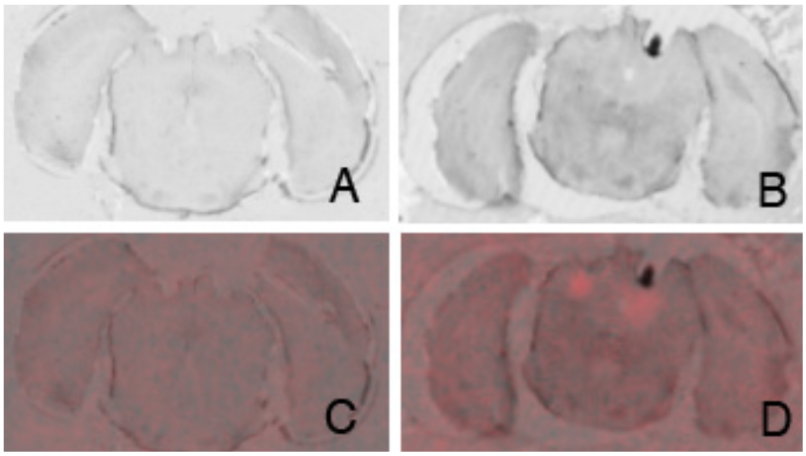

Figure 33. Two mice were each implanted with four cannulas targeting arbitrary locations. One week later, mice were anesthetized with 9% desflurane and 0.1 mg/kg [^{3}H]AziP*m* was administered as a bolus via the tail vein; immediately after the injection, desflurane concentration was adjusted to 5%. The coronal brain section micrograph in (A) was from a mouse that received no further treatment, and the brain section micrograph in (B) was from a mouse that immediately received 375 nm laser illumination (5.9 mW/mm^2) through a fiber optic threaded through the cannula; the laser was on for 0, 30, 60, or 150 seconds at each location. Desflurane administration ceased, and two hours after the injection, the mice were euthanized, perfused, and the brains were sectioned. After drying, the sections were exposed to autoradiography film; in (C) and (D), the autoradiographs (shaded red for clarity) are overlaid over the respective micrographs in (A) and (B). The autoradiograph intensity in (C) represents background. In (D), the intense spheres indicate the location of 60 second laser illumination (*left* sphere) or 150 second laser illumination (*right* sphere) (the locations of 0 and 30 second laser illumination are not visible).

CHAPTER 7: TUBULIN AS A TARGET OF ANTHRACENE GENERAL ANESTHETICS

7.1 1-Aminoanthracene (1-AMA) and 1-Azidoanthracene (1-AZA)

Previously, the Eckenhoff and Dmochowski laboratories identified 1-aminoanthracene (1-AMA) (Figure 34) as a fluorescent, GABAergic general anesthetic that reversibly induces immobility in *X. laevis* tadpoles (Butts *et al.*, 2009). The fluorescence of 1-AMA is enhanced when the ligand is shielded from an aqueous environment; thus, when occupying hydrophobic protein cavities, 1-AMA exhibits a pronounced increase in fluorescence intensity (Butts *et al.*, 2009). This characteristic of the molecule has been exploited to develop a high-throughput screen that aims to identify novel general anesthetics by, among other assays, exploring a chemical library for compounds that displace 1-AMA from the conserved anesthetic site on apoferritin (Butts *et al.*, 2009; Lea *et al.*, 2009). The fluorescence of 1-AMA has also enabled imaging of the distribution of the anesthetic *in vivo* (Butts *et al.*, 2009; Emerson *et al.*, 2012).

The efficacy of 1-AMA as an anesthetic, combined with optical and biochemical advantages of fluorescent probes over radiolabels, prompted investigation of its protein targets. To facilitate target identification, we synthesized a photoactive analog, 1-azidoanthracene (1-AZA), by replacement of the amino group with an azide. 1-AZA was synthesized from 1-AMA in two steps (Figure 34) and purified by column chromatography (Paolini *et al.*, 1998). Replacement of the amine with an azide increased the molecular weight of the otherwise isostructural compound by 26 Da. The UV-Vis spectrum of 1-AZA displayed a pronounced triple absorption peak (λ_{abs} = 350-400 nm), corresponding to the azido moiety. Complete photolysis of the azide with our UVA lamps

and lasers occurred rapidly with a half-life less than 1 minute, which is consistent with previous studies on aryl azides (Lehman and Berry, 1973). The transient product contains a reactive nitrene that is capable of protein attachment, and therefore 1-AZA was useful as a photoactive anesthetic analog (Paolini *et al.*, 1998).

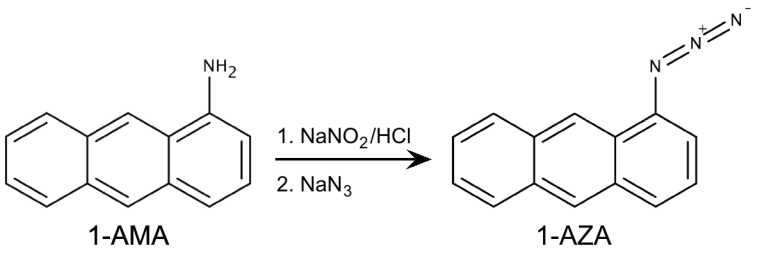

Figure 34. Synthesis of 1-AZA from 1-AMA.

7.2 *In vivo* Tadpole Photolabeling with 1-AZA

Global photolysis of 1-AZA *in vivo* revealed a similar fluorescence distribution profile to 1-AMA in the tadpole CNS (Figure 35) (Butts *et al.*, 2009). As a measure of specific binding, fluorescence intensity in the forebrain relative to the area between the forebrain and eye was quantified for 1-AZA (3.2 ± 0.8 (n = 7)) and 1-AMA (5.6 ± 1.8 (n = 5)). In contrast to 1-AMA, 1-AZA was found to be ineffective as a tadpole immobilizer. The amino group of 1-AMA hydrogen bonds with water, and replacement increases the hydrophobicity of the anthracene (calculated LogP of 1-AZA: 5.4; 1-AMA: 3.7) (Cheng *et al.*, 2007). This results in low water solubility at pH 7 (1-AZA: 7 ± 3 μM; 1-AMA: ~33 μM), which should significantly reduce target site occupancy assuming that 1-AZA and 1-AMA have similar binding affinities. However, because *in vivo* photolabeling increased the apparent potency of AziP*m* (Figure 30), we hypothesized that

in vivo photolabeling of tadpoles equilibrated with sub-anesthetic doses of 1-AZA would result in anesthesia by enhancing occupancy of molecular binding sites.

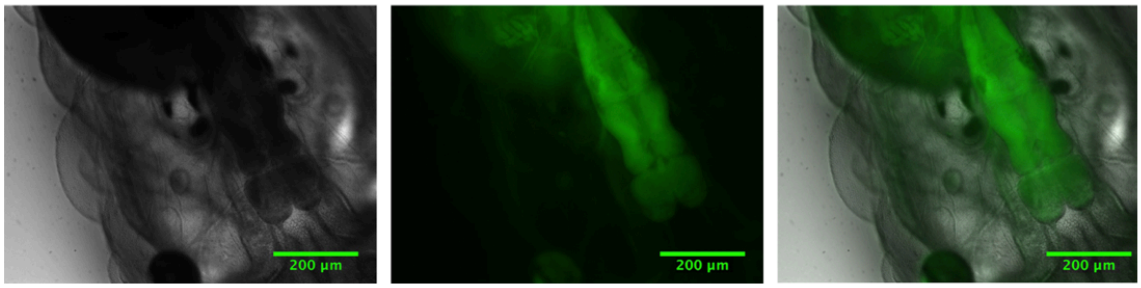

Figure 35. (A) Brightfield image (4x magnification) of tadpole brain after the organism was incubated with 15 µM 1-AZA. (B) 4x fluorescent image of tadpole brain with 15 µM 1-AZA. (C) Overlay of fluorescent and brightfield images. Scale bar is 200 µm.

After equilibrating albino tadpoles with 5 µM 1-AZA, we photolyzed 1-AZA in the forebrains of tadpoles using a UVA laser and confocal microscope; whole body labeling was found to be lethal, and the forebrain provided an explicit and isolable target for replicate experiments. Upon 1-AZA photolysis in the forebrain, 29/35 tadpoles became immobilized, although 19 of the immobilized animals subsequently died. The narrow therapeutic ratios of anesthetics and their steep dose-response Hill slopes suggest that significant changes in target binding converted 1-AZA-induced immobility into lethality. This was likely due to the rapid photolysis rate of 1-AZA and high levels of adduction to targets, whereas less photoreactive molecules such as AziP*m* provide greater occupancy tuning to avoid this toxicity. For example, AziP*m* has a photolysis half-life of 102 ± 9 min (mean ± SD) with the lamp used for AziP*m* tadpole optoanesthesia (Figure 30), during which tadpoles were photolabeled for 3-20 minutes, while essentially all of the 1-AZA underwent photolysis in these experiments.

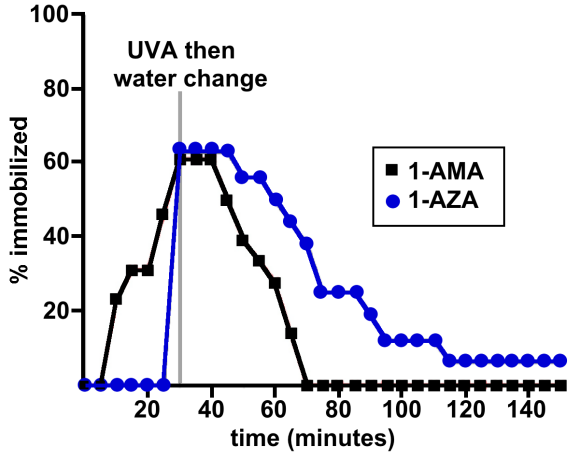

Figure 36. Time course for tadpole recovery after forebrain UVA exposure following 30 minutes equilibration in 5 μM 1-AZA or 8 μM 1-AMA.

Of the 16 (out of 35) tadpoles that survived photolabeling of the forebrain, 63% became reversibly immobilized for 54.5 ± 35.4 minutes (mean ± SD) (Figure 36). Tadpoles anesthetized with an EC_{60} dose of 1-AMA, which lacks a photoactive moiety, completely recovered within 31.2 ± 9.4 min whether or not they were treated with UVA in the forebrain (n = 13 tadpoles). Together, these *in vivo* tadpole photolabeling experiments with 1-AZA proved an immobility effect that relied on photolysis, and suggested an effect attributable to *in vivo* photolabel attachment. Thus, we hypothesized that protein targets covalently labeled by 1-AZA may be conserved substrates of anthracene anesthetics and might contribute to immobility.

7.3 Tubulin as a Target of 1-AZA

Protein from enriched tadpole neuronal membranes photolabeled *in vitro* with 1-AZA was separated by IEF/SDS-PAGE and scanned for fluorescence (Figure 37). Photolabeled spots were excised after Coomassie staining, and the major components

were identified with LC-MS/MS. Spot 1 was identified as β-tubulin and α-tubulin isoforms (Table 12). Note the absence of fluorescence in spot 2, which consisted mostly of ATP synthase subunit β, a protein with peptides also identified in spot 1. Spots 3 and 4 contained VDAC2, identified previously as a binding partner of other general anesthetic analogs (See Chapters 4 and 5), and LC-MS/MS analysis of labeled spots at ~45 kDa with isoelectric points of ~7.2-7.9 yielded multiple high-confidence identifications.

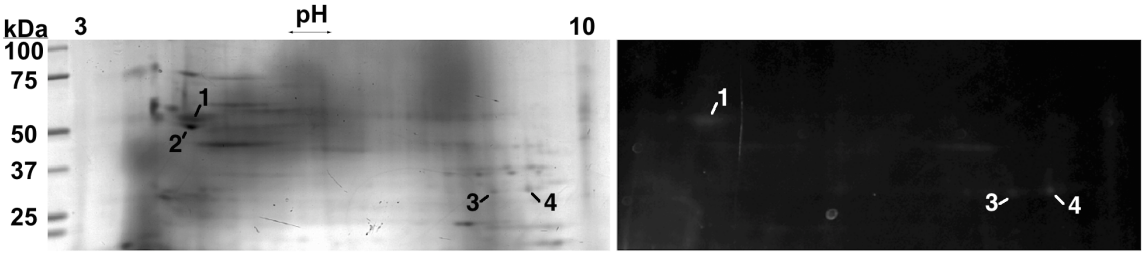

Figure 37. IEF/SDS-PAGE gel of tadpole neuronal membranes photolabeled with 1-AZA. The gel image on the left is after Coomassie staining, and the aligned fluorescence-scanned gel image (taken prior to Coomassie staining) is on the right.

Table 12. Analysis of 1-AZA-photolabeled protein from tadpole brain

Spot	Protein ID	NCBI accession #	Theor[a] MW	Obs[b] MW	Theor[a] pI	Obs[b] pI	Spectra count	Unique peptides
1	tubulin β-4	gi|28461386	49718	55714	4.82	5.01	62	14
	ATP synth β	gi|28436792	56338		5.25		26	11
	tubulin α-1	gi|28422169	49847		4.96		24	12
	tubulin β-3	gi|54311209	50309		4.79		22	7
	tubulin β-6	gi|33417142	50299		4.98		19	5
	tubulin β-2	gi|27696463	49692		4.81		19	5
	tubulin β-5	gi|29124413	49696		4.78		10	3
2	ATP synth β	gi|28436792	56338	51429	5.25	4.92	75	18
	tubulin β-4	gi|28461386	49718		4.82		3	2
3	VDAC2	gi|62826006	30183	31750	8.36	8.59	[c]	[c]
4	VDAC2	gi|62826006	30183	32500	8.36	9.23	[c]	[c]

[a]Theoretical values were computed with ExPASy Compute pI/Mw tool (http://web.expasy.org/compute_pi/). Monoisotopic molecular weights (Da) are shown.
[b]Observed values were estimated from molecular weight markers and IEF resolving estimations published by the manufacturer of the gels.
[c]Spot analysis can be found in Table 6.

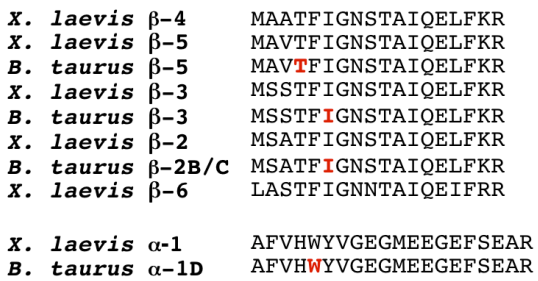

Figure 38. *B. taurus* peptides photolabeled by 1-AZA are shown, and these are aligned to the homologous *X. laevis* peptides. Residues colored red were determined with LC-MS/MS to be adducted by 1-AZA.

Disruption of microtubule dynamics as a contributor to anesthetic hypnosis has previously been suggested (Hameroff *et al.*, 2002). We therefore focused on the relevance of tubulin as a target of 1-AMA. To investigate anthracene-tubulin binding, commercially available bovine brain tubulin was used; *X. laevis* and *Bos taurus* tubulins share ≥95% sequence homology between respective isoforms. We photolabeled bovine tubulin with 1-AZA and, after SDS-PAGE, processed the tubulin samples for LC-MS/MS. We identified 1-AZA adducts on peptides that correspond to tubulin-β2/β3, tubulin-β5, and tubulin-α1D sequences (Figure 38 and Appendix A2.3). The β isoform residues were located on the S10 β sheet, and the photolabeled tryptophan of tubulin-α1D was on the H11' helix (Figure 39A). Structural evaluation revealed that the nearest atoms on labeled/homologous residues of tubulin-β2/β3 (I368) and tubulin-β5 (T366) were 3.3 and 6.7 Å, respectively, from the nearest colchicine atoms in the X-ray co-crystal structure of colchicine and bovine tubulin (PDB code 1SA0) (Figure 39B) (Ravelli *et al.*, 2004). The tubulin-α1D residue is located at the interface of an α-β heterodimer, though sterically shielded from the binding pocket by the tubulin-β H8 helix (Figure 39C).

Interestingly, previous photolabeling studies had identified tubulins as binding partners of the photoactive neurosteroid 6-azi-pregnanolone, which also binds in the tubulin-β colchicine binding site (Figure 39D) (Chen, Chen, *et al.*, 2012).

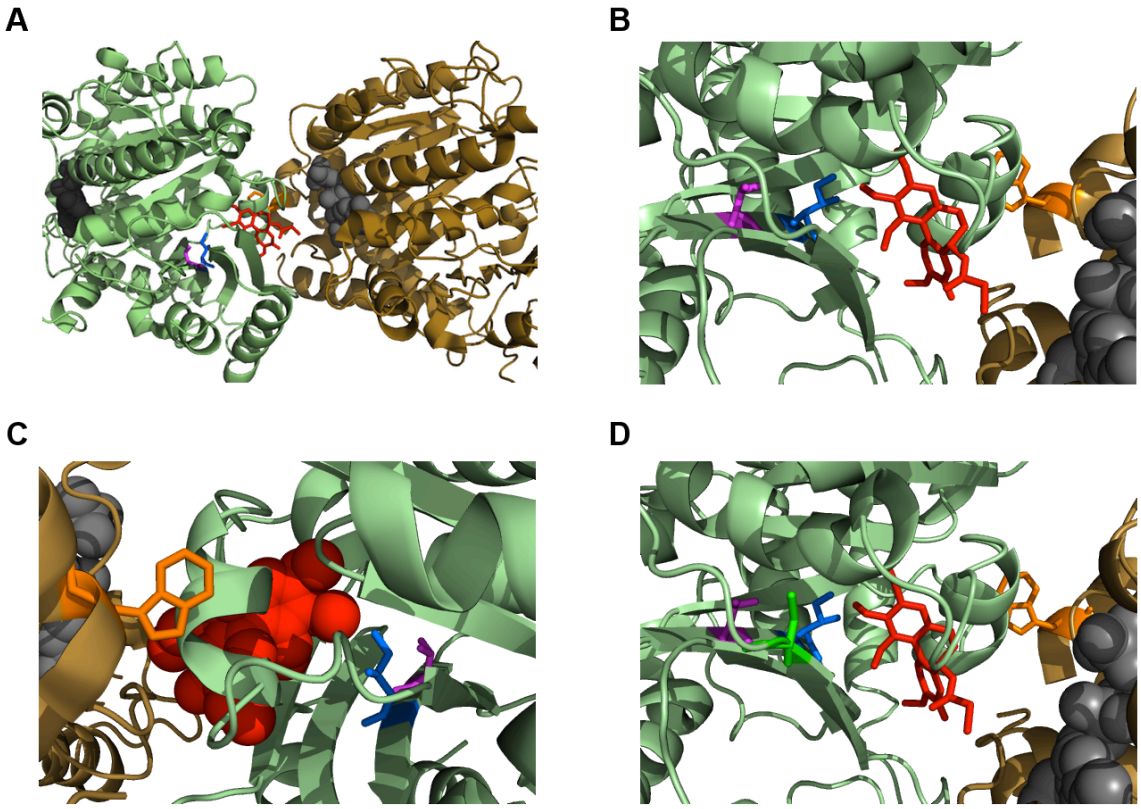

Figure 39. For all images (when applicable): tubulin β-2B is colored pale green, tubulin α-1D is colored brown, GTP and GDP are shown as spheres colored light gray and dark gray, respectively, and colchicine is colored red. 1-AZA photolabeled amino acids are also shown as sticks: tubulin-β2/β3 I368 (blue), tubulin-β5 T366 (magenta), and tubulin-α1D W406 (orange). All structures are adapted from PDB code 1SA0, and the stathmin-like domain of RB3 was removed for clarity. (A) Location of residues photolabeled by 1-AZA at the interface of β and α subunits on bovine tubulin. (B) and (C), Enlarged views of the colchicine site, with the steric shielding of W406 from the site especially visible in (C). (D) Similar view as in (B) but with C354, which is the residue photolabeled by 6-azi-pregnanolone, shown as the green stick.

To further confirm conserved anthracene binding to the colchicine site, we photolabeled tubulin with 1-AZA *in vitro* and measured fluorescence intensity. Similar to

1-AMA (Butts *et al.*, 2009), 1-AZA displayed a four-fold increased fluorescence intensity when bound to protein, which was indicative of considerable shielding from the aqueous environment. Colchicine effectively inhibited 1-AZA photolabeling of tubulin (Figure 40A). We then used a similar fluorescence-competition experiment to demonstrate that 1-AMA also binds to the same site through dose-dependent displacement of 1-AMA from tubulin by colchicine (Figure 40B).

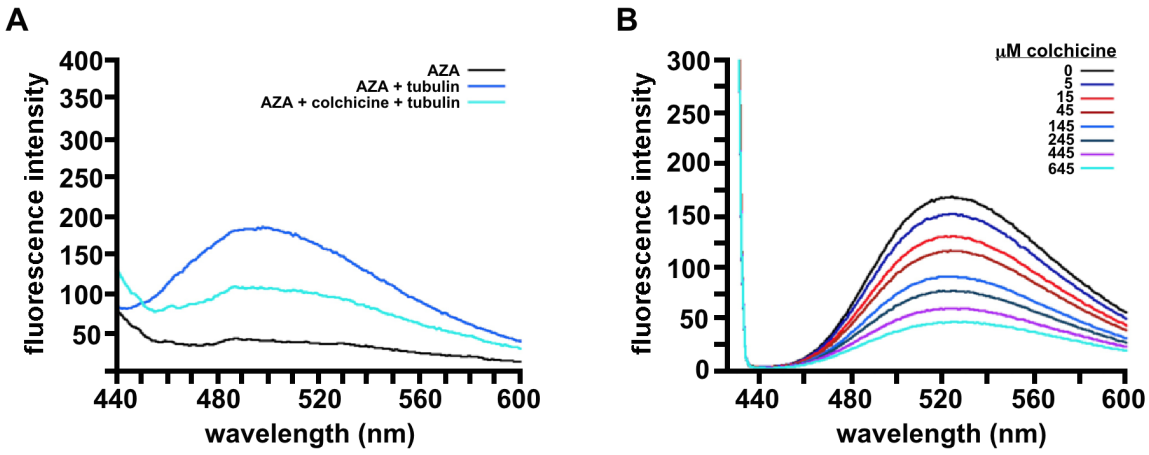

Figure 40. (A) Competition between 1-AZA and colchicine for binding to tubulin. All samples were exposed to UVA for 1.5 minutes before scanning with fluorescence using 400 nm excitation. (black) 8 μM 1-AZA, (blue) 15 μM bovine tubulin and 8 μM 1-AZA, and (cyan) 15 μM tubulin equilibrated with 20 μM colchicine before addition of 8 μM 1-AZA. (B) Competition between 1-AMA and colchicine for binding to tubulin. 100 μM tubulin was equilibrated with 33 μM 1-AMA, then colchicine (5–645 μM) was titrated into the cuvette. For (B), fluorescence was scanned using 425 nm excitation.

Finally, we investigated the effects of anthracenes on tubulin function through *in vitro* polymerization assays. 1-AZA was a potent inhibitor of tubulin polymerization, and this effect was significantly potentiated by covalent attachment of 1-AZA to tubulin (Table 13); the effect of 1-AZA was comparable to colchicine. 1-AMA was less

efficacious at inhibiting tubulin polymerization compared to 1-AZA, but still decreased the polymerization rate compared to control experiments by 20%.

Table 13. Tubulin polymerization rates with and without anthracenes and colchicine

Polymerization condition[a]	V_{max} (mO.D./min) [b]
Control (no inhibitor)	7.8 ± 0.9
14 μM Colchicine	3.1 ± 1.0
14 μM 1-AZA (pre-photolysis)	3.7 ± 1.0
14 μM 1-AZA (post-photolysis)	2.0 ± 1.5
14 μM 1-AMA	6.3 ± 0.9

[a]All assays contained 10 μM tubulin, 10% glycerol, and 2 mM GTP.
[b]V_{max} was calculated from the initial slope of the increasing absorbance at 450 nm after initiating microtubule formation.

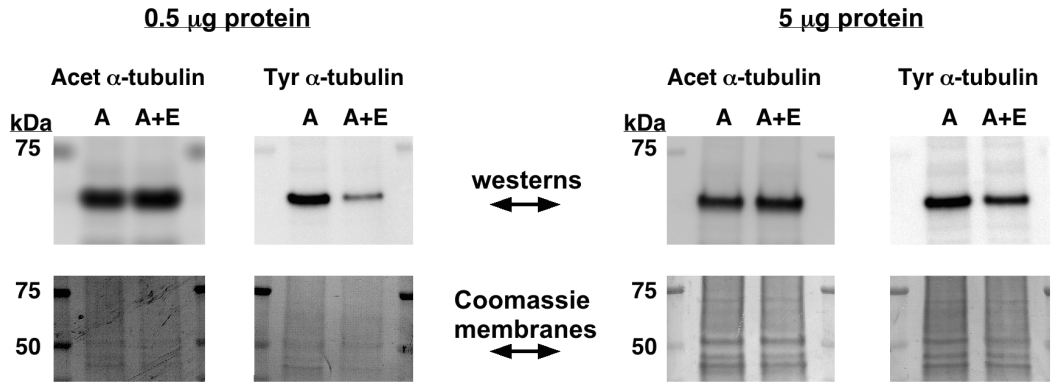

Figure 41. Increased polymerization of microtubules *in vivo*, caused by treating tadpoles with EpoD, was confirmed by western blotting for stabilized microtubule marker (acetylated α-tubulin) and soluble tubulin marker (tyrosinated α-tubulin) from isolated tadpole brains. Coomassie stained membranes are shown below for loading control. A, tadpoles treated with 1-AMA; A+E, tadpoles treated with 1-AMA + EpoD.

7.4 Shifting Sensitivity of Tadpoles to 1-AMA

Our *in vitro* data indicated that the anthracenes bind tubulin and decrease polymerization efficiency and/or stability. To test whether this contributes to the tadpole

immobility endpoint, we equilibrated *X. laevis* tadpoles with 1-AMA for 30 minutes with or without 1 hour prior treatment with 2 μM epothilone D (EpoD), a potent microtubule stabilizing agent that binds near the taxol site (Nettles *et al.*, 2004; Ballatore *et al.*, 2012). We validated the intended pharmacologic effect of EpoD *in vivo* with western blot (Figure 41); acetylation of tubulin-α Lys40 is a surrogate marker for polymerized tubulin, and tyrosination of tubulin-α indicates soluble protein (Brunden *et al.*, 2012; Magiera and Janke, 2014). For 1-AMA, the dose-response induction curve shifted to the right with EpoD-stabilization of microtubules, increasing the 1-AMA EC_{50} from 8 μM to 16 μM (Figure 42).

6-Azi-pregnanolone, which binds in the colchicine site, was also shown to inhibit tubulin polymerization (Chen, Chen, *et al.*, 2012). To investigate further the significance of neuronal tubulin as target of neurosteroid anesthetics, we incubated stage 40-47 tadpoles with allopregnanolone with and without 1 hour prior treatment with 2 μM EpoD. The immobility endpoint was assessed after 3 hours of 3 μM allopregnanolone treatment, and EpoD decreased the percentage of immobilized tadpoles from 34 ± 20% to 10 ± 7% (five experiments per treatment, 8-10 tadpoles per experiment; $p < 0.05$ with two-tailed t-test comparing the percent of tadpoles immobilized ± EpoD).

7.5 Implications of Tubulin as a Target of 1-AMA

The combined *in vivo* and *in vitro* approaches suggest that alteration of microtubule polymerization dynamics can change the effective concentration of certain general anesthetics, including 1-AMA and allopregnanolone. The aggregate effects of the

anthracenes on tubulin are consistent with those of structurally related compounds, such as anthracen-9-yl esters and substituted anthracen-9-ones, that potently inhibit microtubule polymerization and also compete with colchicine for tubulin binding (Zuse *et al.*, 2007; Prinz *et al.*, 2009). If tubulin polymerization state can modulate response to general anesthetics, it is possible that microtubule destabilizing compounds such as these anthrone derivatives and colchicine would increase the sensitivity of organisms to anesthetics.

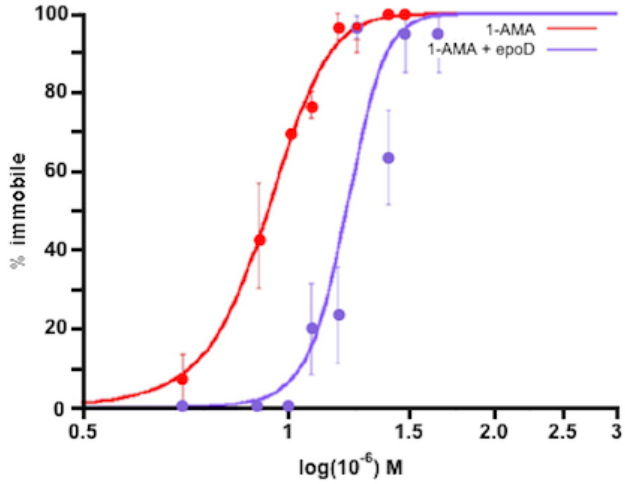

Figure 42. 1-AMA induction dose-response curve after 30 minute incubation with 1-AMA (red) or 1-AMA + 2 μM EpoD (purple). For 1-AMA alone, EC_{50} = 16 ± 0.5 μM with a Hill slope of 4.4 ± 1.1; for 1-AMA + 2 μM EpoD, EC_{50} = 8 μM ± 0.5 μM with a Hill slope of 5.4 ± 2.7.

The pharmacologic relevance of anesthetic-tubulin interactions, however, should not be over-simplified. For example, the volatile anesthetic halothane has been shown to bind tubulin but has little effect on microtubule polymerization *in vitro*, trending towards a stabilizing influence (Xi *et al.*, 2004; Pan *et al.*, 2007; Craddock *et al.*, 2012);

preliminary *in vitro* data with propofol and isoflurane also indicated that these anesthetics do not inhibit tubulin polymerization (data not shown). Thus, it is likely that microtubule destabilization per se may not be a unitary mechanism for achieving general anesthesia. This also suggests that tubulin stabilization by an anesthetic itself could antagonize the susceptibility of an organism to an anesthetic endpoint, and that other molecular targets influence systematic processes that control consciousness to a higher degree.

Finally, exactly how microtubule stability modulates susceptibility of an organism to anesthesia has yet to be determined. It is possible that tubulin binding can indirectly influence neuronal activity, based on the role of microtubules in supporting the trafficking of membrane proteins to the neuron cell surface, as well as providing a scaffold for functional ion channels such as the GABA and NMDA receptors (Passafaro and Sheng, 1999; Wang and Olsen, 2000; Eriksson *et al.*, 2010; Kapitein *et al.*, 2011). Microtubule status is intricately linked to the complement of transmembrane proteins found at the cell surface and can impact physiological ion transport (Lei *et al.*, 2012). Alternatively, although it will not be further discussed here, microtubules and the cytoskeleton have been proposed to directly underlie consciousness itself (Hameroff and Penrose, 1996), and therefore perturbation of microtubules by general anesthetics could disrupt conscious activity.

CHAPTER 8: CONCLUSIONS

The work presented in this thesis advances several aspects of general anesthetic pharmacology research. It has been demonstrated that, similar to volatile anesthetics (MF Eckenhoff *et al.*, 2002), propofol binds a multitude of proteins with both selectivity and specificity. Assuming that propofol modulates the function of even a fraction of these proteins, this implies that numerous cellular processes are modulated by the anesthetic.

Certainly, the off-pathway pharmacology of propofol is complex. Both a protein integral to the mitochondrial outer membrane (VDAC) and a soluble cytosolic/nuclear protein (SIRT2) were determined in this work to be functionally affected by propofol binding; however, these are only two of the many targets of propofol. It may be ambitious to comprehensively identify all of the substrates of propofol and to determine the functional effects of binding in order to develop a framework for the side effects of propofol in each cell type. This "bottom-up" approach taken here– from identification of molecular targets to demonstration of physiologic relevance– contrasts the more common "top-down" approach in anesthetic research, whereby observations made at the cellular or organism levels are rationalized as being caused by known anesthetic targets. The incremental merging of the information gathered with each approach should ultimately reveal which proteins underlie the most critical drug side effects.

Both bottom-up and top-down approaches have limitations. As an example, the most pronounced results are the most likely to be identified; however, the size of a result is not necessarily related to its importance. For instance, the identification of VDAC and SIRT2 as propofol targets was partially related to their abundance in tissue fractions that enabled high levels of radioactive photolabel binding. However, the relative contribution

of a protein to a cellular endpoint is not necessarily related to the abundance of the protein, and similarly, the magnitude of a change in protein function does not necessarily correlate with contribution to a pharmacologic effect. The dynamic range of molecular target identification, as well as the breadth of endpoints investigated on the organism level, must both increase.

Should modulation of VDAC or SIRT2 function be demonstrated to contribute to a deleterious side effect of propofol, it is possible that this knowledge could be incorporated into clinical practice. As an example, SIRT2 promotes re-myelination of nerve axons after crush injury; therefore, because propofol inhibits SIRT2, crush injury patients that require anesthesia might have a better outcome if propofol is avoided. This approach to clinical practice, however, would require in depth knowledge about how every general anesthetic affects SIRT2 and crush injury outcome, and also would necessitate that every side effect from every general anesthetic be considered during patient care. As an alternative example, an analog of propofol could be developed that does not bind to SIRT2 and is therefore suitable for crush injury patients; however, other side effects of this compound would also have to be examined and considered during treatment. To comprehensively understand the causes of drug side effects of any single anesthetic or chemotype will be challenging, especially as research naturally transitions to currently used clinical compounds.

The above examples stress optimizing current general anesthetics in order to improve clinical drug use. The alternative approach is to rationally develop new drug chemotypes that bind on-pathway targets with higher affinities and/or selectivity, thereby mitigating off-pathway side effects. In order to achieve this, the comprehensive set of

proteins that are affected by a general anesthetic to produce hypnosis must first be identified; no pharmacologic or genetic modulation has thus far produced complete resistance of an animal to any general anesthetic, which suggests that this full set of affected proteins has not yet been identified for any drug. As alluded to in Chapter 1, and as seen with our work on 1-AMA, the elucidation of on-pathway mechanisms is similar to that of off-pathway mechanisms, and both bottom-up and top-down approaches pose similar challenges. Novel on-pathway targets of propofol were not identified in this thesis work; however, anesthetic photolabeling and proteomic experiments are continually being refined in the Eckenhoff lab, and new strategies are being developed to avoid limitations confronted in this project. In addition, the introduction of optoanesthesia as a technique provides a powerful tool to identify not only molecular targets of anesthetics, but also targets of the drugs at the neural systems level. The work presented in this thesis should therefore facilitate the unraveling of general anesthetic mechanisms on multiple levels with the endpoint of advancing and improving anesthetic pharmacology.

APPENDIX

A1. Experimental Procedures

A1.1 Materials and Instrumentation

With the exception of compounds that were custom synthesized, chemicals and reagents were commercially available, and the sources of chemicals that are highly relevant to results are noted. 2,6-diisopropylphenol (propofol) was purchased from Sigma-Aldrich, and AziP*m* was synthesized by W. P. Dailey (University of Pennsylvania) through published methods (Hall *et al.*, 2010). AziP*m* was radiolabeled by AmBios Labs (Boston, MA) by iodinating the phenolic ring and reducing with tritium under catalytic conditions. The final product ([^{3}H]AziP*m*) was purified with HPLC. For scintillation counting, Ecolite(+) liquid scintillation cocktail (MP Biomedicals) was used with a PerkinElmer Tri-Carb 2800TR instrument; a Varian Cary 300 Bio UV-VIS spectrophotometer was used for spectroscopy. All protein assays were performed with a BCA assay kit from Thermo Fisher Scientific. First and second dimension gels, electrophoresis apparatuses, molecular weight markers, and PVDF were from Bio-Rad. [^{3}H]-sensitive film was from Amersham/GE Healthcare. Glass-backed thin layer chromatography plates were from Whatman, and these 20 cm plates were coated with a 250 μm silica gel solid phase of 60 Å porosity. Purchased lipids were PC (Sigma-Aldrich), PS (Avanti Polar Lipids), 1,2-dioleoyl-*sn*-glycero-3-phosphocholine (DOPC) (Avanti Polar Lipids), 1,2-dioleoyl-*sn*-glycero-3-phosphoethanolamine (DOPE) (Avanti Polar Lipids), and cholesterol (Sigma-Aldrich). The anti-SIRT2 antibody was from Abcam (Cambridge, England), and the immunogen was the synthetic peptide

LEDLVRREHANI corresponding to amino acids 341-352 of rat SIRT2; the anti-acetylated α-tubulin antibody, clone 6-11B-1, was from Sigma-Aldrich and recognizes acetyl-lysine-40; the anti-tyrosinated α-tubulin antibody, clone TUB-1A2, was also from Sigma-Aldrich. For AziP*m* photolabeling experiments, UVA was generated from two sources: *(1) Newport lamp:* a 100 W arc mercury lamp was filtered through colored glass UV-visible broadband (~340-615 nm) and UV bandpass (~250-375 nm) filters (lamp and filters from Newport, Stratford, CT). Light intensities (measured with an optical power meter from Thorlabs) were 28.1 $\mu W/mm^2$ and 27.7 $\mu W/mm^2$ at 350 nm and 375 nm, respectively. *(2) Rayonet lamp:* a Rayonet RPR-3500 lamp (Southern New England Ultraviolet Company, Branford, CT) with a 350 nm bulb was used (Hall *et al.*, 2010).

Animal protocols were approved by IACUC of the University of Pennsylvania or the equivalent committee from the institutions of collaborators. Albino *X. laevis* tadpoles (stage 45-47) were purchased from Nasco (Fort Atkinson, WI) and housed in supplied pond water for at least 24 hours prior to experiments. Adult female Sprague-Dawley rats (~300 g) that were purchased from Charles River Laboratories were used for all rat experiments. C57BL/6 mice (15-25 g) from Charles River Laboratories were used for all mouse experiments.

A1.2 Methods

Gel, membrane, and film scanning and quantification: Developed autoradiographs, Coomassie-stained membranes, and Coomassie-stained gels were scanned with a Bio-Rad GS-800 Calibrated Densitometer, and the Quantity One software

(version 4.6.3) that accompanies the instrument was used for optical density quantification. Western blots were scanned with a Kodak Image Station 4000MM Pro, and band quantification was performed with the accompanying Carestream Molecular Imaging Software.

Isolation of rat synaptosomes, myelin, and mitochondria: Rats were briefly anesthetized with isoflurane, decapitated, and the brains were removed. The brains were briefly washed in isolation buffer (0.32 M sucrose and 5 mM Tris, pH 7.6, supplemented with protease and phosphatase inhibitors) then transferred to fresh isolation buffer. Brains were minced and homogenized by hand with a Teflon/glass Potter-Elvehjem tissue grinder. Synaptosomes, myelin, and mitochondria were prepared essentially as described without detergent (Sims and Anderson, 2008). The purified fractions were washed three times to remove residual Percoll by pelleting and resuspension in excess isolation buffer. The fractions were then resuspended in isolation buffer and aliquots were stored at -80°C.

Preparation of rat soluble brain extract: A rat was briefly anesthetized with isoflurane before decapitation. The brain was removed and washed in ice-cold assay buffer (25 mM Tris, pH 7.6, 2 mM $MgCl_2$, 50 mM NaCl, 2 μM trichostatin A (from Sigma-Aldrich), and Roche complete protease inhibitor cocktail). The brain was transferred to ~5 ml of fresh assay buffer and homogenized by hand. The homogenate was centrifuged at 15,000 x g for 15 minutes and the supernatant was set aside. The pellet was resuspended in 1 ml of fresh isolation buffer, and after another 15,000 x g centrifugation, the supernatants were combined. This was centrifuged at 30,000 x g for 15 minutes, and the final supernatant was used as the soluble brain extract.

IEF/SDS-PAGE: Enriched or fractionated neuronal membranes, myelin, synaptosomes, or mitochondria, typically corresponding to 100-250 μg of protein, were centrifuged for 15 minutes at 15,000 x g. Following removal of the supernatant, the pellet was dissolved in 125 μl 7 M urea, 2 M thiourea, 4% CHAPS, 20 mM dithiothreitol, and 0.2% carrier ampholytes. IEF and SDS-PAGE proceeded according to the manufacturer's instructions, with 3-10 non-linear pH strips (7 cm) and 4-15% SDS-PAGE.

Western blotting: Detergent solubilized protein was separated by SDS-PAGE then transferred to PVDF. Membranes were blocked with 1.5% bovine serum albumin solubilized in TBS-T (Tris buffered saline with 0.1% Tween-20). A 1:1000 dilution of primary antibody was applied overnight in TBS-T at 4°C on a shaker. After removing the primary antibody, the membrane was washed with TBS-T, and a secondary antibody conjugated to horseradish peroxidase was applied for one hour. After washing with TBS-T, the blots were developed with Amersham ECL Select reagent and imaged with the Kodak Image Station. Typically, the blots were then washed briefly in TBS-T followed by water before staining with Coomassie R250 and drying before scanning.

Tissue preparation for section photolabeling: Rats were briefly anesthetized with halothane before perfusion with ice cold PBS, pH 7.4, via the left ventricle of the heart. The brains were quickly removed and cut into hemispheres with a sterile razor blade. The hemispheres were frozen in stirred isopentane cooled on dry ice, then stored at -80°C. The brains were mounted in Tissue Tek O.C.T. compound (Sakura Finetek USA, Inc.) and cut into 12 μm sagittal sections on a cryostat at -21°C. Sections were mounted on

chromium potassium sulfate and gelatin subbed glass slides, and the slides were stored at -80°C until photolabeling.

Brain section photolabeling. Slides were thawed to room temperature and rinsed in PBS to remove residual O.C.T. compound and any remaining halothane. The tissue sections were photolabeled with the Rayonet lamp in custom, gas-tight quartz cuvettes with 1 mm path length. The cuvettes contained 2.4 ml of 0.1 μM [^{3}H]AziP*m* in PBS for binding distribution experiments with or without propofol (3-300 μM) for competition experiments. The cuvettes were equilibrated for 15 minutes in the dark then exposed to a 350 nm lamp for 15 minutes. The slides were then rinsed for 5 minutes in PBS before consecutive washes for 20 minutes each with fresh PBS, two washes with PBS containing 1 mg/ml bovine serum albumin, two washes with PBS, and one wash with distilled water. These washes removed unbound photolabel and salt. In pilot studies, these washes effectively removed detectable radioactive ligand from slides incubated with 0.1 μM [^{3}H]AziP*m* without UVA exposure, tested by prolonged (60 day) exposure on autoradiography film. Sections were dried over desiccant then placed on autoradiography film for 18 days. After development, the films were scanned with the densitometer, and the mean optical density of each region was quantified after subtracting background.

Synaptosome photolabeling, SDS-PAGE, and autoradiography: Synaptosomes corresponding to 200 μg of protein, as determined with protein assay, were diluted to 1 mg/ml in isolation buffer. 4 μM [^{3}H]AziP*m* was added with 400 μM propofol or the DMSO vehicle for the control; the final DMSO concentration was 0.5%. After briefly vortexing and 3 minutes incubation on ice, the samples were photolabeled with the

Rayonet lamp for 20 minutes in a quartz cuvette (pathlength 1 mm). The samples were then placed in a clean tube and pelleted at 14,000 x g, and the pellet was washed twice with 800 µl 25 mM Tris, pH 7.6. After pelleting, the supernatant was discarded and the pellet was dissolved in 5% glycerol, 1% Triton X-100, 0.5% SDS, and 20 mM Tris, pH 7.6. The insoluble pellet was removed by centrifugation, and after protein assay, 50 µg of each sample was separated via SDS-PAGE. After SDS-PAGE, photolabeled protein was transferred to PVDF and exposed to film for 31 days. After development of the film, the membrane was stained with Commassie R-250, and both the film and membrane were scanned. Lane optical density was quantified from the film after subtracting background.

Preparation of brain homogenate for lipid photolabeling: Rats were anesthetized, decapitated, and the brains were removed as described above. The brains were washed in isolation buffer then transferred to fresh buffer for mincing and homogenizing. After homogenization, the homogenate was centrifuged at 1,000 x g for 10 minutes, the pellet was discarded, and the supernatant was re-centrifuged at 1,000 x g. After discarding the pellet, the supernatant was centrifuged at 13,000 x g for 10 minutes. The supernatant was discarded, and the pellet was resuspended in isolation buffer. This brain homogenate fraction is devoid of most nuclei, connective tissue, and red blood cells, and was used for experiments characterizing lipid photolabeling.

Photolabeling of brain homogenate and lipid isolation: Brain homogenate was diluted to 1.25 mg protein/ml in isolation buffer. For each lipid isolation experiment, brain homogenate corresponding to 1.5 mg protein was photolabeled with the Rayonet lamp for 20 minutes with 1 µM [^{3}H]AziP*m* in the presence of 400 µM propofol or the DMSO vehicle for the control; the final DMSO concentration was 0.25%. After

photolabeling, the homogenate was centrifuged for 10 minutes at 14,000 x g. The supernatant was discarded, and the pellet was resuspended to 1 mg/ml in 5 mM Tris, pH 7.4. This was re-centrifuged at 14,000 x g, the supernatant was discarded, and the pellet was resuspended to 10 mg/ml in 2 mM Tris, pH 7.4. From this, lipids were isolated with a Folch extraction (Folch *et al.*, 1957). Briefly, after transfer to a glass vial, chloroform and methanol were added to achieve a final ratio of 8:4:3 chloroform:methanol:H_2O. After thorough mixing, the samples were centrifuged at 1,000 x g for five minutes and the lipid-containing organic layer was isolated.

Thin layer chromatography and plate analysis: Lipid samples were concentrated to ~150 µl under N_2 gas before spotting on silica gel plates. The following standards were dissolved in methanol and were spotted in individual lanes adjacent the photolabeled samples: 250 µg PC, 250 µg PS, 250 µg DOPE, 250 µg cholesterol, and 500 nmol AziP*m*. Passive separation was achieved with a mobile phase of 64:25:4 chloroform:methanol:(28.5%) ammonium hydroxide until the migrating front was ~1 cm from the top of the plates.

After separation, the plates were dried overnight then stained in a glass box with iodine vapor. Lipid spots were marked in pencil, and the plates were scanned. The scanned plates were used to determine spot Rf (retardation factor), which was measured from the center of the spots. The spots were scraped off the silica plates into scintillation vials for lipid elution and subsequent analyses.

Phospholipid scintillation counting and phosphorous assay: Phospholipids were eluted from the scraped silica spots by adding 1 ml of 1:1 chloroform:methanol into the

scintillation vials and incubating overnight with gentle agitation. 100 µl of the eluates were added to separate scintillation vials for scintillation counting.

The remaining 900 µl (excluding the silica) were placed in glass test tubes for measuring total phospholipid via a phosphorous assay (Fiske and Subbarow, 1925). The solvent was evaporated with N_2, and 450 µl of 8.9 N H_2SO_4 was added to each tube. This was heated to >200°C for 40 minutes or until the lipid was dark yellow. This was then cooled to room temperature before 150 µl of 30% H_2O_2 was added. This was heated for 30 minutes or until clear, then cooled to room temperature. 3.9 ml of H_2O and 500 µl of 2.5 % ammonium molybdate tetrahydrate were added to each tube before mixing. 500 µl of 10% ascorbic acid was then added, and the samples were mixed then incubated at room temperature for 30 minutes. Absorbance at 820 nm was measured with the UV-visible spectrophotometer. Parallel with processing samples, a standard curve was generated with known amounts (0 to 0.65 µmol) of PC, and a linear ($R^2 = 0.99$) relationship between absorbance and total phosphorous was reproducible.

Phospholipid hydrolysis and scintillation counting: After elution of phospholipids from scraped silica, samples were dried with N_2 and resuspended in 1 ml of 9:1 acetonitrile:0.5 N HCl. This was heated to 100°C for forty-five minutes, then 3.2 ml of 5:1 chloroform:H_2O was added. This was centrifuged at 3,000 x g for five minutes, and the organic layer (containing acyl chains) and the aqueous layer (containing polar headgroups) were isolated separately (Aveldaño and Horrocks, 1983). An additional 0.5 ml of H_2O was added to the organic layer for a second extraction, and after centrifugation, the aqueous fractions were combined. 100 µl each of the organic and

aqueous fractions were scintillation counted, and relative cpm in each layer was determined after adjusting for the total extraction volumes.

Cholesterol scintillation counting and cholesterol assay: Similar to phospholipids, cholesterol was eluted from the scraped silica into 1 ml of 1:1 chloroform:methanol. Before quantifying [^{3}H]AziP*m* binding to cholesterol, it was essential to first remove non-cholesterol bound [^{3}H]AziP*m*, which migrated with cholesterol on the chromatography plates. To achieve this, the eluted samples were dried with N_2 then dried under vacuum overnight. To each sample, 150 µl of isopropanol was added, and the samples were incubated at room temperature for 2.5 hours with mild agitation. Samples were briefly sonicated for 60 seconds, then centrifuged at 14,000 x g for 20 minutes. The supernatant was extracted, and an aliquot was used to determine the cholesterol concentration using a cholesterol quantitation kit (Sigma-Aldrich). A separate 15 µl of the supernatant was then separated by reverse phase-high performance liquid chromatography with a C18 analytical column. An isocratic gradient of 60:35:5:0.1 ACN:isopropanol:H_2O:TFA with a 1 ml/min flow rate at room temperature was used, and analytes were detected using UV-Vis absorbance at 373 nm and 210 nm. Processed in parallel with brain homogenate, pure [^{3}H]AziP*m* and cholesterol controls were analyzed and resolved peaks at 3.4 and 8.5 minutes, respectively. Within brain homogenate samples, the cholesterol peak remained clearly distinct from [^{3}H]AziP*m* and unbound photolysis products, which eluted within the first 5 minutes. The cholesterol fraction, photolabeled and otherwise, was collected from 6-20 minutes and dried to 2 ml with N_2. To this, scintillation fluid was added for counting.

Myelin photolabeling with [^{3}H]AziPm and SDS-PAGE: After thawing, myelin samples were diluted to 1 mg/ml with isolation buffer. 4 μM [^{3}H]AziP*m* was added with 180 μM non-radioactive AziP*m*, the indicated concentrations of propofol, or DMSO vehicle (all contained 0.5% DMSO). After transferring to a quartz cuvette (1 mm pathlength), samples were photolabeled for 20 minutes with the Rayonet lamp. Subsequently, the sample was pelleted and the supernatant was removed. The pellet was gently resuspended in 300 μl of 25 mM Tris, pH 7.4, the sample was centrifuged, and the supernatant was discarded. The pellet was washed again by resuspension in 300 μl 25 mM Tris, pH 7.4, and after re-centrifugation, the supernatant was discarded and the pellet was dissolved in buffer with detergent (5% glycerol, 1% Triton X-100, 0.5% SDS, and 20 mM Tris, pH 7.6). Detergent solubilized protein was separated on 4-15% polyacrylamide gels. For autoradiography, protein was transferred to PVDF, and after drying, the membranes were exposed directly to film for 31 days at 4°C. After developing the films, the membranes were stained with Coomassie R-250, and the membranes and films were scanned. For scintillation counting, the gels were stained with Coomassie G-250, and after vertically separating the lanes, these were sliced horizontally into 1 mm pieces. The gel slices were dissolved overnight in sealed scintillation vials containing 350 μl 30% H_2O_2. After cooling, scintillation fluid was added for counting

Myelin photolabeling and SDS-PAGE for mass spectrometry: Myelin diluted to 1 mg/ml with isolation buffer was photolabeled with the Rayonet lamp for 20 minutes with 4 μM non-radioactive AziP*m*. After photolabeling, the sample was centrifuged and washed twice, as described above, with 25 mM Tris, pH 7.4, and the final pellet was

solubilized. 50 μg of protein was separated by SDS-PAGE in adjacent lanes. The gel was stained with Coomassie G-250, and the three gel pieces indicated in Figure 6 were excised from each lane for either trypsin or chymotrypsin digestion. After digestion, mass spectrometry analysis was performed by microcapillary reverse-phase UPLC nanospray tandem mass spectrometry (LC-MS/MS) on a Thermo LTQ-Orbitrap XL mass spectrometer. Raw data were acquired with Xcalibur, and the spectra were searched with Sequest against either a full-tryptic or partial-chymotryptic rat proteome database for protein identification. Methionine oxidation was permitted, and filters for protein identification included 10 ppm parent ion tolerance, 1 amu fragment ion tolerance, Delta CN of 0.05, and 2 unique peptides. The sequences from the proteins identified from all three bands were then compiled into a new database. With Sequest, we searched the spectra against this new database for an AziP*m* mass modification (216.07620 amu) on any amino acid of every full-tryptic or partial-chymotryptic peptide; only three residue modifications, including methionine oxidation, were allowed on each peptide. Filters for identification of modified peptides included 10 ppm parent ion tolerance, 1 amu fragment ion tolerance, Delta CN of 0.05, and Xcorr scores of 1, 2, and 3 for +1 ions, +2 ions, and +3 ions, respectively. All spectra were then inspected manually for verification.

Structural analysis of SIRT2: For SIRT2 structures, chains A from PDB codes 3ZGO and 3ZGV where used (Moniot *et al.*, 2013). 3ZGO corresponds to the inactive conformation of SIRT2, the structure of which was re-refined from the dataset of PDB code 1J8F, also a SIRT2 structure in the inactive conformation (Finnin *et al.*, 2001; Moniot *et al.*, 2013); 3ZGV represents SIRT2 bound to ADP-ribose in an active

conformation (Moniot *et al.*, 2013). Hydrogen atoms were removed, and both structures were loaded into SWISS-MODEL via the ExPASy web server (Arnold *et al.*, 2006; Guex *et al.*, 2009; Kiefer *et al.*, 2009; Biasini *et al.*, 2014). Models of human SIRT2 were re-built using the original structures (i.e., 3ZGO and 3ZGV) as the templates. This procedure built missing side chains in the structures while keeping all other atoms in the exact coordinates as the available crystal structures. The structure of human SIRT3 bound to the inhibitor EX-527 was from PDB code 4BV3 (Gertz *et al.*, 2013), and the structure of *Thermotoda maritima* Sir2 (Sir2Tm) bound to nicotinamide was from PDB code 1YC5 (Avalos *et al.*, 2005). For analysis of protein cavities, the program fpocket was used (Le Guilloux *et al.*, 2009). Visual Molecular Dynamics (VMD) (Humphrey *et al.*, 1996) and PyMOL were used for other structural analyses and preparation of structural images, and sequence alignments were performed with ClustalW2 (Larkin *et al.*, 2007; Goujon *et al.*, 2010; McWilliam *et al.*, 2013).

Photolabeling recombinant human SIRT2: Recombinant human SIRT2, representing residues 13-319, was purchased from Sigma-Aldrich, and its identity was confirmed with mass spectrometry. 50 μg/ml of recombinant SIRT2 was photolabeled with 4 μM [^{3}H]AziP*m* ± propofol with and without 2 mM ADP-ribose, 100 mM nicotinamide, and 250 ng/μl of core histones purified from HeLa cell chromatin (histones were purchased form Active Motif, Carlsbad, CA). Prior to these experiments, histone acetylation was confirmed by western blot with an acetyl-lysine antibody (Cell Signaling Technology). The substrates and ligands for photolabeling were mixed in buffer (10 mM KCl and 10 mM Hepes, pH 7.6), briefly vortexed, and samples were photolabeled in a 1

mm quartz cuvette with the Newport lamp. After photolabeling, the substrates were separated with SDS-PAGE, and the SIRT2 band was excised, dissolved in 350 μl 30% H_2O_2, and scintillation fluid was added for counting.

SIRT2 deacetylase assays: For tubulin deacetylase assays, 30 μg of the soluble brain extract protein was used, and the final assay volume was 30 μl. All components were dissolved in the assay buffer described above, and the assays were performed in 0.2 ml PCR tubes. When added to the reaction, final concentrations of 1 mM NAD^+, 100 mM nicotinamide, and 3 μg human recombinant SIRT2 were used. After briefly vortexing the assay mixture, the tubes were incubated at 37°C for 3 hours with brief mixing every 30 minutes. The reaction was terminated by adding Laemmli buffer then placing the tube in boiling water. SDS-PAGE gels and western blots for acetylated α-tubulin were typically performed with both 1 μg and 3 μg of soluble extract protein.

Mass spectrometry analysis of tadpole protein. Trypsin digested samples were separated on a nanoLC column before online electrospray into a Thermo LTQ linear ion trap. Raw data was acquired with Xcalibur, and a database downloaded from NCBI (November, 2011) with the search term '*Xenopus*' was searched with Sequest. Parameters were 1 amu parent ion tolerance, 1 amu fragment ion tolerance, and 1 missed cleavage. The search result files were combined with Scaffold 3 and filtered with the criteria: Xcorr scores (+1 ion) 1.7, (+2) 2.3, (+3) 2.8; protein identification confidence 99.9%; peptide identification confidence 95%; 2 peptide minimum. Spectra were manually inspected to ensure quality and confidence.

Rat VDAC identification and LC-MS/MS: Rat mitochondria were pelleted, and after removing the isolation buffer, pellets were washed twice with ice-cold 2 mM Tris, pH 7.4. Mitochondrial protein was separated by IEF/SDS-PAGE then stained with Coomassie G-250. Protein spots that were candidates for containing VDAC were identified based on molecular weight and isoelectric point. These were excised for LC-MS/MS. Cysteines were alkylated, and after trypsin digestion, samples were injected into a nanoLC column with online electrospray into a Thermo LTQ linear ion trap. XCalibur acquired raw data, and Sequest searched b and y ions. For protein identifications, a database was downloaded from www.uniprot.org with the search term "rattus norvegicus". Search parameters were 1 amu parent ion tolerance, 1 amu fragment ion tolerance, full tryptic digest, one missed cleavage, variable methionine oxidation, and fixed cysteine carboxyamidomethylation. Filter parameters were Xcorr scores (+1 ion) 1.5, (+2 ion) 2.0, (+3 ion) 2.5, deltaCn 0.08, peptide probability >0.05, and two unique peptides.

Mitochondria photolabeling: Rat mitochondria were diluted to 1 mg/ml in isolation buffer before adding ligand(s). Samples were incubated at room temperature in the dark for 10 minutes before photolabeling in a quartz cuvette (pathlength 1 mm) for 15 minutes with the Newport lamp. After photolabeling, mitochondria were pelleted and washed with ice-cold isolation buffer, pelleted again, then washed twice with 2 mM Tris, pH 7.4. Subsequently, the pellet was dissolved in IEF/SDS-PAGE buffer for two-dimensional electrophoresis.

Scintillation counting of VDAC spots: After IEF/SDS-PAGE of mitochondrial protein photolabeled with [^{3}H]AziP*m*, gels were Coomassie stained and scanned, and

spot intensity was quantified. VDAC protein spots were then excised, dissolved in H_2O_2, and scintillation counted. Scintillation counts were normalized to spot intensity (i.e., protein abundance) for quantitative analyses.

Identification of AziPm binding sites on VDAC: Mitochondria photolabeled with AziP*m* were separated with IEF/SDS-PAGE, the gels were stained, and protein spots were excised and processed for LC-MS/MS as above after either trypsin or chymotrypsin digestion. After LC-MS/MS, the spectra were searched against rat sequences of VDAC1, VDAC2, VDAC3, and malate dehydrogenase 2. The search parameters and filters described above were used along with a maximum of three post-translational modifications per peptide and a variable AziP*m* modification (+216.08 Da) on any residue. To sequence the N-terminus of VDAC1, however, a specific search for alanine acetylation with partial tryptic digest was required (Kayser *et al.*, 1989). This procedure confirmed that the N-terminal methionine of VDAC1 is removed during protein maturation *in vivo*, and also that the second coded residue (alanine) is acetylated (Kayser *et al.*, 1989); however, we included the coded methionine (Met1) in the numbering of amino acids. For protein sequencing, only the highest scoring peptide assignment for each spectrum was considered, and spectra of peptides containing AziP*m* adducts were manually confirmed.

Structural analyses of VDAC-propofol binding sites: For structural analyses of rat VDAC1, we used PDB code 3EMN, which represents a crystal structure of recombinant rat VDAC refolded from inclusion bodies (Ujwal *et al.*, 2008). This was oriented in a hypothetical membrane with the PPM server of Orientation of Proteins in the Membrane (Lomize *et al.*, 2012), and PyMOL was used for generating structural images. In addition

to the 3EMN structure, we referenced a proposed, alternatively-folded VDAC protein with a structural topology that was deduced from experimental studies and has been described elsewhere (Song *et al.*, 1998; Colombini, 2004, 2009). This protein is proposed to contain an integral transmembrane helix and 13 β-strands (Song *et al.*, 1998; Colombini, 2004, 2009); however, a high-resolution structure of VDAC that is folded in this manner is not available.

Reconstitution of rat VDAC into planar lipid bilayers: Frozen mitochondrial membranes from rat liver were kindly provided by Marco Colombini (University of Maryland, College Park). VDAC was isolated from the membranes by the standard method (Blachly-Dyson *et al.*, 1990) and purified on a 2:1 hydroxyapatite:celite column following a previously described protocol (Palmieri and De Pinto, 1989). Purified VDAC was stored at ~0.2 mg/ml in 10 mM Tris, pH 7.0, 50 mM KCl, 1 mM EDTA, 2.5% Triton X-100, and 15% DMSO at -80°C.

Planar lipid bilayers were formed from a lipid mixture of 1:1 DOPC:DOPE in pentane from two opposed preformed lipid monolayers as described previously (Rostovtseva *et al.*, 2006; Teijido *et al.*, 2014). Channel reconstitution was achieved by adding 0.1-0.2 µl of purified VDAC to the ~1.2 ml aqueous solution of 1 M KCl buffered with 5 mM Hepes, pH 7.4, in the *cis* compartment while stirring.

Electrophysiological recordings of VDAC: All electrophysiology experiments were performed essentially as described (Rostovtseva *et al.*, 2006; Teijido *et al.*, 2014). Membrane potential was maintained by Ag/AgCl electrodes with 3 M KCl and 15% agarose bridges. Potential was defined as positive when it is greater on the *cis* side, i.e.

the side of VDAC addition. An Axopatch 200B amplifier (Axon Instruments, Inc.) was used in voltage clamp-mode. Single-channel currents were filtered by the amplifier low-pass Bessel filter at 10 kHz. Data were acquired with a Digidata 1440A board (Axon Instruments, Inc.) at a sampling frequency of 50 kHz for single-channel recordings, which were analyzed with pClamp 10.2 software (Axon Instruments, Inc.).

For multichannel experiments, a symmetrical 5 mHz triangular voltage wave with amplitude ± 60 mV was applied with a Hewlett Packard 33120A waveform generator (Rostovtseva *et al.*, 2006; Teijido *et al.*, 2014), and data was saved with a 1 Hz sampling frequency. Current responses to 5-10 periods of triangular voltage waves were recorded. For subsequent analyses, the parts of the wave in which VDAC re-opens (i.e., -60 mV to +10 mV, and +60 to -10 mV) were used. Relative multichannel conductance and open probability plots were calculated based on a previously described approach to gating analysis (Rostovtseva *et al.*, 2006; Teijido *et al.*, 2014). The gating parameters V_0 and n were calculated from the open probability plots as extensively discussed elsewhere (Colombini, 1989; Thomas *et al.*, 1993; Rostovtseva *et al.*, 2006).

After collecting control data (0 μM propofol), both in single and multichannel experiments, propofol diluted in 1 M KCl, 5 mM Hepes, pH 7.4, was then added to the bath in both the *trans* and *cis* compartments while stirring, and measurements were again collected. After each experiment, the *cis* and *trans* aqueous solutions were collected and the volumes were measured to determine exact propofol concentrations, which were then confirmed with UV spectroscopy.

Gramicidin A experiments: Planar bilayers of 1:1 DOPC:DOPE were formed as described above in 1 M KCl with 10 mM Hepes, pH 7.2. Gramicidin A from 10^{-9} M

ethanol stock solution was added to both aqueous compartments at the amount sufficient to give a single channel activity (~1 μl) (Gramicidin A was a generous gift of O.S. Andersen, Cornell University Medical College). For gramicidin A channel lifetime and conductance, the records were digitally filtered at 2 Hz using Bessel algorithm and analyzed using Clampfit 10.2 software as described previously (Rostovtseva *et al.*, 2006). After control recordings were obtained, propofol dissolved in 1 M KCl and 10 mM Hepes, pH 7.4, was added in increasing concentrations to both compartments. Mean channel conductance was calculated from Gaussian fits to current amplitude histograms, and channel lifetimes were calculated from fits to logarithmic single exponents of at least 250 channel events (Rostovtseva *et al.*, 2006).

Docking cholesterol to human VDAC in silico: Four residues in the mouse crystal structure of VDAC1 (PDB code 3EMN) (Ujwal *et al.*, 2008) were mutated in PyMOL to humanize the protein (Asp55→Thr55, Val129→Met129, Ser160→Ala160, Val227→Ile227). The N-terminal methionine (Kayser *et al.*, 1989), water, and detergent were removed before loading the structure into AutoDockTools (Sanner, 1999; Morris *et al.*, 2009). To the protein, hydrogens were added, non-polar hydrogens merged, and Kollman charges were added. Molecular coordinates for cholesterol were downloaded from the CHARMM small molecule library (MacKerell *et al.*, 1998; Foloppe and MacKerell, Jr., 2000); in AutoDockTools, Geisteiger charges were added, non-polar hydrogens merged, and 6 torsions were allowed (i.e., cholesterol was fully flexible). For docking, grid boxes targeted the specific cholesterol sites and biased the exterior, membrane side of the β-barrel. Residue side chains in the site of interest and projecting

outside the barrel were flexible during docking runs with AutoDock Vina (Trott and Olson, 2010). AutoDock was programmed to return six docking results with search exhaustiveness of 100. The highest scoring poses were generally chosen for simulations. Multiple docking calculations with different grid centers were performed on some sites to increase heterogeneity in the starting poses.

VDAC MD Simulation System Setup: After docking, PDB files of VDAC, the docked cholesterol molecules, and corresponding flexed residues were created. The protein pore was oriented along the z-axis, normal to the membrane, using the PPM server of Orientations of Proteins in the Membrane (Lomize *et al.*, 2012), and the output models were loaded into the CHARMM-GUI Membrane Builder (Woolf and Roux, 1996; Jo *et al.*, 2007, 2009). In all simulations, the N-terminal residue (Ala2) was oriented to place it at $z < 0$. Ala2 was acetylated (Kayser *et al.*, 1989), and residues were protonated according to their standard states at pH 7.4. The water thickness (minimum height on the top and bottom of the system) was 15.0 Å.

For some simulations, 5 cholesterols were docked to the protein, and 160 DOPC molecules (80 in each leaflet) and 11 randomly distributed cholesterols comprised the membrane. For other simulations, 160 DOPC and 16 cholesterols comprised the membrane with no cholesterols docked to VDAC. As a reference, phosphatidylcholines are the most abundant mitochondrial outer membrane phospholipids at 43-50 mole percent, with cholesterol 8-11 mole percent (Colbeau *et al.*, 1971; Cheng and Kimura, 1983). 23 K^+ and 25 Cl^- ions were randomly placed by the CHARMM-GUI to neutralize each system and provide a salt concentration of 0.15 M KCl. Systems were separately generated with the CHARMM-GUI server, hence system details (number of atoms,

starting coordinates, etc.) differed between simulations. Systems were approximately 87 Å, 87 Å, and 74 Å in x, y, and z dimensions, respectively, with about 56000 total atoms that included about 9100 TIP3P waters.

VDAC MD simulation details: Atomistic molecular dynamics simulations were run with NAMD v2.9 (Phillips *et al.*, 2005). The CHARMM36 model was used for protein (MacKerell *et al.*, 1998, 2004; Best *et al.*, 2012) and phospholipid (Klauda *et al.*, 2010, 2012) parameters, and the modified (CHARMM) 36c model was used for cholesterol (Lim *et al.*, 2012); parameters for TIP3P waters (Jorgensen *et al.*, 1983) and ions (Beglov and Roux, 1994) are well established. All simulations used periodic boundary conditions and particle mesh Ewald (PME) electrostatics. Interactions between non-bonded atoms were cutoff at 12 Å, and bonds involving hydrogen were constrained using the SHAKE/RATTLE algorithm. A Langevin thermostat and barostat were used to maintain a temperature and pressure of 303.15 K and 1 atm, respectively, and no surface tension was imposed. The simulation timestep was 2 fs. Prior to production, 20000 minimization steps and a 0.725 ns equilibration protocol detailed elsewhere (Jo *et al.*, 2007) were performed on each system to gradually release restraints on the protein.

VDAC MD Trajectory Analyses: Production simulations were analyzed with VMD (Humphrey *et al.*, 1996). Every 20 ps snapshot was used for all quantitative analyses. Generally, the trajectories were aligned to and centered around the backbone of the crystal structure before performing the following analyses: RMSF: Root mean square fluctuation was measured for residue α carbons and describes the fluctuation of the atom relative to its average position throughout each simulation. Ion diffusion: Cl^-/K^+ permeability ratios were determined after normalizing the number of ions that diffused

through the pore to the total number of that type of ion in the system (23 for K^+ and 25 for Cl^-). Diffusion was defined as traversing the membrane through the channel pore from -20 Å to 20 Å, or vice versa, along z. The protein spanned these coordinates in every frame of every simulation, as detected with the HOLE software (Smart *et al.*, 1993). Channel radius: The minimum channel radius for each frame was measured with the HOLE software, which fit consecutive spheres inside the channel with the centers spaced every 0.5 Å along the z axis. Hydrogen bonds: Hydrogen bonds were calculated with the Hydrogen bond plugin of VMD with a 3.3 Å and 20° donor-acceptor cutoff. Electrostatics: The protein, membrane, and water contribution to the electrostatic potential was generated with the PME electrostatics plugin (PMEPot) using 88 x 88 x 80 grid position counts (~1 Å spacing) (Aksimentiev and Schulten, 2005). The generated maps contained an identical number of data points from each simulation (the dimensions of the systems were also essentially identical). Potential of mean force: Averaged multi-ion potential of mean force plots were made for each trajectory. For each frame, we measured both the number of ions and the number of water molecules in a cylinder of radius 15 Å that ran parallel to the z-axis through the center of the channel. This was used to calculate the concentration of ions, C(z), in 1 Å bins, and the relative free energy was estimated with the equation:

$$\Delta G = -RT \ln[C(z)/C_{bulk}]$$

where R is the gas constant, T is the temperature, and C_{bulk} is the concentration of ions in the bulk water (Rui *et al.*, 2011). Ionic density: Ionic density maps for entire trajectories were generated with the VolMap tool plugin of VMD.

Tadpole immobility studies for alkylphenol anesthetics: Tadpoles were placed in Petri dishes with propofol or AziP*m* dissolved in pond water. In some experiments, after 30 minutes equilibration, tadpoles were transferred to fresh water; in others, after equilibration, tadpoles remained on the bench for a sham control or were exposed to UVA before transfer to fresh water. Immobility/anesthesia was defined (and scored) as the percentage of tadpoles that did not swim, twitch, or right themselves throughout a thirty-second time window preceding every ten-minute interval. Alternative causes of immobility in our study (e.g., muscular toxicity) were not ruled out, but should have had additional and toxic features that would have been observed (e.g., cardiac muscle dysfunction, etc). The water temperature was 21-22°C for experiments and changed < 0.5°C throughout any experiment.

In vivo tadpole photolabeling for isolation of neuronal membranes: Tadpoles were incubated for 30 minutes with 4 μM [^{3}H]AziP*m* and photolabeled for 10 minutes with the Newport lamp. After transfer to fresh water, tricaine methanesulfonate (500 mg/L) was added immediately for the 0 time point or at 165 minutes for the emergence time point, and the tadpoles were placed on ice. After decapitation, brains and spinal cords were removed with forceps under a dissecting microscope, and placed in ice-cold 0.32 M sucrose, 5 mM Tris, pH 7.4 supplemented with protease inhibitors. Tissue isolation required less than 15 minutes following each time point; CNS tissue was homogenized every 3-5 minutes using a Teflon/glass homogenizer.

CNS homogenates were centrifuged at 100,000 x g for 10 minutes, washed with isolation buffer, and re-centrifuged. The pellet was homogenized in 5 mM Tris, pH 7.4

and centrifuged at 100,000 x g for 10 minutes, washed, and centrifuged again before resuspension in 2 mM Tris, pH 7.4. An aliquot was removed for a protein assay prior to freezing at -80°C.

In vitro photolabeling of tadpole neuronal tissue: Unexposed tadpoles were anesthetized with tricaine methanesulfonate and neuronal tissue, dissected as above, was homogenized in sucrose buffer, centrifuged at 100,000 x g for ten minutes, washed, and re-centrifuged. The pellet was suspended in isolation buffer, protein concentration determined, then diluted to 1 mg/ml in a microcentrifuge tube. 4 μM [^{3}H]AziP*m* ± 400 μM propofol was added and, after a brief vortex, was incubated at 21°C in the dark for 10 minutes. After transfer to a quartz cuvette (pathlength, 1 mm), the tissue was photolabeled for 10 minutes using the same light source as above. The homogenates were then centrifuged at 100,000 x g, homogenized in 5 mM Tris, re-centrifuged at 100,000 x g, washed, and stored at -80°C in 2 mM Tris.

Scintillation counting of tadpole neuronal tissue: Dissected CNS tissue from tadpoles treated with 4 μM [^{3}H]AziP*m* with and without photolabeling with the Newport lamp was placed in 1 ml ice-cold 2% SDS, 1% Triton X-100, 5 mM Tris, pH 7.4 supplemented with protease inhibitors. Following homogenization, the protein concentration was determined. 5 and 10 μl of the homogenates were added to separate vials in scintillation fluid. The disintegrations per minute (dpm) from each vial were normalized to the corresponding protein amount, and the mean of the two values was used for a single experimental measurement.

Spot intensity quantitation and scintillation counting from tadpole tissue gels:

Gels were washed with water and fixed overnight in 15% trichloroacetic acid before staining with Coomassie G-250. After destaining, the gels were scanned and quantification performed with Quantity. Background was subtracted with a box drawn between the 50 and 75 kDa molecular weight markers, and mean optical density multiplied by spot area was recorded from contoured spots.

Spots were excised with a 1.5 mm cylindrical hole punch and placed into scintillation vials. 400 μl of 30% H_2O_2 was added and the sealed vials were incubated overnight at 65°C to dissolve the polyacrylamide. These were cooled to room temperature before adding scintillation fluid.

Microscopy methods for 1-AMA and 1-AZA: Fluorescence experiments were performed with an Olympus Fluoview FV1000 confocal laser scanning microscope equipped with inverted IX81 microscope with visible laser (488 nm Ar ion) for 1-AMA and 1-AZA imaging and UVA lasers (351, 364 nm, Enterprise II system) for *in vivo* photolabeling. Tadpoles incubated with 1-AZA in pond water were irradiated with both UVA lasers (100% power) by rastering over the forebrain using an Olympus air objective UPLSAPO 10x (NA: 0.40) with dwell time of 2 μs per pixel. Images for Figure 35 were collected with a hyperspectral CCD (CRi Nuance FX) camera with collection window centered at 520 nm (bandwidth FWHM: 20 nm), coupled to an inverted fluorescence microscope (Olympus IX81). Samples were excited with a mercury lamp with a CFP filter set (excitation filter BP400-440, dichroic mirror DM455, emission filter BA475). An Olympus air objective UPLSAPO 4x (NA: 0.16) was used to collect images.

Synthesis of 1-azidoanthracene: A solution of sodium nitrite (0.088 mg, 1.3 mmol, 1.2 eq.) in water (0.5 ml) was added dropwise at 0 °C over 10 minutes to a solution of 1-AMA (0.201 mg, 1.04 mmol, 1.0 eq.) dissolved in 20% HCl (3 ml). The reaction mixture was stirred at 0 °C for 30 minutes before sodium azide (0.085 g, 1.3 mmol, 1.2 eq.) in water (0.5 ml) was added dropwise over 10 minutes. The solution was slowly warmed to room temperature and stirred for 4 hours. Extraction with diethyl ether gave the crude product as brown solid, which was purified by silica gel flash column chromatography (hexane: CH_2Cl_2, 20:80, v/v) to yield 0.081 g (0.37 mmol, 35% yield) of 1-AZA as a red solid. TLC and NMR data on the final product can be found elsewhere (Emerson *et al.*, 2013).

Localized in vivo photolabeling with 1-AZA: Tadpoles were incubated for 30 minutes in 5 ml artificial pond water (3.15 mM $CaCl_2$, 30.36 mM NaCl and 0.59 mM $NaHCO_3$ in deionized water) with 0.5% ethanol containing 15 μM 1-AZA. Tadpoles were briefly washed with fresh water and directed into a Delta T culture dish (Bioptechs). The Delta T culture dish consisted of a coverslip at the bottom with a tapered agarose channel (solidified 1% w/v in water) to restrict movement. Once here, the tadpoles forebrains were photolabeled as described above in *Microscopy methods for 1-AMA and 1-AZA.*

In quantifying anesthetic emergence after anthracene and UVA treatment, individual tadpoles were incubated with for 30 minutes with 1-AMA or 1-AZA ± localized UVA exposure. Subsequently, each tadpole was placed in 5 ml fresh pond water to assess anesthetic endpoints. Tadpoles scored as ‘immobile’ did not swim, twitch,

or right themselves for 30 seconds, nor did they respond to a gentle tail stroke manually administered with the blunt end of a sterile cotton swab. Death was determined by cessation of heartbeat, visible by microscope through the organism.

Induction assays, 1-AMA: Ten tadpoles per dish were equilibrated with 1-AMA (5–60 μM) for 30 minutes before assessing immobility as described above. The pond water contained 0.5% ethanol for 1-AMA solutions below 30 μM and 1% ethanol above 30 μM. For some experiments, tadpoles were incubated with 2 μM EpoD for 1 hour before addition of 1-AMA. Pond water samples were assayed by UV-Vis spectroscopy immediately after experiments to ensure soluble 1-AMA concentrations were maintained. The tadpoles were then placed into fresh pond water for recovery.

Induction assays, allopregnanolone: Tadpoles were equilibrated with the neurosteroid allopregnanolone (3α-hydroxy-5α-pregnan-20-one) in pond water. Allopregnanolone was added from a 6 mM stock solution in DMSO such that DMSO volume was negligible (<0.06%). Tadpoles were transferred to fresh allopregnanolone solution after 1.5 hours to ensure a stable anesthetic concentration. Tadpole immobilization was recorded after 3 hours.

Preparation of tadpole tissue for post-translationally modified tubulin western blotting: Tadpoles were treated with 60 μM 1-AMA in pond water for 30 minutes with or without prior incubation with 2 μM EpoD for 1 hour (similar to the *Induction assay* method, except here 15 tadpoles were used for each treatment). After treatment, the dishes containing the tadpoles were placed on ice. Individually, the brains were removed with forceps under a dissecting microscope after decapitation behind the hindbrain.

Tissue was placed directly in 20 mM Tris, pH 7.6, 5% glycerol, 1% Triton X-100 and 0.5% SDS supplemented with protease inhibitors; after homogenization the samples were frozen at -80 °C. The two groups of tadpoles (± EpoD) were treated with the same stock of 1-AMA, but not simultaneously to ensure timely removal of neuronal tissue following treatment. Less than 5 minute was required to isolate tissue from each group following the 30 minute 1-AMA equilibration.

After thawing, the insoluble pellets were removed by centrifugation, and a protein assay was performed on the supernatants containing solubilized neuronal protein. This protein was then separated via SDS-PAGE for acetyl-tubulin and tyrosinated-tubulin western blots.

In vitro tadpole photolabeling: Following tricaine methane sulfonate anesthesia, tadpoles were dissected with brains isolated, homogenized in sucrose isolation buffer, and washed. Photolabeling of the isolated neuronal membranes proceeded with an oversaturated solution of 1-AZA (~200 μM). After 5 minutes incubation in the dark, the homogenate was photolabeled for 1 minute in a quartz cuvette (pathlength 1 mm) with the Rayonet lamp. The photolabeled membranes were washed and prepared for IEF/SDS-PAGE. After separation, the gel was washed with water and scanned with the Kodak Image Station with 400 nm excitation and 535 nm emission filters. The gel was subsequently stained with Coomassie G-250 and reimaged. Spots excised from the gel were analyzed with LC-MS/MS, as described below.

Mass spectrometry analysis of AZA-photolabeled samples: Following IEF/SDS-PAGE and staining, spots excised from the AZA-photolabeled tadpole neuronal gel were

trypsin digested and processed by nanoLC-MS/MS with a Thermo LTQ linear ion trap. Raw data were acquired with Xcalibur, and Sequest was used to search b and y ions from a *Xenopus* protein sequence database downloaded from the National Center for Biotechnology Information website. Search parameters were 1.5 amu parent ion mass tolerance, 1 amu fragment ion mass tolerance, and 1 missed cleavage. Cysteine carbamidomethylation and methionine oxidation were permitted as variable modifications, and search result files were filtered with the following criteria: 99.9% protein identification confidence with 2 peptide minimum, and peptide Xcorr scores of (+1 ion) 1.7, (+2 ion) 2.3, (+3 ion) 2.8.

In addition, bovine tubulin (from Cytoskeleton, Inc.) was used for mass spectrometry sequencing experiments. The protein was incubated with an oversaturated 1-AZA solution (200 μM) for 20 minutes under polymerizing conditions (see *Polymerization assay* method) before irradiating with the Rayonet lamp for 1 minute. SDS was added to the solution, and covalent attachment was confirmed via fluorescence after SDS-PAGE by scanning the gel. After Coomassie staining, the ~50 kDa monomer band was excised for analysis. Samples were processed as above, but spectra were searched against a database composed of thirteen *B. taurus* tubulin isoforms (six α- and seven β-tubulin sequences). Search parameters and filters described above were used, but with the additional permission of a variable 191.24 amu modification on each amino acid (corresponding to a 1-AZA photolabel adduct). High scoring spectra were manually inspected to ensure quality and confidence.

Polymerization assay: Bovine tubulin (>99% purity) purchased from Cytoskeleton, Inc. (Denver, CO) was resuspended in ice-cold 1x BRB80 buffer (1 mM $MgCl_2$, 1 mM EGTA, 80 mM PIPES, pH 6.9) at 6 mg/ml, and aliquots were snap frozen in liquid nitrogen. As needed, these were thawed on ice, and diluted to achieve final concentrations of 1x BRB80, 10% glycerol, 1.7% DMSO, 10.9 μM tubulin and 14 μM test compound (colchicine, 1-AMA, or 1-AZA). In some 1-AZA experiments, this mixture was initially irradiated with UVA for 20 seconds. The mixed reagents were added to a cuvette that was temperature controlled at 37 °C. This was blanked, and GTP was added to achieve a final concentration of 2 mM. Absorbance was recorded at 450 nm in order to avoid potential absorption from colchicine, 1-AZA, and 1-AMA.

Anthracene-colchicine competition: For 1-AZA experiments, 15 μM tubulin was incubated for 10 minutes in 1x BRB80 with 8 μM 1-AZA and 50 μM colchicine at 4 °C. Irradiation with UVA then proceeded for 1.5 minutes to ensure complete 1-AZA photolysis. Fluorescence spectra were recorded with 425 nm excitation. For 1-AMA experiments, 100 μM tubulin in 1x BRB80 was incubated with 50 μM 1-AMA for 10 min before varying colchicine concentrations were added at 4 °C. Tubulin was maintained in the depolymerized state for both 1-AZA and 1-AMA experiments. Binding/covalent labeling was monitored by fluorescence intensity at 4 °C. The fluorimeter PMT was set to 800 V, with excitation and emission slit widths of 5 nm. The peak for 1-AZA corresponding to labeled tubulin was recorded at 500 nm and around 520 nm for 1-AMA. Upon colchicine addition, loss of binding was seen with 1-AMA

(intensity reduction with red-shifted emission). When 1-AZA was titrated into tubulin pre-incubated with colchicine, loss of labeling was also seen through signal reduction.

A1.3 Figures and Statistics

Data analysis and figure preparation: Where applicable, mean values are reported with standard error unless otherwise noted. Data analysis and graphical figures were generally performed with either GraphPad Prism or KaleidaGraph software; detailed statistical tests and procedures are generally noted in the text or legends were applicable. Structural figures were generated with VMD and PyMOL. For the SIRT2 western blot standard curves, the net intensities from acetylated α-tubulin blots of known amounts of soluble brain extract were plotted and curve-fit according to a one phase, exponential decay, and the resulting coefficients of determination (R^2) were equal to 0.9999. For VDAC MD trajectory analyses, the mean from each simulation was considered a single experimental unit; therefore, where applicable, values are reported as the mean measurement from multiple simulations with standard error. Tadpole dose-response curves were generated by fitting a sigmoidal curve with variable slope to the equation:

$$y = \frac{100}{1 + (10^{\log EC50 - X})n}$$

where *n* is the Hill slope.

A2. Mass Spectra

A2.1 SIRT2 Peptides Photolabeled by AziPm

For all spectra, hypothetical fragment ions are listed in the tables, and their predicted positions are indicated on the spectra. Fragment ions that were identified on the spectra are colored in the ion tables. Only +1 fragment ions are shown. #Indicates a 216.0762 Da modification was detected; amino acid numbering is according to full-length rat SIRT2.

Peptide: ^{131}F.FALAKELY$^{\#}$PGQF.K^{144}

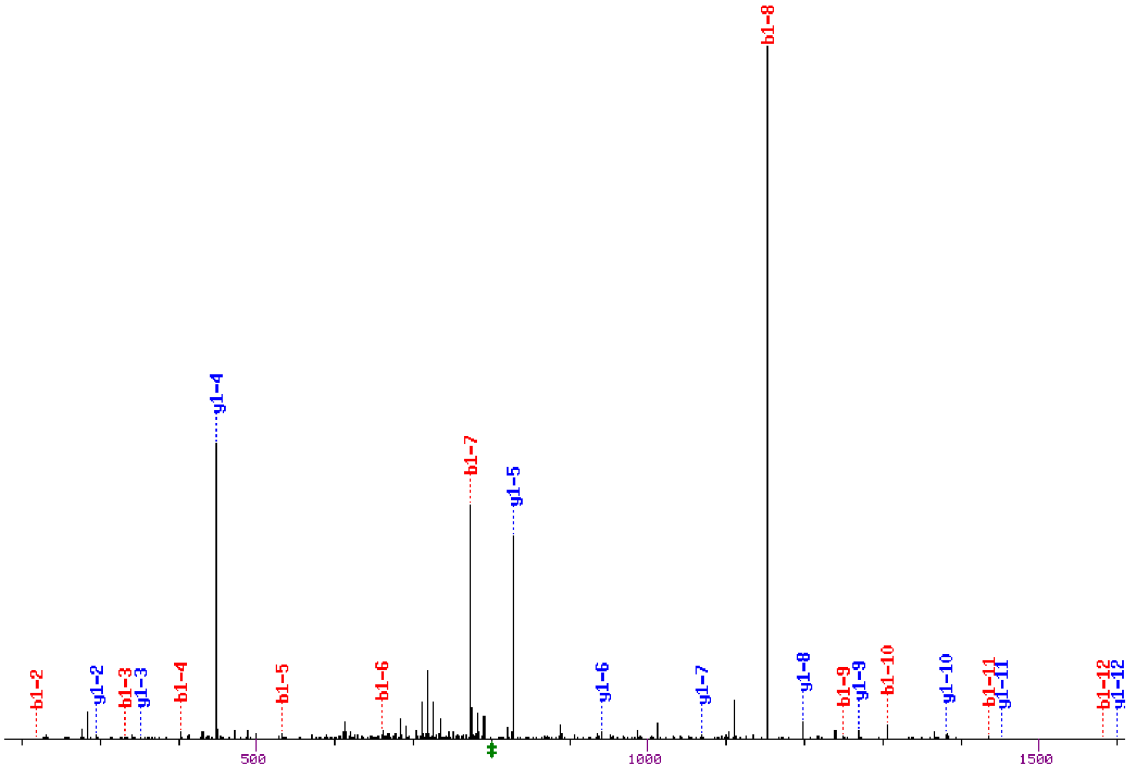

Sequence	#	b	y	#
F	1	148.1	1599.8	12
A	2	219.1	1452.7	11
L	3	332.2	1381.7	10
A	4	403.2	1268.6	9
K	5	531.3	1197.6	8
E	6	660.4	1069.5	7
L	7	773.5	940.4	6
Y#	8	1152.6	827.4	5
P	9	1249.6	448.2	4
G	10	1306.7	351.2	3
Q	11	1434.7	294.1	2
F	12	1581.8	166.1	1

Peptide: ^{132}F.ALAKELY$^{\#}$PGQF.K^{144}

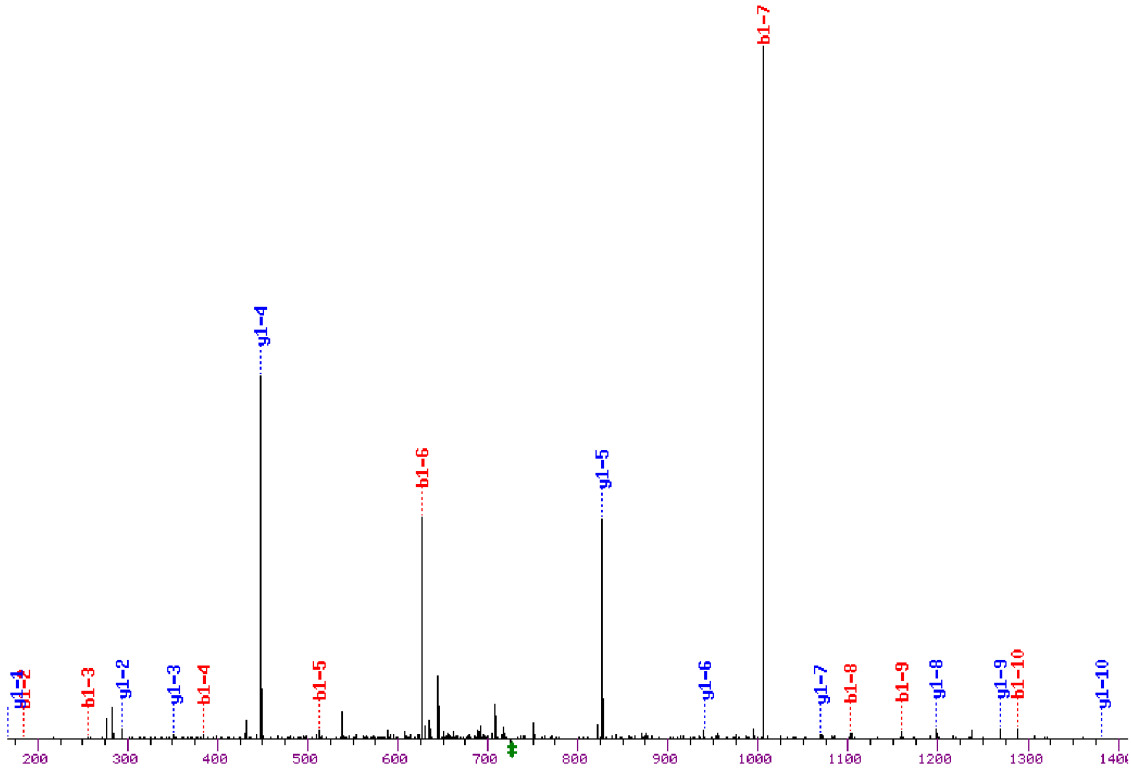

Sequence	#	b	y	#
A	1	72.0	1452.7	11
L	2	185.1	1381.7	10
A	3	256.2	1268.6	9
K	4	384.3	1197.6	8
E	5	513.3	1069.5	7
L	6	626.4	940.4	6
Y#	7	1005.5	827.4	5
P	8	1102.6	448.2	4
G	9	1159.6	351.2	3
Q	10	1287.7	294.1	2
F	11	1434.7	166.1	1

Peptide: ^{134}L.AKELY$^{\#}$PGQF.K^{144}

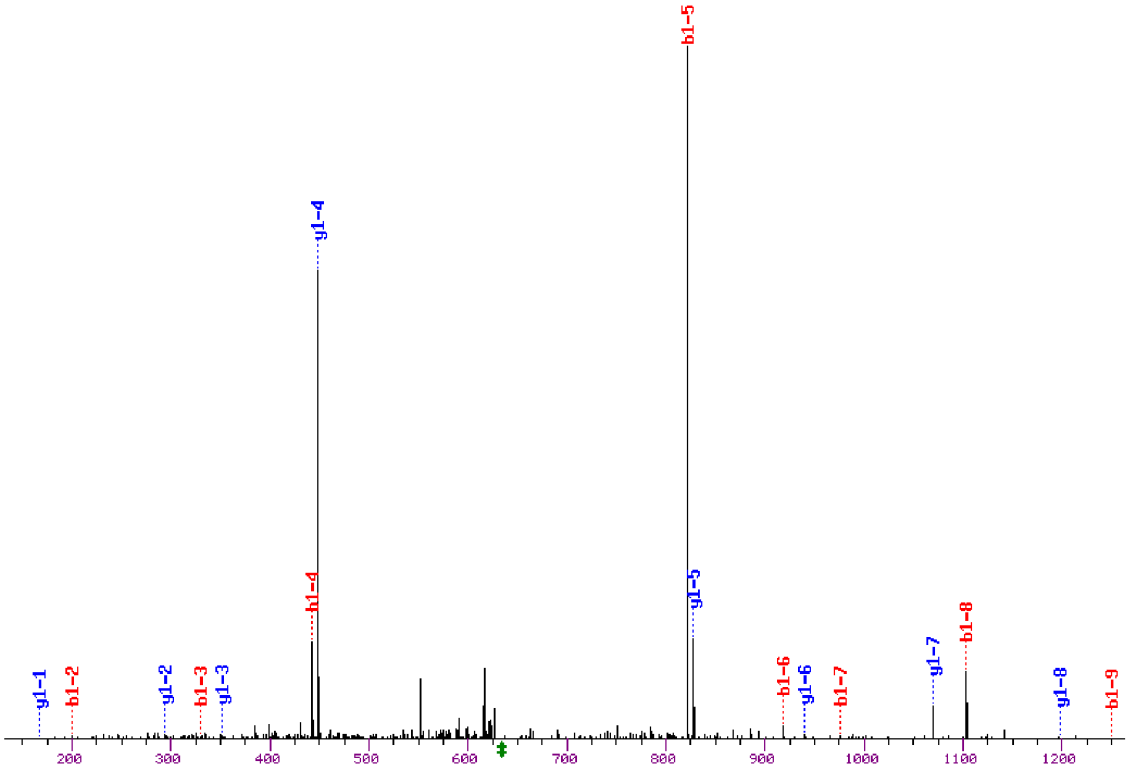

Sequence	#	b	y	#
A	1	72.0	1268.6	9
K	2	200.1	1197.6	8
E	3	329.2	1069.5	7
L	4	442.3	940.4	6
Y#	5	821.4	827.4	5
P	6	918.5	448.2	4
G	7	975.5	351.2	3
Q	8	1103.5	294.1	2
F	9	1250.6	166.1	1

Peptide: ^{136}K.ELY$^{\#}$PGQFK.P^{145}

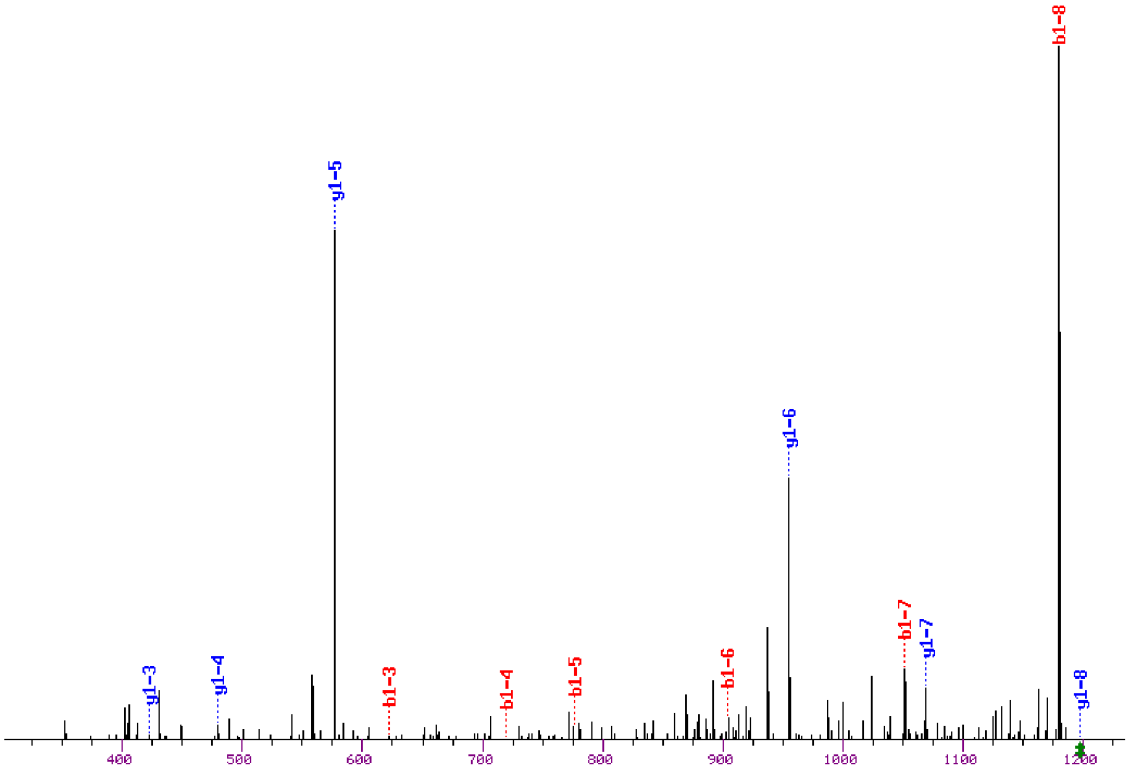

Sequence	#	b	y	#
E	1	130.1	1197.6	8
L	2	243.1	1068.5	7
Y#	3	622.3	955.5	6
P	4	719.3	576.3	5
G	5	776.3	479.3	4
Q	6	904.4	422.2	3
F	7	1051.5	294.2	2
K	8	1179.6	147.1	1

Peptide: ^{172}L.ERVAGLEPQDLVEAHGTF$^{\#}$Y.T^{192}

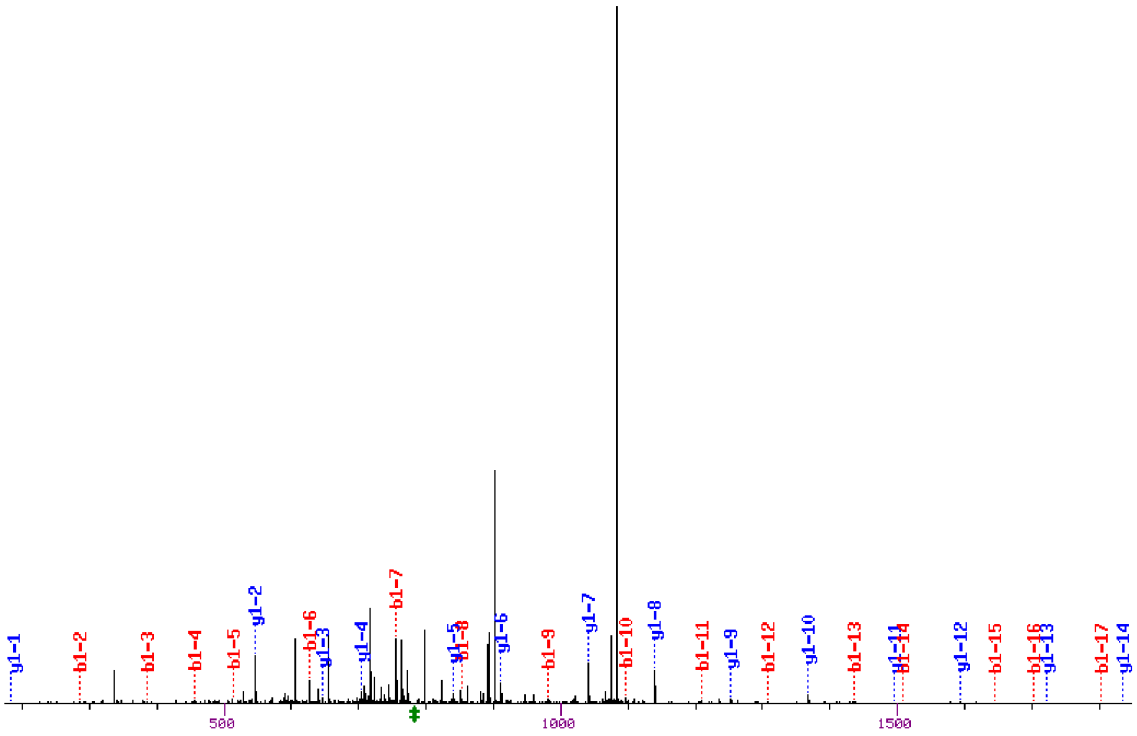

Sequence	#	b	y	#
E	1	130.1	2347.1	19
R	2	286.2	2218.1	18
V	3	385.2	2062.0	17
A	4	456.3	1962.9	16
G	5	513.3	1891.9	15
L	6	626.4	1834.9	14
E	7	755.4	1721.8	13
P	8	852.5	1592.7	12
Q	9	980.5	1495.7	11
D	10	1095.5	1367.6	10
L	11	1208.6	1252.6	9
V	12	1307.7	1139.5	8
E	13	1436.7	1040.4	7
A	14	1507.8	911.4	6
H	15	1644.8	840.4	5
G	16	1701.9	703.3	4
T	17	1802.9	646.3	3
F#	18	2166.0	545.2	2
Y	19	2329.2	182.0	1

note: the peaks at *m/z* = 902.0 and 1083.5 are b17 and b18 +2 fragment ions.

Peptide: ^{202}K.EYTM$^{\#}$SWMK.E^{211}

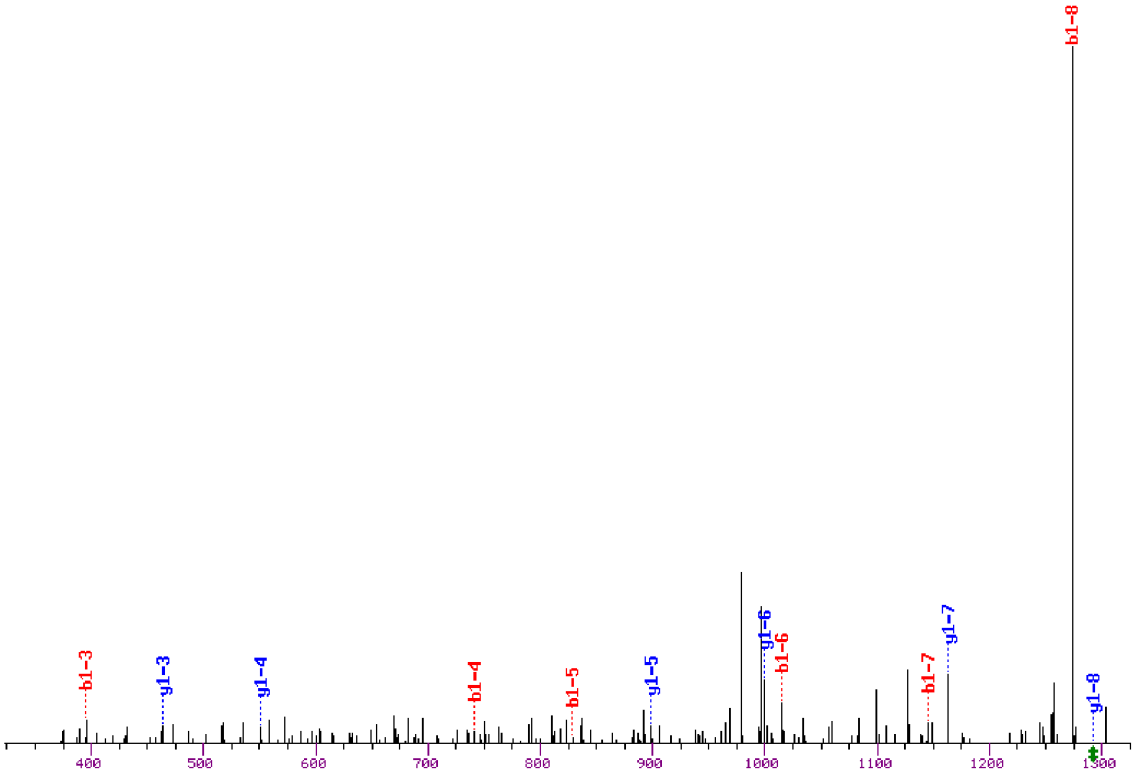

Sequence	#	b	y	#
E	1	130.1	1291.5	8
Y	2	293.1	1162.5	7
T	3	394.2	999.4	6
M#	4	741.3	898.4	5
S	5	828.3	551.3	4
W	6	1014.4	464.2	3
M	7	1145.4	278.2	2
K	8	1273.5	147.1	1

A2.2 VDAC Peptides Photolabeled by AziPm

Spectra of peptides that contain an AziP*m* adduct are shown below, along with the VDAC spot from which that spectra derived. Identified b and y ions are colored red and blue, respectively. Adducted residues are colored green. The value to the right of an identified ion corresponds to the delta mass (the deviation of the identified ion from the mass of the hypothetical value). Where applicable, # indicates the residue contained a +216.08 Da (AziP*m*) modification and * indicates a +15.99 (methionine oxidation) modification. +1 fragment ions are shown.

VDAC1 peptide, spot 1, trypsin digest

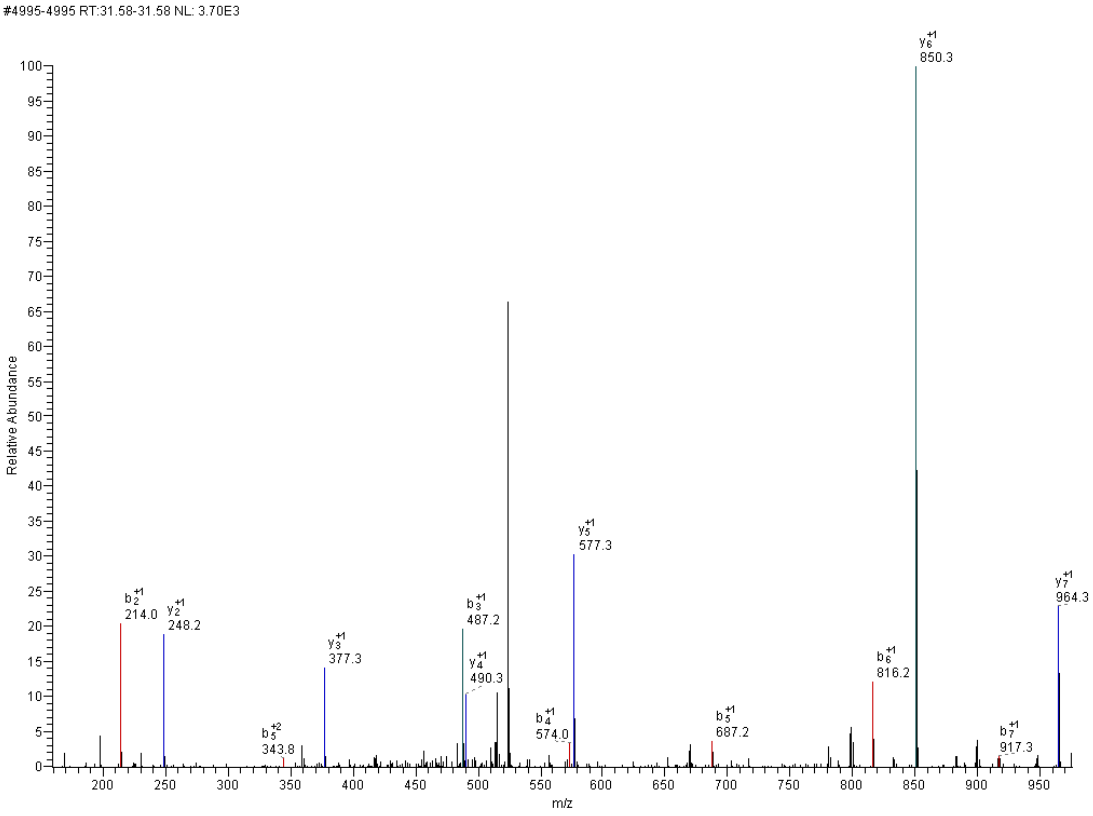

V	100.08		-	
N	214.12	0.13	964.46	0.19
G#	487.22	-0.01	850.42	0.13
S	574.25	0.27	577.32	0
L	687.33	0.14	490.29	-0.02
E	816.37	0.22	377.2	-0.13
T	917.42	0.14	248.16	0.01
K	-		147.11	

VDAC1 peptide, spot 1, trypsin digest

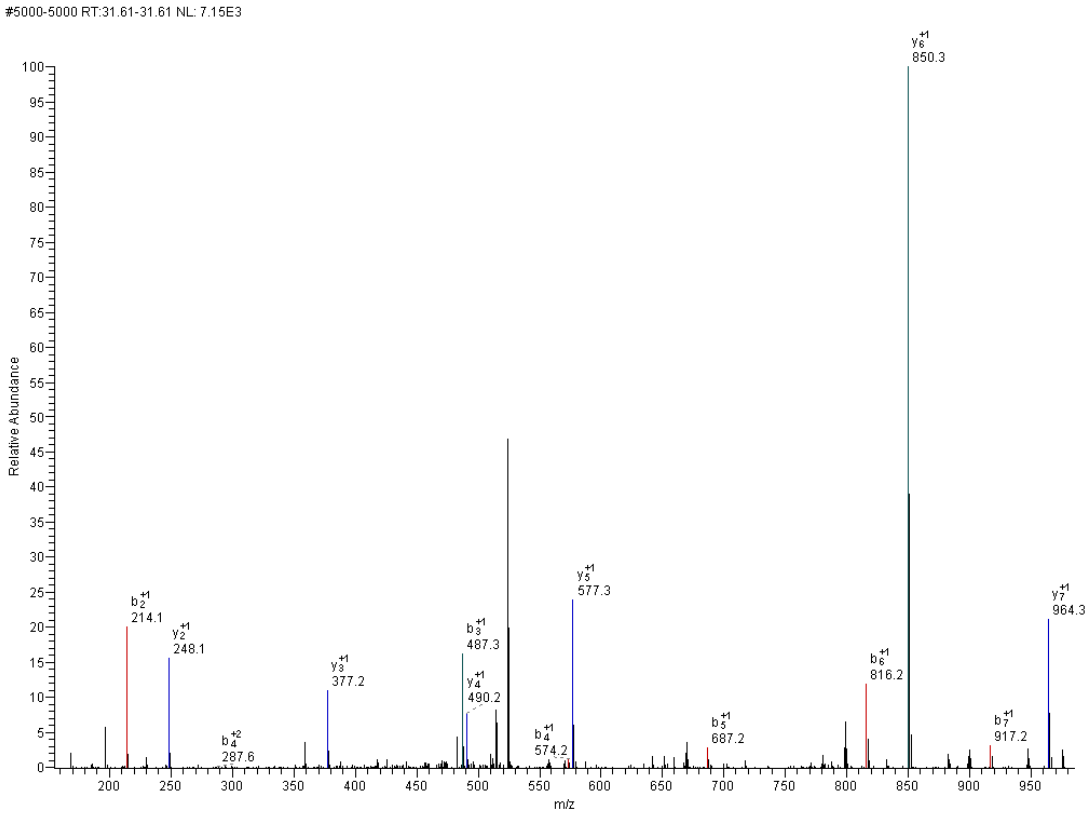

V	100.08		-	
N	214.12	0.06	964.46	0.17
G#	487.22	-0.06	850.42	0.11
S	574.25	0.03	577.32	-0.02
L	687.33	0.17	490.29	0.04
E	816.37	0.19	377.2	-0.01
T	917.42	0.24	248.16	0.04
K	-		147.11	

VDAC1 peptide, spot 2, trypsin digest

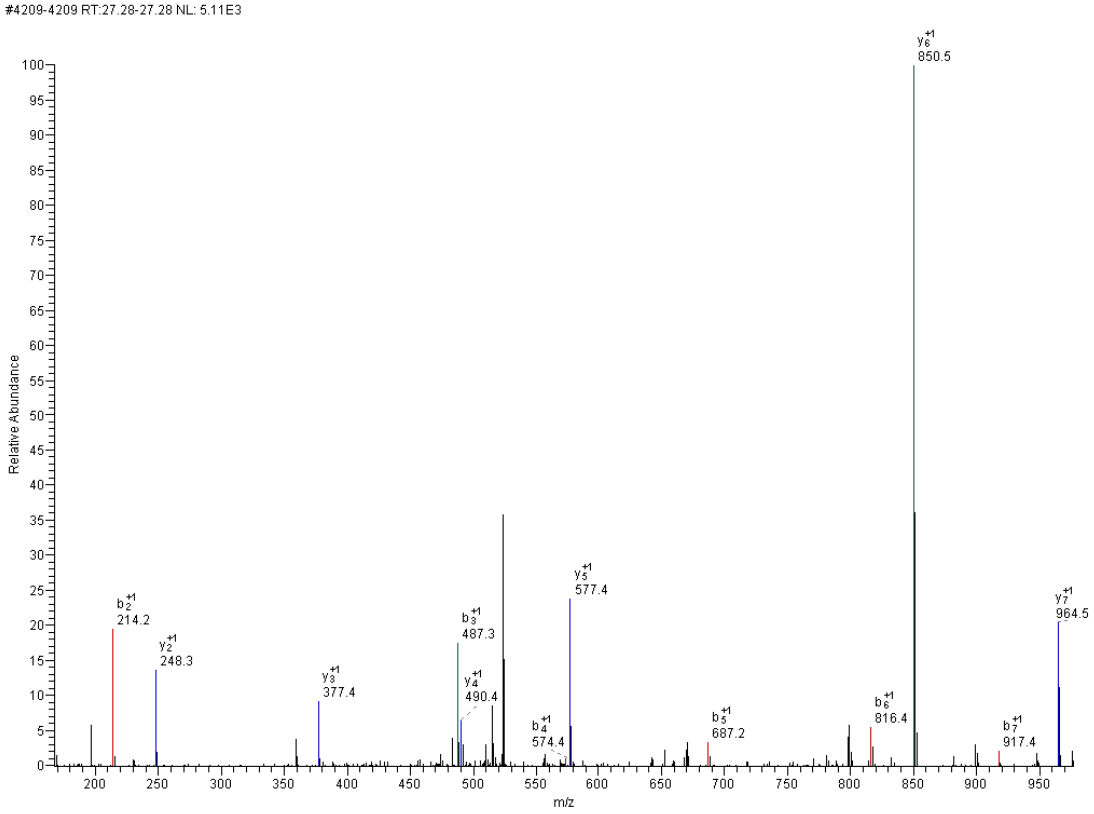

V	100.08		-	
N	214.12	-0.08	964.46	-0.03
G#	487.22	-0.07	850.42	-0.05
S	574.25	-0.10	577.32	-0.08
L	687.33	-0.14	490.29	-0.09
E	816.37	-0.02	377.2	-0.16
T	917.42	-0.05	248.16	-0.12
K	-		147.11	

VDAC1 peptide, spot 2, trypsin digest

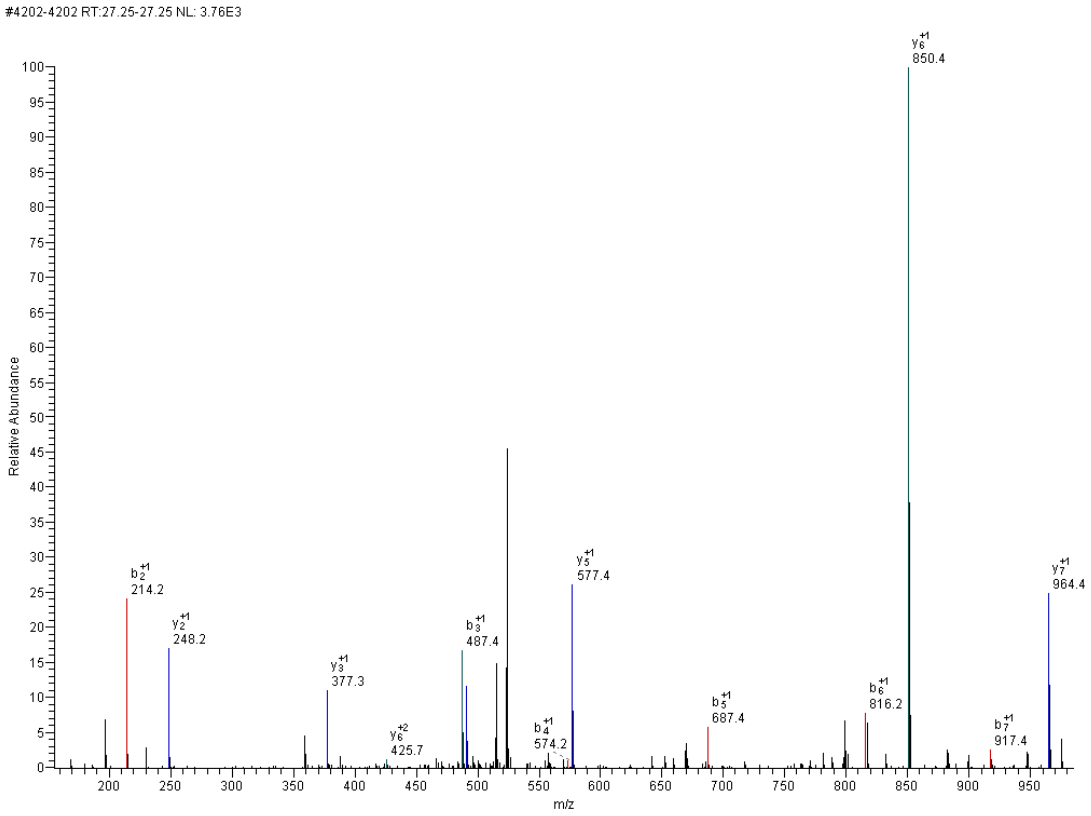

V	100.08		-	
N	214.12	-0.07	964.46	0.01
G#	487.22	-0.21	850.42	0.00
S	574.25	0.09	577.32	-0.11
L	687.33	-0.11	490.29	-0.05
E	816.37	0.19	377.20	-0.14
T	917.42	0.06	248.16	-0.07
K	-		147.11	

VDAC1 peptide, spot 3, trypsin digest

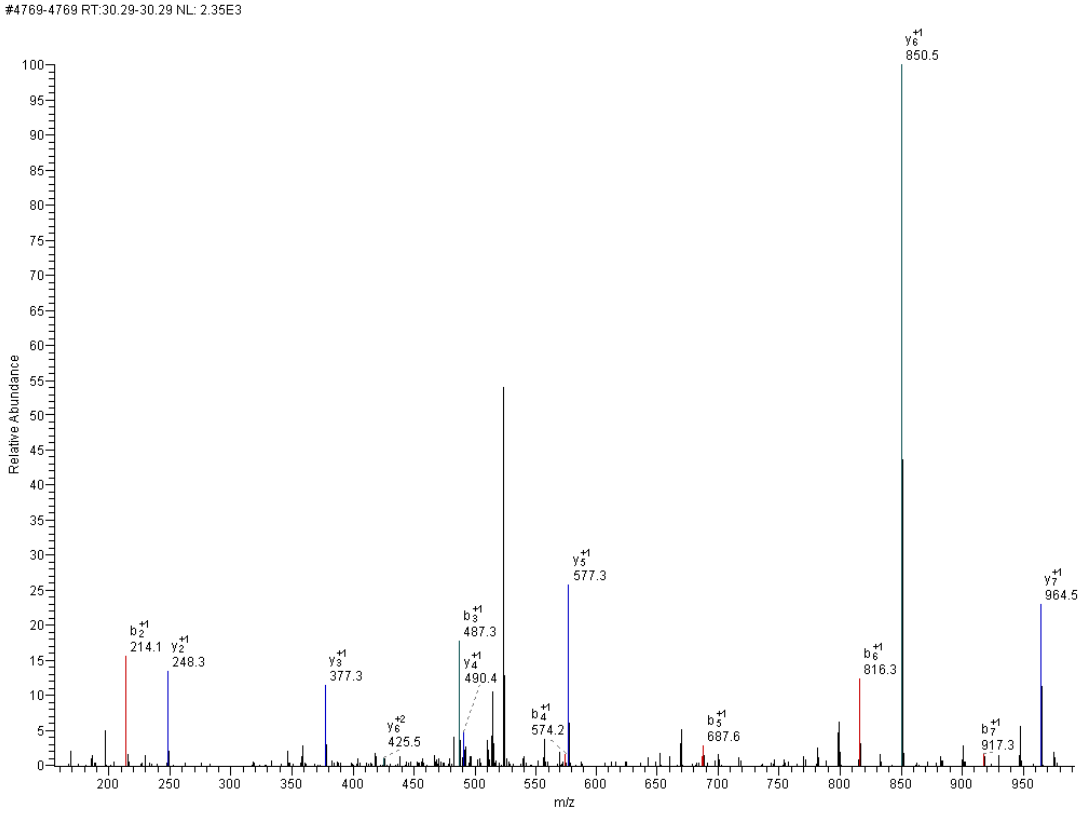

V	100.08		-	
N	214.12	-0.02	964.46	-0.06
G#	487.22	-0.1	850.42	-0.05
S	574.25	0.01	577.32	0
L	687.33	-0.27	490.29	-0.13
E	816.37	0.06	377.20	-0.06
T	917.42	0.15	248.16	-0.14
K		-	147.11	

VDAC1 peptide, spot 4, trypsin digest

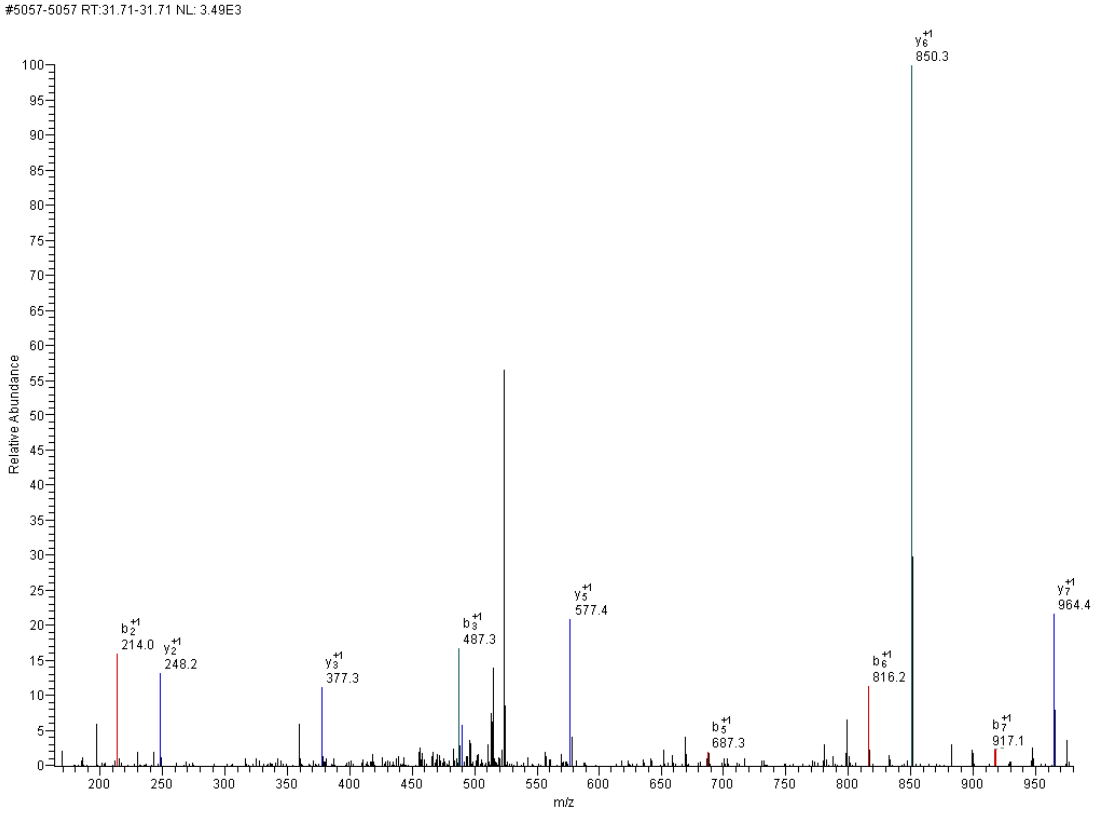

V	100.08		-	
N	214.12	0.11	964.46	0.08
G#	487.22	-0.1	850.42	0.07
S	574.25		577.32	-0.06
L	687.33	0.03	490.29	0.08
E	816.37	0.22	377.2	-0.09
T	917.42	0.36	248.16	0.01
K	-		147.11	

VDAC1 peptide, spot 5, trypsin digest

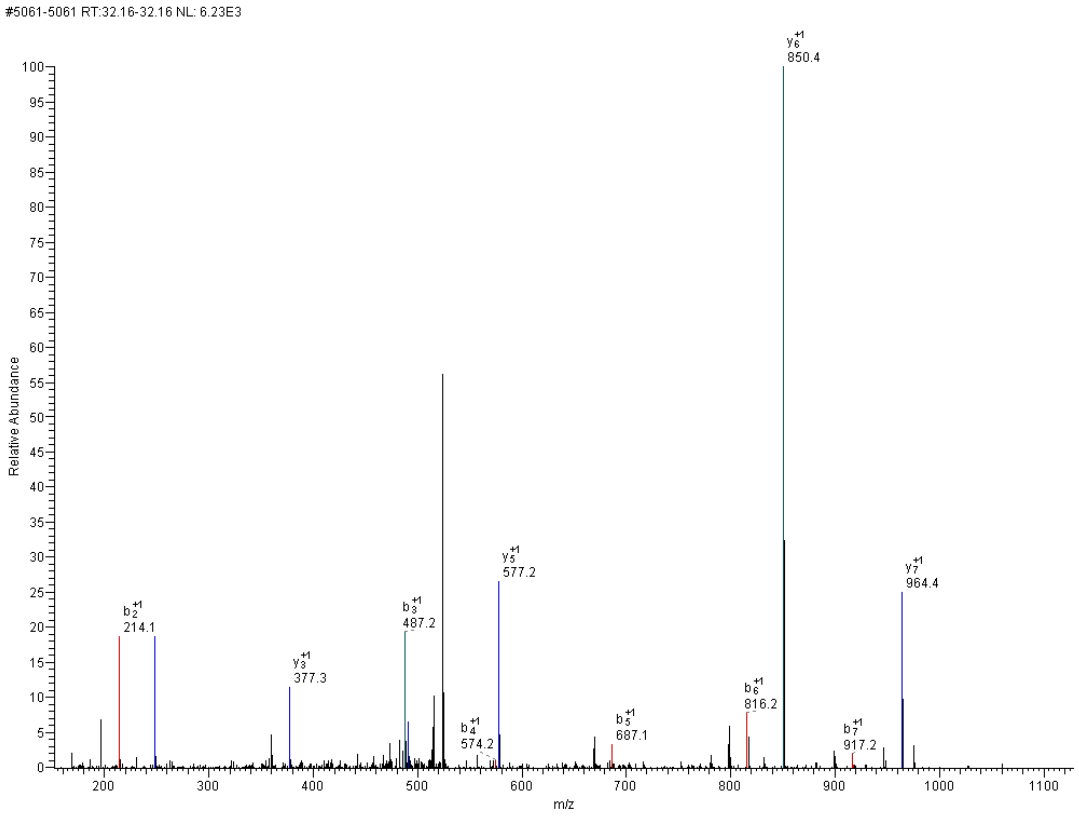

V	100.08		-	
N	214.12	0.06	964.46	0.09
G#	487.22	0.02	850.42	0.03
S	574.25	0.07	577.32	0.1
L	687.33	0.23	490.29	-0.05
E	816.37	0.18	377.2	-0.07
T	917.42	0.26	248.16	0.02
K	-		147.11	

VDAC1 peptide, spot 2, chymotrypsin digest

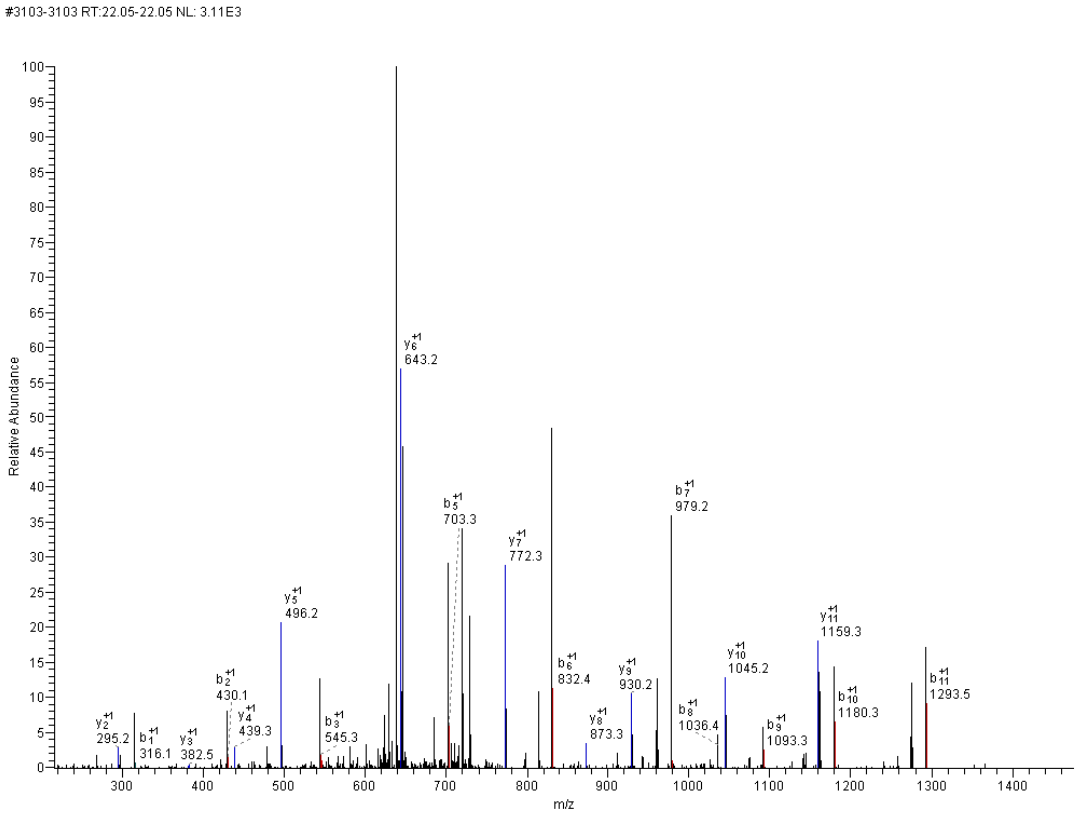

V#	316.15	0.03	-	
N	430.19	0.06	1159.49	0.22
D	545.22	-0.11	1045.45	0.20
G	602.24		930.42	0.25
T	703.29	0.03	873.4	0.15
E	832.33	-0.02	772.35	0.09
F	979.40	0.22	643.31	0.06
G	1036.42	0.05	496.24	0.04
G	1093.44	0.11	439.22	-0.04
S	1180.48	0.13	382.2	-0.30
I	1293.56	0.09	295.17	-0.05
Y	-		182.08	

VDAC1 peptide, spot 2, chymotrypsin digest

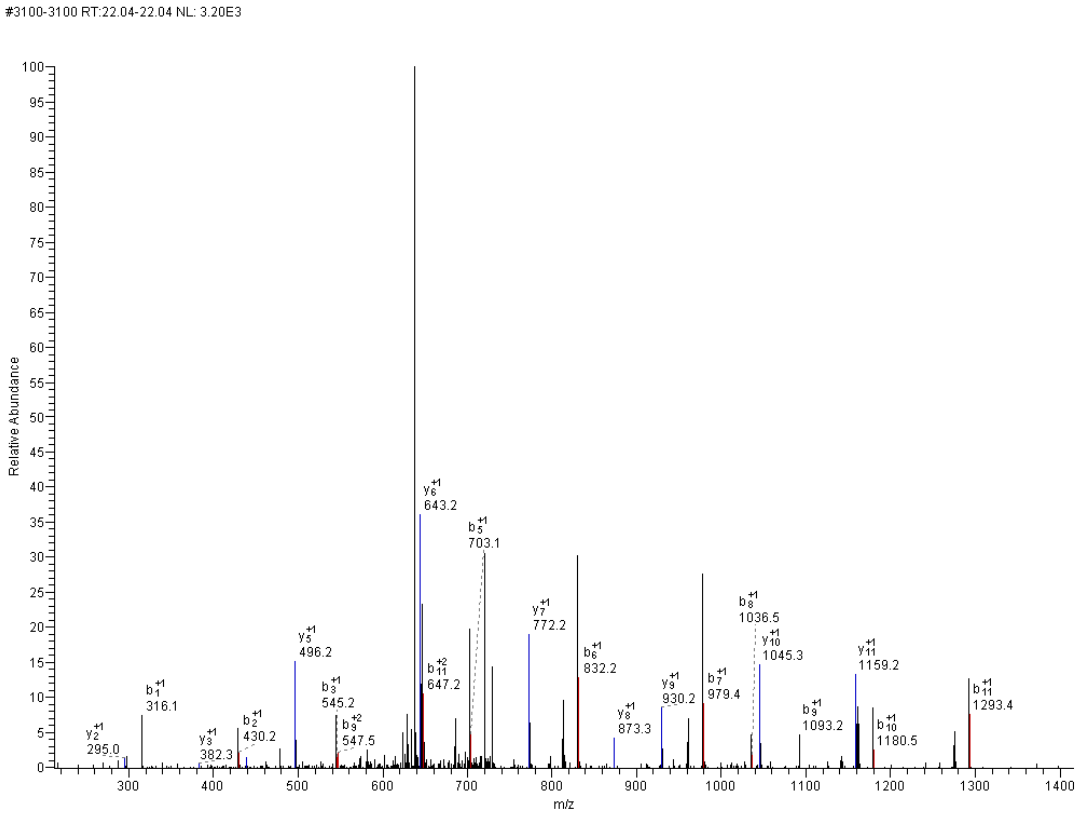

V#	316.15	0.08	-	
N	430.19	-0.01	1159.49	0.28
D	545.22	-0.02	1045.45	0.17
G	602.24		930.42	0.24
T	703.29	0.15	873.40	0.07
E	832.33	0.08	772.35	0.16
F	979.40	0.05	643.31	0.07
G	1036.42	-0.06	496.24	0.03
G	1093.44	0.24	439.22	-0.03
S	1180.48	0.02	382.20	-0.05
I	1293.56	0.20	295.17	0.18
Y	-		182.08	

VDAC2 peptide, spot 2, chymotrypsin digest

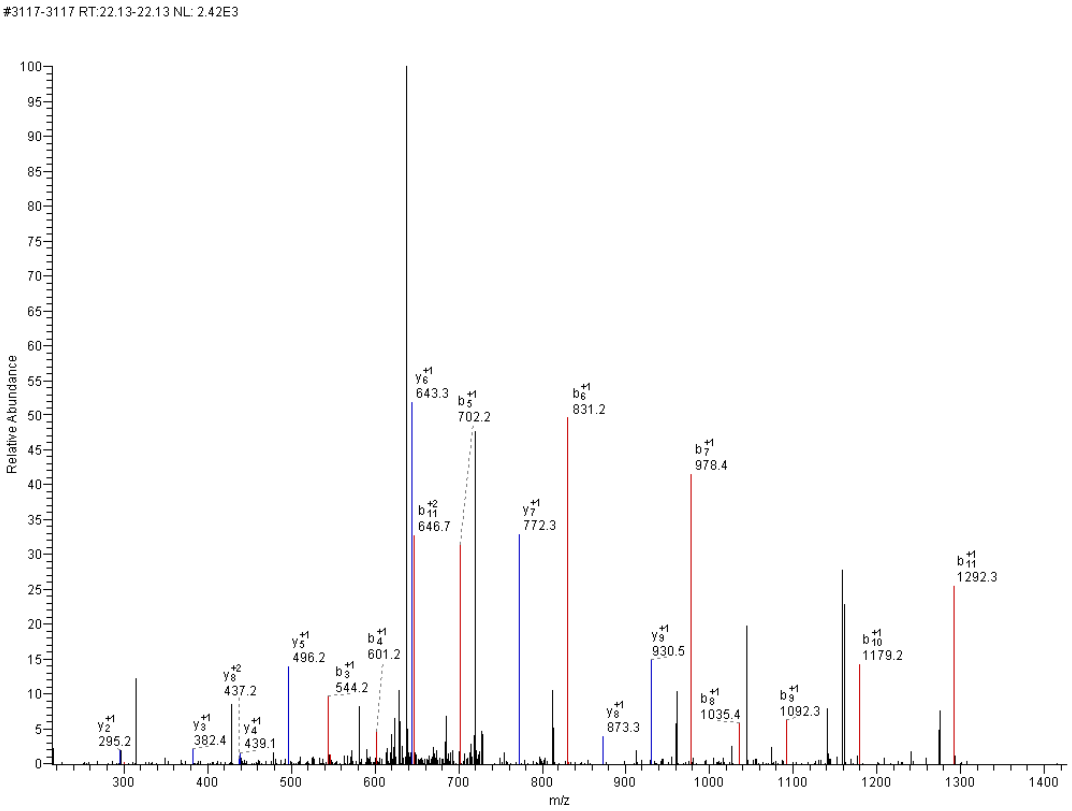

V#	316.15		-	
N	430.19		1158.51	
N	544.24	-0.01	1044.46	
G	601.26	0.11	930.42	-0.05
T	702.31	0.08	873.40	0.14
E	831.35	0.20	772.35	0.07
F	978.42	0.07	643.31	-0.02
G	1035.44	0.08	496.24	0.06
G	1092.46	0.11	439.22	0.09
S	1179.49	0.32	382.20	-0.20
I	1292.58	0.27	295.17	-0.06
Y	-		182.08	

VDAC2 peptide, spot 2, chymotrypsin digest

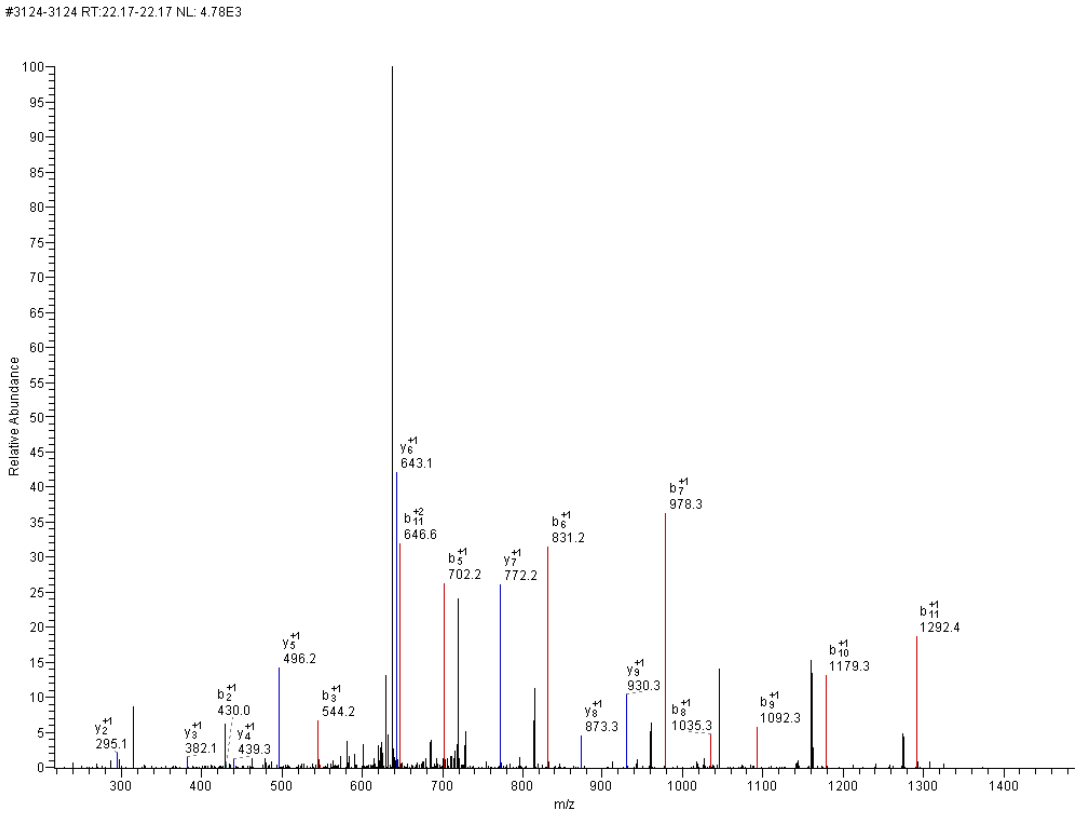

V#	316.15		-	
N	430.19	0.23	1158.51	
N	544.24	-0.01	1044.46	
G	601.26		930.42	0.15
T	702.31	0.08	873.40	0.07
E	831.35	0.13	772.35	0.13
F	978.42	0.16	643.31	0.18
G	1035.44	0.19	496.24	0.04
G	1092.46	0.19	439.22	-0.08
S	1179.49	0.22	382.20	0.13
I	1292.58	0.14	295.17	0.11
Y	-		182.08	

A2.3 Tubulin Peptides Photolabeled by 1-AZA

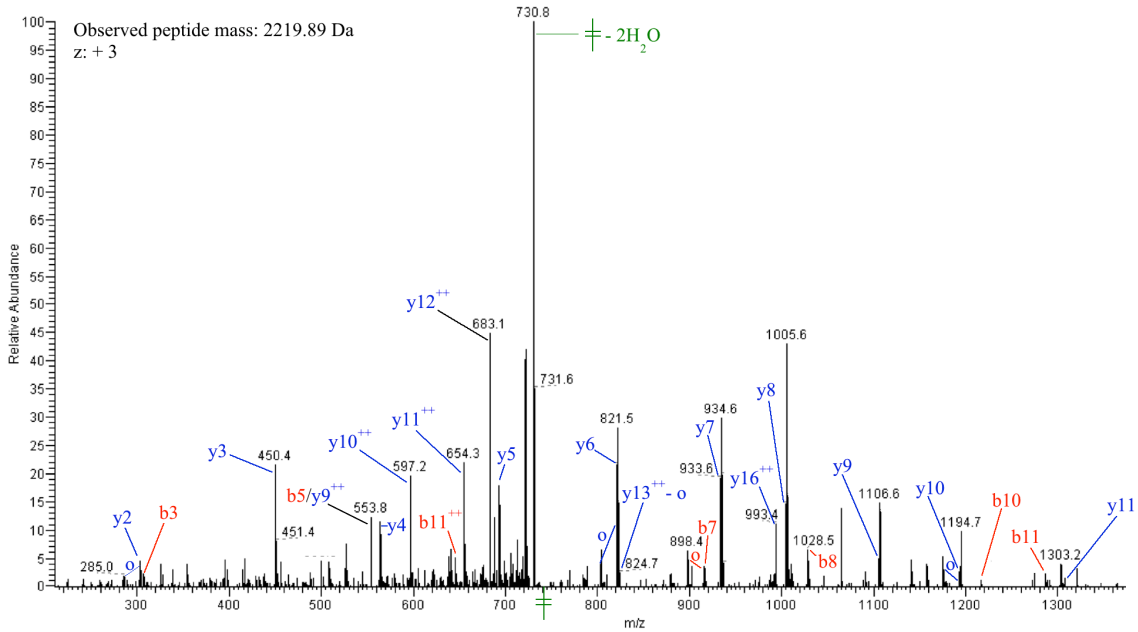

		m/z		m/z
M^{ox}	b1	148.0	y18	2222.3
S	b2	235.1	y17	2074.3
A	b3	306.1	y16	1987.2
T	b4	407.2	y15	1916.2
F	b5	554.3	y14	1815.1
I^{AZA}	b6	858.6	y13	1668.0
G	b7	915.6	y12	1363.7
N	b8	1029.6	y11	1306.7
S	b9	1116.6	y10	1192.7
T	b10	1217.7	y9	1105.7
A	b11	1288.7	y8	1004.6
I	b12	1401.8	y7	933.6
Q	b13	1529.9	y6	820.5
E	b14	1658.9	y5	692.4
L	b15	1772.0	y4	563.4
F	b16	1919.1	y3	450.3
K	b17	2047.2	y2	303.2
R	b18	2222.3	y1	175.1

tubulin β-2b/c

$M^{ox}SATFI^{AZA}GNSTAIQELFKR$

		m/z		m/z
M	b1	132.0	y18	2222.3
S	b2	219.1	y17	2090.2
S	b3	306.1	y16	2003.2
T	b4	407.2	y15	1916.2
F	b5	554.2	y14	1815.1
I^{AZA}	b6	858.6	y13	1668.1
G	b7	915.6	y12	1363.7
N	b8	1029.6	y11	1306.7
S	b9	1116.6	y10	1192.7
T	b10	1217.7	y9	1105.7
A	b11	1288.7	y8	1004.6
I	b12	1401.8	y7	933.6
Q	b13	1529.9	y6	820.5
E	b14	1658.9	y5	692.4
L	b15	1772.0	y4	563.4
F	b16	1919.1	y3	450.3
K	b17	2047.2	y2	303.2
R	b18	2222.3	y1	175.1

tubulin β-3

$MSSTFI^{AZA}GNSTAIQELFKR$

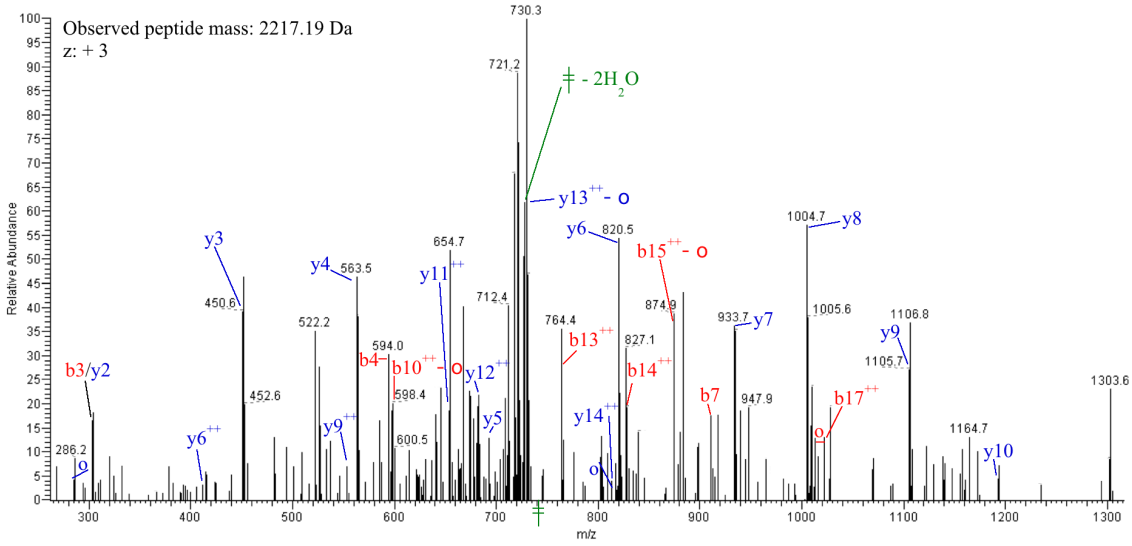

		m/z		m/z
M	b1	132.0	y18	2218.3
A	b2	203.1	y17	2086.3
V	b3	302.2	y16	2015.2
T^{AZA}	b4	594.5	y15	1916.2
F	b5	741.6	y14	1623.9
I	b6	854.6	y13	1476.8
G	b7	911.7	y12	1363.7
N	b8	1025.7	y11	1306.7
S	b9	1112.7	y10	1192.7
T	b10	1213.8	y9	1105.6
A	b11	1284.8	y8	1004.6
I	b12	1397.9	y7	933.6
Q	b13	1526.0	y6	820.5
E	b14	1655.0	y5	692.4
L	b15	1768.1	y4	563.4
F	b16	1915.2	y3	450.3
K	b17	2043.2	y2	303.2
R	b18	2218.3	y1	175.1

tublin β−5

$MAVT^{AZA}FIGNSTAIQELFKR$

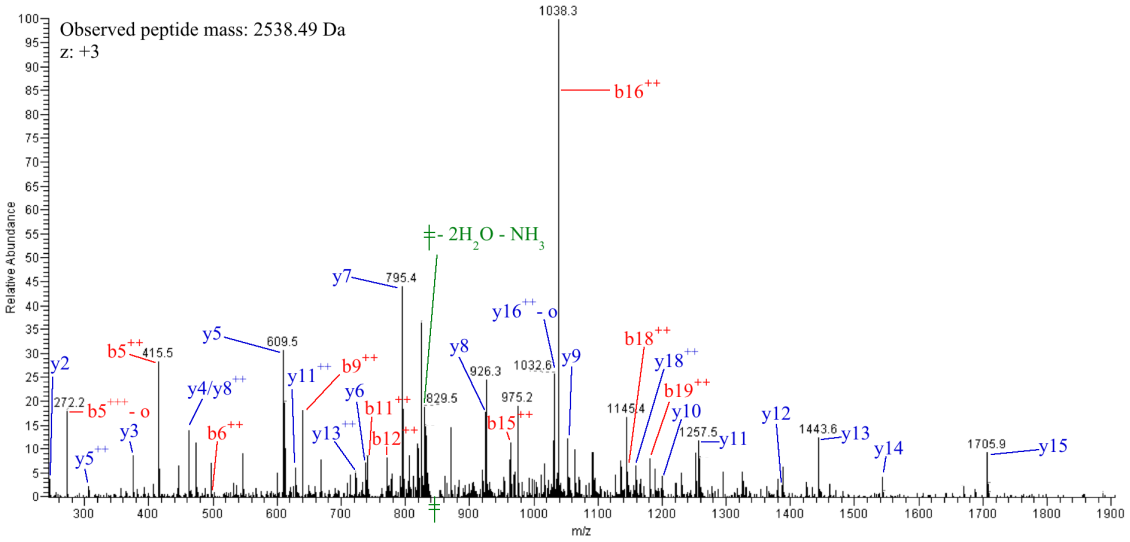

		m/z		m/z
A	b1	72.0	y20	2538.3
F	b2	219.1	y19	2466.2
V	b3	318.2	y18	2319.1
H	b4	455.2	y17	2220.1
W^{AZA}	b5	832.5	y16	2083.0
Y	b6	995.6	y15	1705.7
V	b7	1094.7	y14	1542.6
G	b8	1151.7	y13	1443.6
E	b9	1280.7	y12	1386.5
G	b10	1331.7	y11	1257.5
M^{ox}	b11	1484.8	y10	1200.5
E	b12	1613.8	y9	1053.4
E	b13	1742.9	y8	924.4
G	b14	1799.9	y7	795.4
E	b15	1928.9	y6	738.3
F	b16	2076.0	y5	609.3
S	b17	2163.0	y4	462.3
E	b18	2292.1	y3	375.2
A	b19	2363.1	y2	246.2
R	b20	2538.3	y1	175.1

tubulin α-1d

$AFVHW^{AZA}YVGEGM^{ox}EEGEFSEAR$

A3. Acknowledgement of Funding Sources

This work was supported in part by the National Institutes of Health, including through grants F31-NS080519, P01-GM055876, and T32-GM008076. Additional support was provided by the Department of Anesthesiology & Critical Care of the University of Pennsylvania, and also by the Solomon and Catherine Erulkar Traveling Fellowship Award.

BIBLIOGRAPHY

Addona GH, Husain SS, Stehle T, and Miller KW (2002) Geometric isomers of a photoactivable general anesthetic delineate a binding site on adenylate kinase. *J Biol Chem* **277**:25685–25691.

Aksimentiev A, and Schulten K (2005) Imaging alpha-hemolysin with molecular dynamics: ionic conductance, osmotic permeability, and the electrostatic potential map. *Biophys J* **88**:3745–3761.

Amodeo GF, Scorciapino MA, Messina A, De Pinto V, and Ceccarelli M (2014) Charged residues distribution modulates selectivity of the open state of human isoforms of the voltage dependent anion-selective channel. *PloS ONE* **9**:e103879.

Arcario MJ, Mayne CG, and Tajkhorshid E (2014) Atomistic models of general anesthetics for use in in silico biological studies. *J Phys Chem B* **118**:12075–12086.

Arnold K, Bordoli L, Kopp J, and Schwede T (2006) The SWISS-MODEL workspace: a web-based environment for protein structure homology modelling. *Bioinforma Oxf Engl* **22**:195–201.

Avalos JL, Bever KM, and Wolberger C (2005) Mechanism of sirtuin inhibition by nicotinamide: altering the NAD(+) cosubstrate specificity of a Sir2 enzyme. *Mol Cell* **17**:855–868.

Avalos JL, Boeke JD, and Wolberger C (2004) Structural basis for the mechanism and regulation of Sir2 enzymes. *Mol Cell* **13**:639–648.

Avalos JL, Celic I, Muhammad S, Cosgrove MS, Boeke JD, and Wolberger C (2002) Structure of a Sir2 enzyme bound to an acetylated p53 peptide. *Mol Cell* **10**:523–535.

Aveldaño MI, and Horrocks LA (1983) Quantitative release of fatty acids from lipids by a simple hydrolysis procedure. *J Lipid Res* **24**:1101–1105.

Azoulay-Zohar H, Israelson A, Abu-Hamad S, and Shoshan-Barmatz V (2004) In self-defence: hexokinase promotes voltage-dependent anion channel closure and prevents mitochondria-mediated apoptotic cell death. *Biochem J* **377**:347–355.

Baggetto LG, Clottes E, and Vial C (1992) Low mitochondrial proton leak due to high membrane cholesterol content and cytosolic creatine kinase as two features of the deviant bioenergetics of Ehrlich and AS30-D tumor cells. *Cancer Res* **52**:4935–4941.

Bahri MA, Seret A, Hans P, Piette J, Deby-Dupont G, and Hoebeke M (2007) Does propofol alter membrane fluidity at clinically relevant concentrations? An ESR spin label study. *Biophys Chem* **129**:82–91.

Ballatore C, Brunden KR, Huryn DM, Trojanowski JQ, Lee VM, and Smith AB 3rd (2012) Microtubule stabilizing agents as potential treatment for Alzheimer's disease and related neurodegenerative tauopathies. *J Med Chem* **55**:8979-8996.

Baxter International Inc. (2013) Sevoflurane Product Monograph.

Bayrhuber M, Meins T, Habeck M, Becker S, Giller K, Villinger S, Vonrhein C, Griesinger C, Zweckstetter M, and Zeth K (2008) Structure of the human voltage-dependent anion channel. *Proc Natl Acad Sci U S A* **105**:15370–15375.

Beglov D, and Roux B (1994) Finite representation of an infinite bulk system: Solvent boundary potential for computer simulations. *J Chem Phys* **100**:9050–9063.

Beirowski B, Gustin J, Armour SM, Yamamoto H, Viader A, North BJ, Michán S, Baloh RH, Golden JP, Schmidt RE, Sinclair DA, Auwerx J, and Milbrandt J (2011) Sir-two-homolog 2 (Sirt2) modulates peripheral myelination through polarity protein Par-3/atypical protein kinase C (aPKC) signaling. *Proc Natl Acad Sci U S A* **108**:E952–961.

Best RB, Zhu X, Shim J, Lopes PEM, Mittal J, Feig M, and Mackerell AD Jr (2012) Optimization of the additive CHARMM all-atom protein force field targeting improved sampling of the backbone φ, ψ and side-chain χ(1) and χ(2) dihedral angles. *J Chem Theory Comput* **8**:3257–3273.

Bhattacharya AA, Curry S, and Franks NP (2000) Binding of the general anesthetics propofol and halothane to human serum albumin. High resolution crystal structures. *J Biol Chem* **275**:38731–38738.

Biasini M, Bienert S, Waterhouse A, Arnold K, Studer G, Schmidt T, Kiefer F, Cassarino TG, Bertoni M, Bordoli L, and Schwede T (2014) SWISS-MODEL: modelling protein tertiary and quaternary structure using evolutionary information. *Nucleic Acids Res* **42**:W252-258.

Blachly-Dyson E, Peng S, Colombini M, and Forte M (1990) Selectivity changes in site-directed mutants of the VDAC ion channel: structural implications. *Science* **247**:1233–1236.

Blackmer T, Larsen EC, Bartleson C, Kowalchyk JA, Yoon E-J, Preininger AM, Alford S, Hamm HE, and Martin TFJ (2005) G protein βγ directly regulates SNARE protein fusion machinery for secretory granule exocytosis. *Nat Neurosci* **8**:421-425.

Borra MT, Langer MR, Slama JT, and Denu JM (2004) Substrate specificity and kinetic mechanism of the Sir2 family of NAD+-dependent histone/protein deacetylases. *Biochemistry* **43**:9877–9887.

Bösterling B, Trevor A, and Trudell JR (1982) Binding of halothane-free radicals to fatty acids following UV irradiation. *Anesthesiology* **56**:380–384.

Bowery NG, Hudson AL, and Price GW (1987) GABAA and GABAB receptor site distribution in the rat central nervous system. *Neuroscience* **20**:365–383.

Bright DP, Adham SD, Lemaire LCJM, Benavides R, Gruss M, Taylor GW, Smith EH, and Franks NP (2007) Identification of anesthetic binding sites on human serum albumin using a novel etomidate photolabel. *J Biol Chem* **282**:12038–12047.

Brunden KR, Ballatore C, Lee VM-Y, Smith AB, and Trojanowski JQ (2012) Brain-penetrant microtubule-stabilizing compounds as potential therapeutic agents for tauopathies. *Biochem Soc Trans* **40**:661–666.

Bureau MH, Khrestchatisky M, Heeren MA, Zambrowicz EB, Kim H, Grisar TM, Colombini M, Tobin AJ, and Olsen RW (1992) Isolation and cloning of a voltage-

dependent anion channel-like Mr 36,000 polypeptide from mammalian brain. *J Biol Chem* **267**:8679–8684.

Butts CA, Xi J, Brannigan G, Saad AA, Venkatachalan SP, Pearce RA, Klein ML, Eckenhoff RG, and Dmochowski IJ (2009) Identification of a fluorescent general anesthetic, 1-aminoanthracene. *Proc Natl Acad Sci U S A* **106**:6501–6506.

Cheng B, and Kimura T (1983) The distribution of cholesterol and phospholipid composition in submitochondrial membranes from bovine adrenal cortex: fundamental studies of steroidogenic mitochondria. *Lipids* **18**:577–584.

Cheng T, Zhao Y, Li X, Lin F, Xu Y, Zhang X, Li Y, Wang R, and Lai L (2007) Computation of octanol-water partition coefficients by guiding an additive model with knowledge. *J Chem Inf Model* **47**:2140–2148.

Chen Z-W, Chen L-H, Akentieva N, Lichti CF, Darbandi R, Hastings R, Covey DF, Reichert DE, Townsend RR, and Evers AS (2012) A neurosteroid analogue photolabeling reagent labels the colchicine-binding site on tubulin: A mass spectrometric analysis. *Electrophoresis* **33**:666–674.

Chen Z-W, Manion B, Townsend RR, Reichert DE, Covey DF, Steinbach JH, Sieghart W, Fuchs K, and Evers AS (2012) Neurosteroid analog photolabeling of a site in the third transmembrane domain of the β3 subunit of the GABA(A) receptor. *Mol Pharmacol* **82**:408–419.

Chiara DC, Dangott LJ, Eckenhoff RG, and Cohen JB (2003) Identification of nicotinic acetylcholine receptor amino acids photolabeled by the volatile anesthetic halothane. *Biochemistry* **42**:13457–13467.

Chiara DC, Gill JF, Chen Q, Tillman T, Dailey WP, Eckenhoff RG, Xu Y, Tang P, and Cohen JB (2014) Photoaffinity labeling the propofol binding site in GLIC. *Biochemistry* **53**:135–142.

Colbeau A, Nachbaur J, and Vignais PM (1971) Enzymic characterization and lipid composition of rat liver subcellular membranes. *Biochim Biophys Acta* **249**:462–492.

Colombini M (1979) A candidate for the permeability pathway of the outer mitochondrial membrane. *Nature* **279**:643–645.

Colombini M (1980) Pore size and properties of channels from mitochondria isolated from Neurospora crassa. *J Membr Biol* **53**:79–84.

Colombini M (2009) The published 3D structure of the VDAC channel: native or not? *Trends Biochem Sci* **34**:382–389.

Colombini M (2004) VDAC: The channel at the interface between mitochondria and the cytosol. *Mol Cell Biochem* **256-257**:107–115.

Colombini M (1989) Voltage gating in the mitochondrial channel, VDAC. *J Membr Biol* **111**:103–111.

Colombini M, Blachly-Dyson E, and Forte M (1996) VDAC, a channel in the outer mitochondrial membrane. *Ion Channels* **4**:169–202.

Condliffe SB, Corradini I, Pozzi D, Verderio C, and Matteoli M (2010) Endogenous SNAP-25 regulates native voltage-gated calcium channels in glutamatergic neurons. *J Biol Chem* **285**:24968–24976.

Craddock TJA, St George M, Freedman H, Barakat KH, Damaraju S, Hameroff S, and Tuszynski JA (2012) Computational predictions of volatile anesthetic interactions with the microtubule cytoskeleton: implications for side effects of general anesthesia. *PloS ONE* **7**:e37251.

Creeley C, Dikranian K, Dissen G, Martin L, Olney J, and Brambrink A (2013) Propofol-induced apoptosis of neurones and oligodendrocytes in fetal and neonatal rhesus macaque brain. *Br J Anaesth* **110 Suppl 1**:i29–38.

Darbandi-Tonkabon R, Hastings WR, Zeng C-M, Akk G, Manion BD, Bracamontes JR, Steinbach JH, Mennerick SJ, Covey DF, and Evers AS (2003) Photoaffinity labeling with a neuroactive steroid analogue. 6-azi-pregnanolone labels voltage-dependent anion channel-1 in rat brain. *J Biol Chem* **278**:13196–13206.

Darbandi-Tonkabon R, Manion BD, Hastings WR, Craigen WJ, Akk G, Bracamontes JR, He Y, Sheiko TV, Steinbach JH, Mennerick SJ, Covey DF, and Evers AS (2004)

Neuroactive steroid interactions with voltage-dependent anion channels: lack of relationship to GABAA receptor modulation and anesthesia. *J Pharmacol Exp Ther* **308**:502–511.

De Frémont P, Marion N, and Nolan SP (2009) Carbenes: Synthesis, properties, and organometallic chemistry. *Coord Chem Rev* **253**:862–892.

De Pinto V, Benz R, and Palmieri F (1989) Interaction of non-classical detergents with the mitochondrial porin. *Eur J Biochem* **183**:179–187.

Domingo A (1990) Exponential gradient maker using a disposable syringe. *Anal Biochem* **189**:88–90.

Downes H, and Courogen PM (1996) Contrasting effects of anesthetics in tadpole bioassays. *J Pharmacol Exp Ther* **278**:284–296.

Dunkley PR, Jarvie PE, and Robinson PJ (2008) A rapid Percoll gradient procedure for preparation of synaptosomes. *Nat Protoc* **3**:1718–1728.

Eckenhoff MF, Chan K, and Eckenhoff RG (2002) Multiple specific binding targets for inhaled anesthetics in the mammalian brain. *J Pharmacol Exp Ther* **300**:172–179.

Eckenhoff MF, and Eckenhoff RG (1998) Quantitative autoradiography of halothane binding in rat brain. *J Pharmacol Exp Ther* **285**:371–376.

Eckenhoff RG (1996a) Amino acid resolution of halothane binding sites in serum albumin. *J Biol Chem* **271**:15521–15526.

Eckenhoff RG (1996b) An inhalational anesthetic binding domain in the nicotinic acetylcholine receptor. *Proc Natl Acad Sci U S A* **93**:2807–2810.

Eckenhoff RG, and Johansson JS (1997) Molecular interactions between inhaled anesthetics and proteins. *Pharmacol Rev* **49**:343–368.

Eckenhoff RG, Knoll FJ, Greenblatt EP, and Dailey WP (2002) Halogenated diazirines as photolabel mimics of the inhaled haloalkane anesthetics. *J Med Chem* **45**:1879–1886.

Eckenhoff RG, Petersen CE, Ha CE, and Bhagavan NV (2000) Inhaled anesthetic binding sites in human serum albumin. *J Biol Chem* **275**:30439–30444.

Eckenhoff RG, Xi J, Shimaoka M, Bhattacharji A, Covarrubias M, and Dailey WP (2010) Azi-isoflurane, a photolabel analog of the commonly used inhaled general anesthetic isoflurane. *ACS Chem Neurosci* **1**:139–145.

el-Maghrabi EA, Eckenhoff RG, and Shuman H (1992) Saturable binding of halothane to rat brain synaptosomes. *Proc Natl Acad Sci U S A* **89**:4329–4332.

Emerson DJ, Liao Z, Eckenhoff RG, and Dmochowski IJ (2012) A novel fluorescent general anesthetic enables imaging of sites of action in vivo. *Anesthesiology* **116**:1363.

Emerson DJ, Weiser BP, Psonis J, Liao Z, Taratula O, Fiamengo A, Wang X, Sugasawa K, Smith AB 3rd, Eckenhoff RG, and Dmochowski IJ (2013) Direct modulation of microtubule stability contributes to anthracene general anesthesia. *J Am Chem Soc* **135**:5389–5398.

Eriksson M, Samuelsson H, Björklund S, Tortosa E, Avila J, Samuelsson E-B, Benedikz E, and Sundström E (2010) MAP1B binds to the NMDA receptor subunit NR3A and affects NR3A protein concentrations. *Neurosci Lett* **475**:33–37.

Finnin MS, Donigian JR, and Pavletich NP (2001) Structure of the histone deacetylase SIRT2. *Nat Struct Biol* **8**:621–625.

Fiske CH, and Subbarow Y (1925) The colorimetric determination of phosphorus. *J Biol Chem* **66**:375–400.

Flood P, Ramirez-Latorre J, and Role L (1997) Alpha 4 beta 2 neuronal nicotinic acetylcholine receptors in the central nervous system are inhibited by isoflurane and propofol, but alpha 7-type nicotinic acetylcholine receptors are unaffected. *Anesthesiology* **86**:859–865.

Folch J, Lees M, and Stanley GHS (1957) A simple method for the isolation and purification of total lipides from animal tissues. *J Biol Chem* **226**:497–509.

Foloppe N, and MacKerell, Jr. AD (2000) All-atom empirical force field for nucleic acids: I. Parameter optimization based on small molecule and condensed phase macromolecular target data. *J Comput Chem* **21**:86–104.

Franks NP (2008) General anaesthesia: from molecular targets to neuronal pathways of sleep and arousal. *Nat Rev Neurosci* **9**:370–386.

Garbelli R, Inverardi F, Medici V, Amadeo A, Verderio C, Matteoli M, and Frassoni C (2008) Heterogeneous expression of SNAP-25 in rat and human brain. *J Comp Neurol* **506**:373–386.

Gerachshenko T, Blackmer T, Yoon E-J, Bartleson C, Hamm HE, and Alford S (2005) Gβγ acts at the C terminus of SNAP-25 to mediate presynaptic inhibition. *Nat Neurosci* **8**:597–605.

Gerbig D, and Ley D (2013) Computational methods for contemporary carbene chemistry. *Wiley Interdiscip Rev Comput Mol Sci* **3**:242–272.

Gergalova G, Lykhmus O, Kalashnyk O, Koval L, Chernyshov V, Kryukova E, Tsetlin V, Komisarenko S, and Skok M (2012) Mitochondria express α7 nicotinic acetylcholine receptors to regulate Ca2+ accumulation and cytochrome c release: study on isolated mitochondria. *PloS ONE* **7**:e31361.

Gertz M, Fischer F, Nguyen GTT, Lakshminarasimhan M, Schutkowski M, Weyand M, and Steegborn C (2013) Ex-527 inhibits sirtuins by exploiting their unique NAD+-dependent deacetylation mechanism. *Proc Natl Acad Sci U S A* **110**:E2772–E2781.

Goujon M, McWilliam H, Li W, Valentin F, Squizzato S, Paern J, and Lopez R (2010) A new bioinformatics analysis tools framework at EMBL-EBI. *Nucleic Acids Res* **38**:W695–699.

Guex N, Peitsch MC, and Schwede T (2009) Automated comparative protein structure modeling with SWISS-MODEL and Swiss-PdbViewer: A historical perspective. *Electrophoresis* **30**:S162–S173.

Gurnev PA, Rostovtseva TK, and Bezrukov SM (2011) Tubulin-blocked state of VDAC studied by polymer and ATP partitioning. *FEBS Lett* **585**:2363–2366.

Hall MA, Xi J, Lor C, Dai S, Pearce R, Dailey WP, and Eckenhoff RG (2010) m-Azipropofol (AziPm) a photoactive analogue of the intravenous general anesthetic propofol. *J Med Chem* **53**:5667–5675.

Hameroff S, Nip A, Porter M, and Tuszynski J (2002) Conduction pathways in microtubules, biological quantum computation, and consciousness. *Biosystems* **64**:149–168.

Hameroff S, and Penrose R (1996) Orchestrated reduction of quantum coherence in brain microtubules: A model for consciousness. *Math Comput Simul* **40**:453–480.

Hamouda AK, Stewart DS, Husain SS, and Cohen JB (2011) Multiple transmembrane binding sites for p-trifluoromethyldiazirinyl-etomidate, a photoreactive Torpedo nicotinic acetylcholine receptor allosteric inhibitor. *J Biol Chem* **286**:20466–20477.

Hansen AH, Sørensen KT, Mathieu R, Serer A, Duelund L, Khandelia H, Hansen PL, and Simonsen AC (2013) Propofol modulates the lipid phase transition and localizes near the headgroup of membranes. *Chem Phys Lipids* **175-176**:84–91.

Harroun TA, Katsaras J, and Wassall SR (2006) Cholesterol hydroxyl group is found to reside in the center of a polyunsaturated lipid membrane. *Biochemistry* **45**:1227–1233.

Harroun TA, Katsaras J, and Wassall SR (2008) Cholesterol is found to reside in the center of a polyunsaturated lipid membrane. *Biochemistry* **47**:7090–7096.

Hellsten U, Harland RM, Gilchrist MJ, Hendrix D, Jurka J, Kapitonov V, Ovcharenko I, Putnam NH, Shu S, Taher L, Blitz IL, Blumberg B, Dichmann DS, Dubchak I, Amaya E, Detter JC, Fletcher R, Gerhard DS, Goodstein D, Graves T, Grigoriev IV, Grimwood J, Kawashima T, Lindquist E, Lucas SM, Mead PE, Mitros T, Ogino H, Ohta Y, Poliakov AV, Pollet N, Robert J, Salamov A, Sater AK, Schmutz J, Terry A, Vize PD, Warren WC, Wells D, Wills A, Wilson RK, Zimmerman LB, Zorn AM, Grainger R, Grammer T, Khokha MK, Richardson PM, and Rokhsar DS (2010) The genome of the Western clawed frog Xenopus tropicalis. *Science* **328**:633–636.

Herlitze S, Garcia DE, Mackie K, Hille B, Scheuer T, and Catterall WA (1996) Modulation of Ca2+ channels by G-protein beta gamma subunits. *Nature* **380**:258–262.

Herring BE, McMillan K, Pike CM, Marks J, Fox AP, and Xie Z (2011) Etomidate and propofol inhibit the neurotransmitter release machinery at different sites. *J Physiol* **589**:1103–1115.

Herring BE, Xie Z, Marks J, and Fox AP (2009) Isoflurane inhibits the neurotransmitter release machinery. *J Neurophysiol* **102**:1265–1273.

Hiller S, Abramson J, Mannella C, Wagner G, and Zeth K (2010) The 3D structures of VDAC represent a native conformation. *Trends Biochem Sci* **35**:514–521.

Hiller S, Garces RG, Malia TJ, Orekhov VY, Colombini M, and Wagner G (2008) Solution structure of the integral human membrane protein VDAC-1 in detergent micelles. *Science* **321**:1206–1210.

Hulce JJ, Cognetta AB, Niphakis MJ, Tully SE, and Cravatt BF (2013) Proteome-wide mapping of cholesterol-interacting proteins in mammalian cells. *Nat Methods* **10**:259–264.

Humphrey W, Dalke A, and Schulten K (1996) VMD: visual molecular dynamics. *J Mol Graph* **14**:33–38, 27–28.

Husain SS, Forman SA, Kloczewiak MA, Addona GH, Olsen RW, Pratt MB, Cohen JB, and Miller KW (1999) Synthesis and properties of 3-(2-hydroxyethyl)-3- *n* -pentyldiazirine, a photoactivable general anesthetic. *J Med Chem* **42**:3300–3307.

Husain SS, Nirthanan S, Ruesch D, Solt K, Cheng Q, Li G-D, Arevalo E, Olsen RW, Raines DE, Forman SA, Cohen JB, and Miller KW (2006) Synthesis of trifluoromethylaryl diazirine and benzophenone derivatives of etomidate that are potent general anesthetics and effective photolabels for probing sites on ligand-gated ion channels. *J Med Chem* **49**:4818–4825.

Husain SS, Stewart D, Desai R, Hamouda AK, Li SG-D, Kelly E, Dostalova Z, Zhou X, Cotten JF, Raines DE, Olsen RW, Cohen JB, Forman SA, and Miller KW (2010) p-Trifluoromethyldiazirinyl-etomidate: a potent photoreactive general anesthetic

derivative of etomidate that is selective for ligand-gated cationic ion channels. *J Med Chem* **53**:6432–6444.

Husain SS, Ziebell MR, Ruesch D, Hong F, Arevalo E, Kosterlitz JA, Olsen RW, Forman SA, Cohen JB, and Miller KW (2003) 2-(3-Methyl-3H-diaziren-3-yl)ethyl 1-(1-phenylethyl)-1H-imidazole-5-carboxylate: a derivative of the stereoselective general anesthetic etomidate for photolabeling ligand-gated ion channels. *J Med Chem* **46**:1257–1265.

Ikeda SR (1996) Voltage-dependent modulation of N-type calcium channels by G-protein beta gamma subunits. *Nature* **380**:255–258.

Ishizawa Y, Pidikiti R, Liebman PA, and Eckenhoff RG (2002) G protein-coupled receptors as direct targets of inhaled anesthetics. *Mol Pharmacol* **61**:945–952.

James R, and Glen JB (1980) Synthesis, biological evaluation, and preliminary structure-activity considerations of a series of alkylphenols as intravenous anesthetic agents. *J Med Chem* **23**:1350–1357.

Jayakar SS, Zhou X, Chiara DC, Dostalova Z, Savechenkov PY, Bruzik KS, Dailey WP, Miller KW, Eckenhoff RG, and Cohen JB (2014) Multiple propofol binding sites in a γ-aminobutyric acid type A receptor (GABAAR) identified using a photoreactive propofol analog. *J Biol Chem* **289**:27456-27468.

Jiang W, Wang S, Xiao M, Lin Y, Zhou L, Lei Q, Xiong Y, Guan K-L, and Zhao S (2011) Acetylation regulates gluconeogenesis by promoting PEPCK1 degradation via recruiting the UBR5 ubiquitin ligase. *Mol Cell* **43**:33–44.

Johansson JS, and Eckenhoff RG (1996) Minimum structural requirement for an inhalational anesthetic binding site on a protein target. *Biochim Biophys Acta* **1290**:63–68.

Jorgensen WL, Chandrasekhar J, Madura JD, Impey RW, and Klein ML (1983) Comparison of simple potential functions for simulating liquid water. *J Chem Phys* **79**:926–935.

Jo S, Kim T, and Im W (2007) Automated builder and database of protein/membrane complexes for molecular dynamics simulations. *PLoS ONE* **2**:e880.

Jo S, Lim JB, Klauda JB, and Im W (2009) CHARMM-GUI Membrane Builder for mixed bilayers and its application to yeast membranes. *Biophys J* **97**:50–58.

Jurd R, Arras M, Lambert S, Drexler B, Siegwart R, Crestani F, Zaugg M, Vogt KE, Ledermann B, Antkowiak B, and Rudolph U (2003) General anesthetic actions in vivo strongly attenuated by a point mutation in the GABA(A) receptor beta3 subunit. *FASEB J* **17**:250–252.

Kapitein LC, Yau KW, Gouveia SM, van der Zwan WA, Wulf PS, Keijzer N, Demmers J, Jaworski J, Akhmanova A, and Hoogenraad CC (2011) NMDA receptor activation suppresses microtubule growth and spine entry. *J Neurosci* **31**:8194–8209.

Katoh T, and Ikeda K (1987) The minimum alveolar concentration (MAC) of sevoflurane in humans. *Anesthesiology* **66**:301–303.

Kayser H, Kratzin HD, Thinnes FP, Götz H, Schmidt WE, Eckart K, and Hilschmann N (1989) Identification of human porins. II. Characterization and primary structure of a 31-lDa porin from human B lymphocytes (Porin 31HL). *Biol Chem Hoppe Seyler* **370**:1265–1278.

Kerner J, Lee K, Tandler B, and Hoppel CL (2012) VDAC proteomics: Post-translation modifications. *Biochim Biophys Acta* **1818**:1520–1525.

Kiefer F, Arnold K, Künzli M, Bordoli L, and Schwede T (2009) The SWISS-MODEL Repository and associated resources. *Nucleic Acids Res* **37**:D387–D392.

Klauda JB, Monje V, Kim T, and Im W (2012) Improving the CHARMM force field for polyunsaturated fatty acid chains. *J Phys Chem B* **116**:9424–9431.

Klauda JB, Venable RM, Freites JA, O'Connor JW, Tobias DJ, Mondragon-Ramirez C, Vorobyov I, MacKerell AD Jr, and Pastor RW (2010) Update of the CHARMM all-atom additive force field for lipids: validation on six lipid types. *J Phys Chem B* **114**:7830–7843.

Komarov AG, Deng D, Craigen WJ, and Colombini M (2005) New insights into the mechanism of permeation through large channels. *Biophys J* **89**:3950–3959.

Krammer E-M, Homblé F, and Prévost M (2011) Concentration dependent ion selectivity in VDAC: a molecular dynamics simulation study. *PloS ONE* **6**:e27994.

Krammer E-M, Homblé F, and Prévost M (2013) Molecular origin of VDAC selectivity towards inorganic ions: a combined molecular and Brownian dynamics study. *Biochim Biophys Acta* **1828**:1284–1292.

Krasowski MD, Jenkins A, Flood P, Kung AY, Hopfinger AJ, and Harrison NL (2001) General anesthetic potencies of a series of propofol analogs correlate with potency for potentiation of γ-aminobutyric acid (GABA) current at the GABAA receptor but not with lipid solubility. *J Pharmacol Exp Ther* **297**:338–351.

Kretschmannova K, Hines RM, Revilla-Sanchez R, Terunuma M, Tretter V, Jurd R, Kelz MB, Moss SJ, and Davies PA (2013) Enhanced tonic inhibition influences the hypnotic and amnestic actions of the intravenous anesthetics etomidate and propofol. *J Neurosci* **33**:7264–7273.

Kucerka N, Marquardt D, Harroun TA, Nieh M-P, Wassall SR, de Jong DH, Schäfer LV, Marrink SJ, and Katsaras J (2010) Cholesterol in bilayers with PUFA chains: doping with DMPC or POPC results in sterol reorientation and membrane-domain formation. *Biochemistry* **49**:7485–7493.

Kurkcuoglu Z, Bakan A, Kocaman D, Bahar I, and Doruker P (2012) Coupling between catalytic loop motions and enzyme global dynamics. *PLoS Comput Biol* **8**:e1002705.

Larkin MA, Blackshields G, Brown NP, Chenna R, McGettigan PA, McWilliam H, Valentin F, Wallace IM, Wilm A, Lopez R, Thompson JD, Gibson TJ, and Higgins DG (2007) Clustal W and Clustal X version 2.0. *Bioinforma Oxf Engl* **23**:2947–2948.

Lea WA, Xi J, Jadhav A, Lu L, Austin CP, Simeonov A, and Eckenhoff RG (2009) A high-throughput approach for identification of novel general anesthetics. *PloS ONE* **4**:e7150.

Lee KI, Rui H, Pastor RW, and Im W (2011) Brownian dynamics simulations of ion transport through the VDAC. *Biophys J* **100**:611–619.

Le Guilloux V, Schmidtke P, and Tuffery P (2009) Fpocket: an open source platform for ligand pocket detection. *BMC Bioinformatics* **10**:168.

Lehman P, and Berry R (1973) Flash photolytic decomposition of aryl azides. Measurement of an intramolecular closure rate. *J Am Chem Soc* **95**:8614–8620.

Lei P, Ayton S, Finkelstein DI, Spoerri L, Ciccotosto GD, Wright DK, Wong BXW, Adlard PA, Cherny RA, Lam LQ, Roberts BR, Volitakis I, Egan GF, McLean CA, Cappai R, Duce JA, and Bush AI (2012) Tau deficiency induces parkinsonism with dementia by impairing APP-mediated iron export. *Nat Med* **18**:291–295.

Lemasters JJ, and Holmuhamedov E (2006) Voltage-dependent anion channel (VDAC) as mitochondrial governator—Thinking outside the box. *Biochim Biophys Acta* **1762**:181–190.

Liang J, Edelsbrunner H, and Woodward C (1998) Anatomy of protein pockets and cavities: measurement of binding site geometry and implications for ligand design. *Protein Sci* **7**:1884–1897.

Liao M, Sonner JM, Husain SS, Miller KW, Jurd R, Rudolph U, and Eger EI (2005) R (+) etomidate and the photoactivable R (+) azietomidate have comparable anesthetic activity in wild-type mice and comparably decreased activity in mice with a N265M point mutation in the gamma-aminobutyric acid receptor β3 subunit. *Anesth Analg* **101**:131–135.

Lim JB, Rogaski B, and Klauda JB (2012) Update of the cholesterol force field parameters in CHARMM. *J Phys Chem B* **116**:203–210.

Liu L, Arun A, Ellis L, Peritore C, and Donmez G (2012) Sirtuin 2 (SIRT2) enhances 1-methyl-4-phenyl-1,2,3,6-tetrahydropyridine (MPTP)-induced nigrostriatal damage via deacetylating forkhead box O3a (Foxo3a) and activating Bim protein. *J Biol Chem* **287**:32307–32311.

Li W, Zhang B, Tang J, Cao Q, Wu Y, Wu C, Guo J, Ling E-A, and Liang F (2007) Sirtuin 2, a mammalian homolog of yeast silent information regulator-2 longevity regulator, is an oligodendroglial protein that decelerates cell differentiation through deacetylating alpha-tubulin. *J Neurosci* **27**:2606–2616.

Lomize MA, Pogozheva ID, Joo H, Mosberg HI, and Lomize AL (2012) OPM database and PPM web server: resources for positioning of proteins in membranes. *Nucleic Acids Res* **40**:D370–D376.

Lundbaek JA, and Andersen OS (1999) Spring constants for channel-induced lipid bilayer deformations. Estimates using gramicidin channels. *Biophys J* **76**:889–895.

MacKerell AD Jr, Feig M, and Brooks CL 3rd (2004) Improved treatment of the protein backbone in empirical force fields. *J Am Chem Soc* **126**:698–699.

MacKerell, AD, Bashford D, Bellott M, Dunbrack RL, Evanseck JD, Field MJ, Fischer S, Gao J, Guo H, Ha S, Joseph-McCarthy D, Kuchnir L, Kuczera K, Lau FTK, Mattos C, Michnick S, Ngo T, Nguyen DT, Prodhom B, Reiher WE, Roux B, Schlenkrich M, Smith JC, Stote R, Straub J, Watanabe M, Wiórkiewicz-Kuczera J, Yin D, and Karplus M (1998) All-Atom Empirical Potential for Molecular Modeling and Dynamics Studies of Proteins. *J Phys Chem B* **102**:3586–3616.

Magiera MM, and Janke C (2014) Post-translational modifications of tubulin. *Curr Biol* **24**:R351–354.

Maldonado EN, Sheldon KL, DeHart DN, Patnaik J, Manevich Y, Townsend DM, Bezrukov SM, Rostovtseva TK, and Lemasters JJ (2013) Voltage-dependent anion channels modulate mitochondrial metabolism in cancer cells: regulation by free tubulin and erastin. *J Biol Chem* **288**:11920–11929.

McWilliam H, Li W, Uludag M, Squizzato S, Park YM, Buso N, Cowley AP, and Lopez R (2013) Analysis tool web services from the EMBL-EBI. *Nucleic Acids Res* **41**:W597–600.

Meyer H (1901) Zur Theorie der Alkoholnarkose. *Arch Für Exp Pathol Pharmakol* **46**:338–346.

Mlayeh L, Chatkaew S, Léonetti M, and Homblé F (2010) Modulation of plant mitochondrial VDAC by phytosterols. *Biophys J* **99**:2097–2106.

Moniot S, Schutkowski M, and Steegborn C (2013) Crystal structure analysis of human Sirt2 and its ADP-ribose complex. *J Struct Biol* **182**:136–143.

Montero J, Morales A, Llacuna L, Lluis JM, Terrones O, Basañez G, Antonsson B, Prieto J, García-Ruiz C, Colell A, and Fernández-Checa JC (2008) Mitochondrial cholesterol contributes to chemotherapy resistance in hepatocellular carcinoma. *Cancer Res* **68**:5246–5256.

Morris GM, Huey R, Lindstrom W, Sanner MF, Belew RK, Goodsell DS, and Olson AJ (2009) AutoDock4 and AutoDockTools4: Automated docking with selective receptor flexibility. *J Comput Chem* **30**:2785–2791.

Murasaki O, Kaibara M, Nagase Y, Mitarai S, Doi Y, Sumikawa K, and Taniyama K (2003) Site of action of the general anesthetic propofol in muscarinic M1 receptor-mediated signal transduction. *J Pharmacol Exp Ther* **307**:995–1000.

Nagele P, Mendel JB, Placzek WJ, Scott BA, D'Avignon DA, and Crowder CM (2005) Volatile anesthetics bind rat synaptic snare proteins. *Anesthesiology* **103**:768–778.

Napper AD, Hixon J, McDonagh T, Keavey K, Pons J-F, Barker J, Yau WT, Amouzegh P, Flegg A, Hamelin E, Thomas RJ, Kates M, Jones S, Navia MA, Saunders JO, DiStefano PS, and Curtis R (2005) Discovery of indoles as potent and selective inhibitors of the deacetylase SIRT1. *J Med Chem* **48**:8045–8054.

Nettles JH, Li H, Cornett B, Krahn JM, Snyder JP, and Downing KH (2004) The binding mode of epothilone A on alpha,beta-tubulin by electron crystallography. *Science* **305**:866–869.

Nguyen HT, Li K, daGraca RL, Delphin E, Xiong M, and Ye JH (2009) Behavior and cellular evidence for propofol-induced hypnosis involving brain glycine receptors. *Anesthesiology* **110**:326–332.

North BJ, Marshall BL, Borra MT, Denu JM, and Verdin E (2003) The human Sir2 ortholog, SIRT2, is an NAD+-dependent tubulin deacetylase. *Mol Cell* **11**:437–444.

Overton CE (1901) Studien über die narkose zugleich ein beitrag zur allgemeinen pharmakologie. *Gustav Fischer, Jena, Switzerland*.

Palacios JM, Wamsley JK, and Kuhar MJ (1981) High affinity GABA receptors — autoradiographic localization. *Brain Res* **222**:285–307.

Palmieri F, and De Pinto V (1989) Purification and properties of the voltage-dependent anion channel of the outer mitochondrial membrane. *J Bioenerg Biomembr* **21**:417–425.

Pan JZ, Xi J, Tobias JW, Eckenhoff MF, and Eckenhoff RG (2007) Halothane binding proteome in human brain cortex. *J Proteome Res* **6**:582–592.

Paolini S, Scaloni A, Amoresano A, Marchese S, Napolitano E, and Pelosi P (1998) Amino acid sequence, post-translational modifications, binding and labelling of porcine odorant-binding protein. *Chem Senses* **23**:689–698.

Papon M-A, Whittington RA, El-Khoury NB, and Planel E (2011) Alzheimer's disease and anesthesia. *Front Neurodegener* **4**:272.

Passafaro M, and Sheng M (1999) Synaptogenesis: the MAP location of GABA receptors. *Curr Biol* **9**:R261–263.

Pastorino JG, and Hoek JB (2008) Regulation of hexokinase binding to VDAC. *J Bioenerg Biomembr* **40**:171–182.

Patel S, Wohlfeil ER, Rademacher DJ, Carrier EJ, Perry LJ, Kundu A, Falck JR, Nithipatikom K, Campbell WB, and Hillard CJ (2003) The general anesthetic propofol increases brain N‐arachidonylethanolamine (anandamide) content and inhibits fatty acid amide hydrolase. *Br J Pharmacol* **139**:1005–1013.

Pfaller R, Freitag H, Harmey MA, Benz R, and Neupert W (1985) A water-soluble form of porin from the mitochondrial outer membrane of Neurospora crassa. Properties and relationship to the biosynthetic precursor form. *J Biol Chem* **260**:8188–8193.

Phillips JC, Braun R, Wang W, Gumbart J, Tajkhorshid E, Villa E, Chipot C, Skeel RD, Kalé L, and Schulten K (2005) Scalable molecular dynamics with NAMD. *J Comput Chem* **26**:1781–1802.

Popp B, Schmid A, and Benz R (1995) Role of sterols in the functional reconstitution of water-soluble mitochondrial porins from different organisms. *Biochemistry* **34**:3352–3361.

Pratt MB, Husain SS, Miller KW, and Cohen JB (2000) Identification of sites of incorporation in the nicotinic acetylcholine receptor of a photoactivatible general anesthetic. *J Biol Chem* **275**:29441–29451.

Prinz H, Schmidt P, Böhm KJ, Baasner S, Müller K, Unger E, Gerlach M, and Günther EG (2009) 10-(2-oxo-2-phenylethylidene)-10H-anthracen-9-ones as highly active antimicrotubule agents: synthesis, antiproliferative activity, and inhibition of tubulin polymerization. *J Med Chem* **52**:1284–1294.

Ravelli RBG, Gigant B, Curmi PA, Jourdain I, Lachkar S, Sobel A, and Knossow M (2004) Insight into tubulin regulation from a complex with colchicine and a stathmin-like domain. *Nature* **428**:198–202.

Rehberg B, and Duch DS (1999) Suppression of central nervous system sodium channels by propofol. *Anesthesiology* **91**:512–520.

Rostovtseva TK, Antonsson B, Suzuki M, Youle RJ, Colombini M, and Bezrukov SM (2004) Bid, but not Bax, regulates VDAC channels. *J Biol Chem* **279**:13575–13583.

Rostovtseva TK, and Bezrukov SM (2008) VDAC regulation: role of cytosolic proteins and mitochondrial lipids. *J Bioenerg Biomembr* **40**:163–170.

Rostovtseva TK, Kazemi N, Weinrich M, and Bezrukov SM (2006) Voltage gating of VDAC is regulated by nonlamellar lipids of mitochondrial membranes. *J Biol Chem* **281**:37496–37506.

Rostovtseva TK, Sheldon KL, Hassanzadeh E, Monge C, Saks V, Bezrukov SM, and Sackett DL (2008) Tubulin binding blocks mitochondrial voltage-dependent anion channel and regulates respiration. *Proc Natl Acad Sci U S A* **105**:18746–18751.

Rostovtseva TK, Tan W, and Colombini M (2005) On the role of VDAC in apoptosis: fact and fiction. *J Bioenerg Biomembr* **37**:129–142.

Rouslin W, MacGee J, Gupte S, Wesselman A, and Epps DE (1982) Mitochondrial cholesterol content and membrane properties in porcine myocardial ischemia. *Am J Physiol* **242**:H254–259.

Rui H, Lee KI, Pastor RW, and Im W (2011) Molecular dynamics studies of ion permeation in VDAC. *Biophys J* **100**:602–610.

Sanner MF (1999) Python: a programming language for software integration and development. *J Mol Graph Model* **17**:57–61.

Savechenkov PY, Zhang X, Chiara DC, Stewart DS, Ge R, Zhou X, Raines DE, Cohen JB, Forman SA, Miller KW, and Bruzik KS (2012) Allyl m-trifluoromethyldiazirine mephobarbital: an unusually potent enantioselective and photoreactive barbiturate general anesthetic. *J Med Chem* **55**:6554–6565.

Schneider R, Etzkorn M, Giller K, Daebel V, Eisfeld J, Zweckstetter M, Griesinger C, Becker S, and Lange A (2010) The native conformation of the human VDAC1 N terminus. *Angew Chem Int Ed* **49**:1882–1885.

Schredelseker J, Paz A, López CJ, Altenbach C, Leung CS, Drexler MK, Chen J-N, Hubbell WL, and Abramson J (2014) High resolution structure and double electron-electron resonance of the zebrafish voltage-dependent anion channel 2 reveal an oligomeric population. *J Biol Chem* **289**:12566–12577.

Sims NR, and Anderson MF (2008) Isolation of mitochondria from rat brain using Percoll density gradient centrifugation. *Nat Protoc* **3**:1228–1239.

Smart OS, Goodfellow JM, and Wallace BA (1993) The pore dimensions of gramicidin A. *Biophys J* **65**:2455–2460.

Smith C, McEwan AI, Jhaveri R, Wilkinson M, Goodman D, Smith LR, Canada AT, and Glass PS (1994) The interaction of fentanyl on the Cp50 of propofol for loss of consciousness and skin incision. *Anesthesiology* **81**:820–828.

Song J, Midson C, Blachly-Dyson E, Forte M, and Colombini M (1998) The topology of VDAC as probed by biotin modification. *J Biol Chem* **273**:24406–24413.

Southwood CM, Peppi M, Dryden S, Tainsky MA, and Gow A (2007) Microtubule deacetylases, SirT2 and HDAC6, in the nervous system. *Neurochem Res* **32**:187–195.

Stewart DS, Savechenkov PY, Dostalova Z, Chiara DC, Ge R, Raines DE, Cohen JB, Forman SA, Bruzik KS, and Miller KW (2011) p-(4-Azipentyl)propofol: a potent photoreactive general anesthetic derivative of propofol. *J Med Chem* **54**:8124–8135.

Suchyna TM, Tape SE, Koeppe RE, Andersen OS, Sachs F, and Gottlieb PA (2004) Bilayer-dependent inhibition of mechanosensitive channels by neuroactive peptide enantiomers. *Nature* **430**:235–240.

Tang P, Eckenhoff RG, and Xu Y (2000) General anesthetic binding to gramicidin A: the structural requirements. *Biophys J* **78**:1804–1809.

Teijido O, Rappaport SM, Chamberlin A, Noskov SY, Aguilella VM, Rostovtseva TK, and Bezrukov SM (2014) Acidification affects voltage-dependent anion channel functioning asymmetrically: role of salt bridges. *J Biol Chem* **289**:23670-23682.

Thomas L, Blachly-Dyson E, Colombini M, and Forte M (1993) Mapping of residues forming the voltage sensor of the voltage-dependent anion-selective channel. *Proc Natl Acad Sci U S A* **90**:5446–5449.

Tomasello MF, Guarino F, Reina S, Messina A, and De Pinto V (2013) The voltage-dependent anion selective channel 1 (VDAC1) topography in the mitochondrial outer membrane as detected in intact cell. *PloS ONE* **8**:e81522.

Trott O, and Olson AJ (2010) AutoDock Vina: improving the speed and accuracy of docking with a new scoring function, efficient optimization, and multithreading. *J Comput Chem* **31**:455–461.

Tsuchiya H (2001) Structure-specific membrane-fluidizing effect of propofol. *Clin Exp Pharmacol Physiol* **28**:292–299.

Ujwal R, Cascio D, Colletier J-P, Faham S, Zhang J, Toro L, Ping P, and Abramson J (2008) The crystal structure of mouse VDAC1 at 2.3 A resolution reveals mechanistic insights into metabolite gating. *Proc Natl Acad Sci U S A* **105**:17742–17747.

Vander Heiden MG, Chandel NS, Li XX, Schumacker PT, Colombini M, and Thompson CB (2000) Outer mitochondrial membrane permeability can regulate coupled respiration and cell survival. *Proc Natl Acad Sci U S A* **97**:4666–4671.

Vander Heiden MG, Li XX, Gottleib E, Hill RB, Thompson CB, and Colombini M (2001) Bcl-xL promotes the open configuration of the voltage-dependent anion channel and metabolite passage through the outer mitochondrial membrane. *J Biol Chem* **276**:19414–19419.

Van Swinderen B, Saifee O, Shebester L, Roberson R, Nonet ML, and Crowder CM (1999) A neomorphic syntaxin mutation blocks volatile-anesthetic action in Caenorhabditis elegans. *Proc Natl Acad Sci U S A* **96**:2479–2484.

Vaquero A, Scher MB, Lee DH, Sutton A, Cheng H-L, Alt FW, Serrano L, Sternglanz R, and Reinberg D (2006) SirT2 is a histone deacetylase with preference for histone H4 Lys 16 during mitosis. *Genes Dev* **20**:1256–1261.

Vaquero A, Sternglanz R, and Reinberg D (2007) NAD+-dependent deacetylation of H4 lysine 16 by class III HDACs. *Oncogene* **26**:5505–5520.

Vedula LS, Brannigan G, Economou NJ, Xi J, Hall MA, Liu R, Rossi MJ, Dailey WP, Grasty KC, Klein ML, Eckenhoff RG, and Loll PJ (2009) A unitary anesthetic binding site at high resolution. *J Biol Chem* **284**:24176–24184.

Vempati RK, Jayani RS, Notani D, Sengupta A, Galande S, and Haldar D (2010) p300-mediated acetylation of histone H3 lysine 56 functions in DNA damage response in mammals. *J Biol Chem* **285**:28553–28564.

Verderio C, Pozzi D, Pravettoni E, Inverardi F, Schenk U, Coco S, Proux-Gillardeaux V, Galli T, Rossetto O, Frassoni C, and Matteoli M (2004) SNAP-25 modulation of calcium dynamics underlies differences in GABAergic and glutamatergic responsiveness to depolarization. *Neuron* **41**:599–610.

Villinger S, Briones R, Giller K, Zachariae U, Lange A, Groot BL de, Griesinger C, Becker S, and Zweckstetter M (2010) Functional dynamics in the voltage-dependent anion channel. *Proc Natl Acad Sci U S A* **107**:22546–22551.

Violet JM, Downie DL, Nakisa RC, Lieb WR, and Franks NP (1997) Differential sensitivities of mammalian neuronal and muscle nicotinic acetylcholine receptors to general anesthetics. *Anesthesiology* **86**:866–874.

Wang H, and Olsen RW (2000) Binding of the GABA(A) receptor-associated protein (GABARAP) to microtubules and microfilaments suggests involvement of the cytoskeleton in GABARAPGABA(A) receptor interaction. *J Neurochem* **75**:644–655.

Weinrich M, Rostovtseva TK, and Bezrukov SM (2009) Lipid-dependent effects of halothane on gramicidin channel kinetics: a new role for lipid packing stress. *Biochemistry* **48**:5501–5503.

Weiser TG, Regenbogen SE, Thompson KD, Haynes AB, Lipsitz SR, Berry WR, and Gawande AA (2008) An estimation of the global volume of surgery: a modelling strategy based on available data. *The Lancet* **372**:139–144.

Werner HB, Kuhlmann K, Shen S, Uecker M, Schardt A, Dimova K, Orfaniotou F, Dhaunchak A, Brinkmann BG, Möbius W, Guarente L, Casaccia-Bonnefil P, Jahn O, and Nave K-A (2007) Proteolipid protein is required for transport of sirtuin 2 into CNS myelin. *J Neurosci* **27**:7717–7730.

Whittington RA, Virág L, Marcouiller F, Papon M-A, El Khoury NB, Julien C, Morin F, Emala CW, and Planel E (2011) Propofol directly increases tau phosphorylation. *PloS ONE* **6**:e16648.

Wickley PJ, Yuge R, Martin BA, Meyer JS, and Damron DS (2009) Propofol activates and allosterically modulates recombinant protein kinase Cε. *Anesthesiology* **111**:36–43.

Wiser O, Trus M, Hernández A, Renström E, Barg S, Rorsman P, and Atlas D (1999) The voltage sensitive Lc-type Ca2+ channel is functionally coupled to the exocytotic machinery. *Proc Natl Acad Sci U S A* **96**:248–253.

Wood NT, Fadda E, Davis R, Grant OC, Martin JC, Woods RJ, and Travers SA (2013) The influence of N-linked glycans on the molecular dynamics of the HIV-1 gp120 V3 loop. *PLoS ONE* **8**:e80301.

Woolf TB, and Roux B (1996) Structure, energetics, and dynamics of lipid–protein interactions: A molecular dynamics study of the gramicidin A channel in a DMPC bilayer. *Proteins Struct Funct Bioinforma* **24**:92–114.

Xi J, Liu R, Asbury GR, Eckenhoff MF, and Eckenhoff RG (2004) Inhalational anesthetic-binding proteins in rat neuronal membranes. *J Biol Chem* **279**:19628–19633.

Xi J, Liu R, Rossi MJ, Yang J, Loll PJ, Dailey WP, and Eckenhoff RG (2006) Photoactive analogues of the haloether anesthetics provide high-resolution features from low-affinity interactions. *ACS Chem Biol* **1**:377–384.

Yagoda N, von Rechenberg M, Zaganjor E, Bauer AJ, Yang WS, Fridman DJ, Wolpaw AJ, Smukste I, Peltier JM, Boniface JJ, Smith R, Lessnick SL, Sahasrabudhe S, and Stockwell BR (2007) RAS-RAF-MEK-dependent oxidative cell death involving voltage-dependent anion channels. *Nature* **447**:864–868.

Yip GMS, Chen Z-W, Edge CJ, Smith EH, Dickinson R, Hohenester E, Townsend RR, Fuchs K, Sieghart W, Evers AS, and Franks NP (2013) A propofol binding site on mammalian GABAA receptors identified by photolabeling. *Nat Chem Biol* **9**:715–720.

Zachariae U, Schneider R, Briones R, Gattin Z, Demers J-P, Giller K, Maier E, Zweckstetter M, Griesinger C, Becker S, Benz R, de Groot BL, and Lange A (2012) β-barrel mobility underlies closure of the voltage-dependent anion channel. *Structure 1993* **20**:1540–1549.

Zhang X, Liu Y, Feng C, Yang S, Wang Y, Wu A, and Yue Y (2009) Proteomic profiling of the insoluble fractions in the rat hippocampus post-propofol anesthesia. *Neurosci Lett* **465**:165–170.

Zhong H, Rüsch D, and Forman SA (2008) Photo-activated azi-etomidate, a general anesthetic photolabel, irreversibly enhances gating and desensitization of γ-aminobutyric acid type A receptors. *Anesthesiology* **108**:103–112.

Ziebell MR, Nirthanan S, Husain SS, Miller KW, and Cohen JB (2004) Identification of binding sites in the nicotinic acetylcholine receptor for [3H]azietomidate, a photoactivatable general anesthetic. *J Biol Chem* **279**:17640–17649.

Zimmermann MT, and Jernigan RL (2012) Protein loop dynamics are complex and depend on the motions of the whole protein. *Entropy* **14**:687–700.

Zuse A, Schmidt P, Baasner S, Böhm KJ, Müller K, Gerlach M, Günther EG, Unger E, and Prinz H (2007) Sulfonate derivatives of naphtho[2,3-b]thiophen-4(9H)-one and 9(10H)-anthracenone as highly active antimicrotubule agents. Synthesis, antiproliferative activity, and inhibition of tubulin polymerization. *J Med Chem* **50**:6059–6066.